universität wien

DISSERTATION

Titel der Dissertation

Experimental study of nucleation in different vapors and its temperature dependence and the effect of particle properties on the response of condensation particle counters

Verfasserin

DI Agnieszka Kupc BSc

angestrebter akademischer Grad

Doktorin der Naturwissenschaften (Dr. rer. nat.)

Wien, 2013

Studienkennzahl lt. Studienblatt:	A 091 411
Dissertationsgebiet lt. Studienblatt:	A 091 411 Physik
Betreuer:	Ao. Univ.-Prof. Dr. Dr. h.c Paul E. Wagner

This PhD thesis is a cumulative work consisting of seven chapters.
Chapter 1 – Introduction – provides the problem statement, state of the art and motivation for the performed research. As a background for this thesis some theoretical aspects of nucleation are described in Chapter 2.
The main content of the PhD research is provided in four publications (Chapters 3, 4, 5 and 6) including one coauthorship paper. The achieved results are outlined and discussed in Chapter 7 – Conclusions. Finally an outlook is provided at the end of Chapter 7 - Implications and Future work. References are listed in Bibliography section located at the end of this PhD thesis.

ABSTRACT

Despite ongoing efforts radiative forcing of aerosols and clouds still represents the highest uncertainty in our current understanding of climate change [54]. Its quantification is extremely difficult since properties of aerosols such as composition, concentration, size, lifetime, or spatial and temporal distribution vary greatly. To better understand the influence of aerosols on the climate it is necessary to clarify the mechanisms of aerosol formation defining the before-mentioned properties.
Those mechanisms are referred to as homogeneous or heterogeneous nucleation processes depending on whether they are initiated from vapors or on pre-existing seed particles. The composition of participating vapors, the kinetics of cluster growth and evaporation, the influence of temperature and ionizing radiation as well as the nature and charge of involved particles are currently under investigation and are generally considered to be critical to the understanding of the climate.

In this PhD research the effect of (1) ions, temperature and various vapors on homogeneous nucleation, (2) temperature and seed properties on heterogeneous nucleation, as well as (3) particle composition on the response of condensation particle counters (CPC) were investigated. This was achieved using state-of-the-art aerosol- and gas-phase instruments at the CLOUD chamber for (1), and expansion type CPC (SANC) for (2), as well as commercially available laminar-flow water- and n-butanol-based particle counters in the laboratory for (3).

ad(1): ***The effect of ions, temperature and various vapors on homogeneous nucleation***
To perform homogeneous nucleation experiments a clean and thermally stable environment such as at the CLOUD chamber is needed. At this unique electropolished stainless steel cylinder (26.1 m^3) the effect of ionizing radiation on binary

and ternary nucleation can be studied. To investigate those processes a stable concentration of sulfuric acid is required as it is one of the key components taking part in atmospheric nucleation. Therefore an innovative fibre-optic UV system was installed at CLOUD in order to trigger photochemical reactions by the same mechanisms as they exist in the atmosphere. Concentrations of sulfuric acid produced in the CLOUD chamber through ozone photolysis have proven to be stable and reproducible [80] (**Chapter III/Paper I**). The fibre-optic UV system characterized in this work has shown only negligible thermal effect, which is of crucial importance in nucleation studies. So far such high thermal stability has not been achieved in another comparable experimental set-up.
In-situ production of sulfuric acid at the CLOUD chamber allowed for the investigation of homogeneous binary (H_2SO_4-H_2O) and ternary (H_2SO_4-H_2O-NH_3) nucleation at three different temperatures (248, 278, 292 K). Results have shown that both mechanisms cannot account for atmospheric boundary layer nucleation, and that another component e.g. an organic compound is missing. As the role of organics in nucleation processes is not yet resolved, the assessment of the influence of ionizing radiation in the atmospheric nucleation requires further research. For the processes investigated here an ion enhancement has been observed for all considered temperatures. Through this CLOUD study a significant progress has been made on the direct measurement of the composition from homogeneously nucleated molecular cluster up to the aerosol particles [69] (**Chapter IV/Paper II**).

ad(2): ***The effect of temperature and seed properties on heterogeneous nucleation***

Also in heterogeneous nucleation processes temperature is a critical factor. The temperature dependence has recently gained some attention especially as unusual temperature trends of heterogeneous nucleation of n-propanol vapour on sodium chloride particles were reported [121]. According to McGraw et al. [91] the unusual behavior may be related to strong seed surface effects. Investigation of heterogeneous nucleation is equally important as homogeneous processes since aerosol particles in the atmosphere may also form on pre-existing seeds (such as stable homogeneously formed clusters or particles emitted to the atmosphere such as sea-salt). In the framework of this PhD the effect of particle properties and temperature (263-288 K) on heterogeneous nucleation of water vapour using expansion type CPC (SANC) was studied. Results described in this work have revealed an unexpected

temperature trend for silver seeds where the onset saturation ratio exhibits a pronounced maximum at about 278 K (**Chapter V/Paper III**). The effect for sodium chloride particles however, was found to be in qualitative agreement with theory. Those findings are highly relevant for both fundamental and instruments aspects.

ad(3): ***The effect of particle composition on the response of condensation particle counters (CPC)***
Since the nature of the particle may affect its activation and growth the effect of seed properties on the response of commercially available condensation particle counters was studied using water and n-butanol liquid. CPCs are the most common instruments used in nucleation studies and their performance may be critically influenced by specific properties of both particle and working liquid. The results of the present study provide an insight on how the variability and complexity of particles (such as composition, solubility, wettability, shape or size) may influence the activation and counting efficiency of a CPC-type instrument and impact its lowest cut-off size (**Chapter VI/Paper IV**).

One of the main obstacles to furthering our understanding of nucleation is our inability to identify critical processes (such as formation of a new phase - cluster) due to instrument detection thresholds. Findings reported in this PhD thesis may lead to significant improvement of the basic knowledge of nucleation mechanisms. Further they allow more precisely incorporate particle formation in climate models resulting in more accurate predictions. In addition, this work may contribute to optimize condensation particle counters and induce further improvements of these instruments.

KURZFASSUNG

Im Fokus der vorliegenden Dissertation stehen die verschiedenen Nukleationsprozesse (homogene und heterogene) und deren relevante Einflussgrößen.
Prozesse der homogenen Nukleation wurden mit Hilfe unterschiedlicher Aerosol- und Gasphasenmessgeräte in der CLOUD Versuchskammer untersucht. Um hinreichend stabile Schwefelsäure - Konzentrationen im Inneren der Kammer zu erreichen, wurde ein neuartiges UV-Bestrahlung-System entwickelt welches sich durch vernachlässigbare thermische Effekte auszeichnet (**Chapter III/Paper I**). Im Rahmen der durchgeführten Experimente wurde versucht der Einfluss (1) des Vorhandenseins von Ionen, (2) der Temperatur sowie (3) der Zusammensetzung der betrachteten Dämpfe auf die homogene Nukleation aufzuklären. Die experimentellen Nukleationsraten in binären Wasser-Schwefelsäure und ternären Wasser-Schwefelsäure-Ammoniak-Systemen die dabei beobachtet wurden, können atmosphärische Nukleationsraten an der Erdoberfläche nicht allerdings erklären (**Chapter IV/Paper II**).

Ergänzend dazu wurden in einem Expansionskammer-Messsystem, dem sogenannten Size Analyzing Nuclei Counter (SANC), Versuche zur heterogenen Nukleation durchgeführt. Insbesondere sollten die Temperaturabhängigkeit sowie der potentielle Einfluss der Eigenschaften der Nukleationskerne auf heterogene Nukleationsprozesse untersucht werden. Die Ergebnisse zeigen einen unerwarteten Temperaturtrend bei der heterogenen Nukleation von Wasserdampf an Silber-Partikeln mit einem ausgeprägten Maximum des Sättigungsverhältnises bei 278 K (**Chapter V/Paper III**). Abweichungen von den theoretisch zu erwartenden Temperaturabhängigkeiten wurden bereits von Schobersberger et al. [121] für NaCl Partikel in n-Propanol-Dämpf beaobachtet. Laut McGraw et al. [91] könnten diese Ergebnisse möglicherweise durch starke Oberflächeneffekte erklärt werden.

Des Weiteren wurden verschiedene Partikelarten mit kommerziellen Kondensa-

tionkernzählern ('condensation particle counter', CPC) untersucht, um festzustellen wie sich physikalisch-chemische Eigenschaften auf die Zählergebisse dieser Geräte auswirken. Es konnte gezeigt werden, dass die Zähleffizienz von kommerziellen CPCs insbesondere von Faktoren wie Größe, Zusammensetzung, Benetzbarkeit und Löslichkeit von Kondensationskernen abhängt (**Chapter VI**/**Paper IV**).

Die Ergebnisse der vorliegenden Arbeit weisen auf ein unerwartetes Temperaturvehalten bei heterogener Nukleation hin. Die quantitativen Messungen von Partikelkernbildungsraten unter präzise kontrollierten Bedingungen können zu einer Verbesserung bestehender Klimamodelle beitragen. Die durchgefürten Nukleationsexperimente sind auch für die Weiterentwicklung von CPCs von Bedeutung.

Erkenntnisse der hier durchgeführten Arbeiten, können einen signifikanten Beitrag zu einem besseren Grundverständnis von Nukleationsvorgängen leisten. Insbesondere wird es möglich sein, durch eine adäquate Berücksichtigung von Partikelbildung und verwandten Prozessen, bessere Klimamodelle und Vorhersagen zu generieren. Zuletzt können die hier gelieferten Ergebnisse auch dazu verwendet werden die Entwicklung verbesserter CPC-Geräte zu unterstützen.

LIST OF PUBLICATIONS AND AUTHOR CONTRIBUTION

PAPER I (PUBLISHED)

A fibre-optic UV system for H_2SO_4 production in aerosol chambers causing minimal thermal effects

Kupc, A., Amorim, A., Curtius, J., Danielczok, A., Duplissy, J., Ehrhart, S., Walther, H., Ickes, L., Kirkby, J., Kuerten, A., Lima, J.M., Mathot, S., Minginette, P., Onnela, A., Rondo, L., Wagner, P.E.

(2011), *Journal of Aerosol Science*, 42, 8, 532-543

DOI:10.1016/j.jaerosci.2011.05.001

Author Contribution:

The author took a leading role during the characterization of the UV fibre-optic system used at the CLOUD chamber at CERN. Required measurements as described in this publication were performed by the author together with some of the co-authors. Further, contributions include part of the design, installation of the UV fibre-optic system, data collection and evaluation as well as writing most of the manuscript underlying the final paper.

PAPER II (PUBLISHED)

Role of sulphuric acid, ammonia and galactic cosmic rays in atmospheric aerosol nucleation

Kirkby, J., Curtius, J., Almeida, J., Dunne, E., Duplissy, J., Ehrhart, S., Franchin, A., Gagne, S., Ickes, L., Kurten, A., **Kupc, A.**, Metzger, A., Riccobono, F., Rondo, L., Schobesberger, S., Tsagkogeorgas, G.,Wimmer, D., Amorim, A., Bianchi, F.,

Breitenlechner, M., David, A., Dommen, J., Downard, A., Ehn, M., Flagan, R. C., Haider, S., Hansel, A., Hauser, D., Jud, W., Junninen, H., Kreissl, F., Kvashin, A., Laaksonen, A., Lehtipalo, K., Lima, J., Lovejoy, E. R., Makhmutov, V., Mathot, S., Mikkila, J., Minginette, P., Mogo, S., Nieminen, T., Onnela, A., Pereira, P., Petaja, T., Schnitzhofer, R., Seinfeld, J. H., Sipila, M., Stozhkov, Y., Stratmann, F., Tome, A., Vanhanen, J., Viisanen, Y., Vrtala, A., Wagner, P. E., Walther, H., Weingartner, E., Wex, H., Winkler, P. M., Carslaw, K. S., Worsnop, D. R., Baltensperger, U., and Kulmala, M.
(2011), *Nature*, 476, 429-433, DOI: 10.1038/nature10343

Author Contribution:
The main tasks performed by Agnieszka Kupc on the investigation of binary and ternary nucleation and the effect of ions and temperature at CLOUD experiment were mostly related to data collection and analysis as well as experiment supervision. In addition the Agnieszka Kupc contributed to the development of the CLOUD facility through characterization of the UV fibre-optic system and several analysis instruments. As one of the co-authors, Agnieszka Kupc also commented on the manuscript.

PAPER III (SUBMITTED)

The unusual temperature dependence of heterogeneous nucleation of water vapor on Ag particles
Kupc A., Winkler, P.M., Vrtala, M. and Wagner P.E.
(Manuscript submitted as an Aerosol Research Letter to *Aerosol Science and Technology*: 20^{th} February 2013)

Author Contribution:
The goal of this study was to investigate the effect of temperature of heterogeneous nucleation of water vapor on particles with various physico-chemical properties. The research for this publication was undertaken at University of Vienna where the experimental work and the evaluation of the data have been carried out entirely by the author. Agnieszka Kupc also wrote the manuscript.

PAPER IV (PUBLISHED)

Laboratory Characterization of a New Nano-Water-Based CPC 3788 and Performance Comparison to an Ultrafine Butanol-Based CPC 3776
Kupc, A., Bischof, O., Tritscher, T., Beeston, M., Krinke, T. and Wagner, P.E. **(2013)**, *Aerosol Science and Technology*, 47:2, 183-191
DOI:10.1080/02786826.2012.738317

Author Contribution:
The experimental work has been performed during a CLOUD-ITN secondment at TSI, Aachen in January 2012. The goal of this study was to evaluate the effect of particles with various properties on the response of different condensation particle counters. Agnieszka Kupc was involved in organizing the measurements and together with co-authors she set up the experimental system. Agnieszka did the majority of measurements for evaluation of counting efficiencies for both particle counters and performed data analysis. Further, Agnieszka wrote the manuscript.

ACKNOWLEDGEMENTS

I am grateful to many people who contributed to the great experience that was my PhD research.
First of all I would like to thank my advisor, Prof. Paul E. Wagner, for giving me meaningful support and guidance along the way. Thank you Paul, it has been a wonderful learning experience!
Furthermore, I am grateful to Dr. Paul M. Winkler for his patience and constructive suggestions. I benefited greatly from his experience and support.
Additionally I would like to express my gratitude to the CLOUD community. It has been a privilege working with you. I have greatly enjoyed this opportunity of collaborating with many great scientists. In particular I would like to thank Dr. Jasper Kirkby from CERN, Prof. Joachim Curtius from Goethe-Universität Frankfurt am Main and Dr. Jonathan Duplissy from CERN for your contagious enthusiasm for aerosol research. Big thanks to my colleagues and friends from CLOUD-ITN project. You are too many to name. It would not be the same without you guys!
I would also like to thank the two reviewers for grading this thesis. Thank you for your time and interest in my work.
In addition, I would like to thank the co-authors for their cooperation and contributions. Many of the results would not have been possible without your valuable input.

Further, big thanks to my colleagues at the Aerosol and Environmental Physics Group at University of Vienna for a pleasant and inspiring working environment - in particular Tamara Pinterich, Dr. Aron Vrtala and Peter Kallinger for the fruitful discussions.
Furthermore, thank you to the colleagues at TSI in Aachen, Germany: Oliver Bischof, Torsten Tritscher, Michael Beeston, and Thomas Krinke for hosting my CLOUD-ITN Secondment in January 2012. It has been a great learning experience working with you. Thank you! I would also like to thank all other friends that put

up with me in the last four years - in particular Martina Kasper. Thank you Alain Straus for your patience, understanding and support during all those times I had to go off alone to write. You never let me forget that life is not only about work.
Finally, I would like to thank my family: Malgorzata, Alicja and Ryszard for their infinite support! Dziekuje za wszystko!

This research was supported by the EC's Seventh Framework Programme under the grant agreement no. 215072 (Marie Curie Initial Training Network CLOUD-ITN), and by the Austrian Science Fund (project no. P 19546, L593). This work was performed at a) Aerosol and Environmental Physics Group, Faculty of Physics, Vienna, Austria; b) CERN, Geneva, Switzerland and c) TSI Research and Analytics, Aachen, Germany.

TABLE OF CONTENTS

CHAPTER 1

INTRODUCTION

1.1 Motivation

As highlighted in the 2007 report of the Intergovernmental Panel on Climate Change [54] climate change is driven by altering the Earth's energy balance. Increasing concentrations of greenhouse gases (such as carbon dioxide and methane) and aerosols, as well as changes in land cover and solar radiation lead to different radiation patterns (absorption, scattering, emission) throughout the atmosphere and at the surface of the Earth. Depending on the nature of the energy balance shift, either warming or cooling effects are anticipated [122]. So far results on temperature measurements of the atmosphere and the upper part of the ocean indicated warming of the climate [54].

The sources and the warming effect of greenhouse gases are well understood. However, the key uncertainties remain in the field associated with net cooling effect aerosols and clouds. To evaluate their influence on climate, knowledge on the mechanisms by which aerosols and further clouds are forming is crucial. The first steps of aerosol formation are referred to as nucleation mechanisms. Nucleation describes formation of solid or liquid particles that either form from vapor molecules itself, on a pre-existing seed particle or upon an ion or ion cluster. Those may further grow to droplets big enough to become seeds for clouds.

As indicated by Pierce [111], every cloud droplet in the atmosphere is formed on an aerosol particle. Thus any changes in aerosol concentration or composition may

change cloud properties by impacting on the number of activated droplets, their lifetime, reflectivity, precipitation and/or size distribution [122]. The impact of new particle formation on particle concentrations is significant however has not yet been quantified [65, 129, 151]. The same concerns the influence of aerosols on changes in temperature, clouds albedo or precipitation. As indicated by Merikanto et al. [94] and Kirkby et al. [69] nearly 50 % of global cloud condensation nuclei in the atmospheric boundary layer may be formed through new particle formation.

Understanding atmospheric nucleation mechanisms requires knowledge on the participating vapors, the kinetics of cluster growth and evaporation, charging or the influence of seed particle properties. Low level of scientific knowledge in aerosol research is mainly due to the variability of the aerosols in time and space. In addition, new advances in this field are restricted by the detection thresholds of the available instrumentation used in nucleation studies.

To establish the influence of aerosols and clouds on climate, the knowledge of the mechanisms of particle formation in the atmosphere - as a base to quantify the climate-relevant impacts of aerosols and further improve climate model predictions - is indispensable.

In the framework of the present thesis the focus is given to the issues that currently limit our understanding of atmospheric particle formation - nucleation processes.

1.2 Particle formation in the atmosphere

Particles in the atmosphere known as aerosols are solids or liquids suspended in a gas. When the aerosol is emitted directly to the atmosphere (e.g. by combustion, plants or sea-spray) it is called primary aerosol. In case it is formed in the atmosphere through chemical processes from precursor vapors it is referred as a secondary aerosol [122, 172].

The mechanism by which new particles are formed is known as nucleation, in other words formation of a new phase. Nucleation produces a large fraction of aerosols present in the atmosphere and has been observed in marine, urban or forested environments [172].

When gaseous molecules bond a new particle is formed. This process is called homogeneous nucleation. In case a pre-existing seed particle is present a heterogeneous nucleation and condensation on the aerosol particle takes place. In general it is more energetically favorable for vapor or mixtures of vapors to condense on the smallest seed particle than to form a new one from vapors [161]. Finally, ion-induced nucleation is based on the formation of stable nuclei of the condensed phase on ions or ion clusters in the atmosphere [24, 47, 157].

The first step of new particle formation involves formation of a critical nucleus [75]. When the critical nucleus forms, the free energy of the nucleating system reaches a maximum the so called nucleation barrier beyond which the growth of the particle becomes spontaneous. Atmospheric aerosol formation is usually defined by formation and growth rates [75]. The former is the rate at which particles are being produced (particles $cm^{-3}s^{-1}$), while the latter describes how rapidly particles grow to larger sizes (nm h^{-1}). The rate at which nucleation occurs is related to the chemical composition of the critical nucleus and the concentrations of gaseous species [172]. It is a crucial variable in simulations of aerosol formation in climate models.

Nucleation occurs in bursts and is limited by the production rate of precursor gases [47]. The subsequent particle growth is possible due to vapor-particle reactions or condensation. For instance thermodynamically stable clusters (TSC) present in the atmosphere are formed from vapor molecules. Those may further grow to detectable sizes ($\sim$ 3 nm) [76, 151]. Due to high rate of coagulation with pre-existing particles (such as sea salt or dust), the loss of freshly nucleated particles is high. The initial growth rate strongly influences the rate of new particle formation and their concentrations in the atmosphere [151]. As suggested by Wang et al. [151] the primary condensational growth of TSC may be described as heterogeneous nucleation of vapors on pre-existing clusters. Nucleated particles may grow to sizes big enough to serve as cloud condensation nuclei and eventually form cloud droplets and clouds [123].

1.3 State of the art

Nucleation is an interdisciplinary topic and nucleation mechanisms have been a focus in the field of theoretical and experimental atmospheric chemistry and physics

however they are not yet fully understood. The challenge is to find out how aerosols form at the molecular level.

Ever since P.J. Coulier's experiments in 1875 [23] and Wilson's chamber research in 1911 [157] the role of small particles and ions acting as nuclei for the formation of cloud droplets has been studied. In 1880 John Aitken [3] built the world's first instrument to measure particle number concentrations of ambient air, known as condensation particle counter (CPC). Further, Gibbs [41] took the first steps to understand the kinetics of phase change, while the first paper on the kinetics of nucleation has been published by Volmer and Weber in 1926 [146]. In 1935 Becker and Döring [9] and further Zeldovich [168, 169] derived the classical theory of nucleation. Quantitative nucleation experiments have been performed [132, 148, 164, 165]. Only recently Kirkby et al. [69] reported well-defined laboratory experiments directly applicable to nucleation mechanisms in the atmosphere and the effect of ions. Those findings are described further in **Chapter IV (Paper II)**.

For a long time direct measurements of the nucleation rate or chemical composition of the critical cluster were not possible and the theoretical approaches to identify the nucleation barrier have also failed [99, 172, 174]. As a result, researchers have indirectly inferred the composition of the critical cluster by measuring the dependence of the nucleation rate on the concentrations of gaseous nucleating species [172].

Several research groups have been working both in the laboratory and in field studies with the aim to understand (1) which vapors and concentrations of these vapors contribute to particle formation and growth, (2) the size and chemical composition of the critical cluster, (3) the nucleation and growth rates at small sizes, (4) the effect of relative humidity and temperature and properties of pre-existing particle, (5) the significance of atmospheric ions and pre-existing pool of clusters present in the atmosphere, (6) the contribution of nucleation to total CCN, and (7) the extent of the impact of nucleation on the climate. The experimental advances made it possible to address at least some of those questions.

Until recently, water vapor (H_2O) and sulfuric acid (H_2SO_4) were thought to be the main vapors responsible for atmospheric particle formation, while their growth was facilitated by organic species [10, 76, 93, 152, 172]. In 2010 Metzger et al. [95] pointed out the evidence of organic vapors participating not only in the atmospheric

particle growth but also in the formation process. This opened a new way of investigating nucleation processes using e.g. ammonia [69] and amines in experimental approaches such as chamber studies where the atmospheric conditions can be simulated. To trigger photochemical reactions (e.g. formation of H_2SO_4 or other vapors) in a constrained environment as they appear in nature experimentalists use UV light as a solution to simulate solar radiation. Recently, a novel UV fibre-optic system has been installed at the CLOUD *(Cosmics Leaving Outdoor Droplets)* chamber causing minimal thermal effects and representing state-of-the-art approach [80].

Nucleation in the atmosphere whether it is homogeneous, heterogeneous or ion-induced involves water vapor and is strictly temperature dependent. Temperature is one of the crucial factors influencing both chemical processes and the phase-partitioning thermodynamics [45]. Recently, the effect of temperature on heterogeneous nucleation has gained some attention. In well explored homogeneous nucleation studies [14, 34, 144, 145, 153, 164, 165] the temperature trend agrees with the one described by Classical Nucleation Theory (CNT). However, since Chen et al. [17], very little investigations have been conducted on the temperature effect of heterogeneous nucleation of water vapor. Recent studies of Schobesberger et al. [121] and Winkler et al. [163] focused on n-propanol vapor, while in 2010 Pichelstorfer [109] investigated n-nonane vapor. Results of Schobesberger et al. [121] indicated different activation efficiencies and strange temperature dependence. Recently McGraw et al. [91] suggested that strong particle surface effects might be a reason for such unexpected behavior in heterogeneous nucleation studies.

To summarize, the current knowledge of particle formation in the atmosphere relies on the challenges to basically understand nucleation processes and to properly incorporate particle formation in climate models. Further issues in this field include the detection of the number of molecules in critical cluster, the gaseous species involved in nucleation and their concentrations. Moreover, theoretical developments at the microscopic levels and experimental studies are needed to understand this multidimensional phenomenon of thermodynamical, chemical and physical aspects. In addition, the observation of the nucleation processes in situ is usually limited by detection thresholds of available instrumentation.

In the past decade, there has been a significant improvement in analytical instrumental development for measuring particle number concentrations < 3 nm

[53, 55, 92, 139, 161]. This was achieved by optimizing the working liquid [89], operating temperatures and flows [53]. Further, there has been a crucial development in instrumentation for both particle- and gas-phase chemical composition, leading to findings that tremendously contributed to a better understanding of nucleation phenomena (such as in Kirkby et al. [69]). Activation by nucleation below the Kelvin limit, as recently observed by Winkler et al. [162], is the key factor in lowering the detectable size [91]. Without this detailed knowledge climate models are not able to adequately describe the particle number concentration or aerosol rate of formation in various geographic regions, thus leading to huge uncertainties in climate predictions [129].

1.4 Research questions and thesis outline

Although strong efforts have been made to reveal the processes of nucleation and its impact on climate, still many questions remain unanswered. The goal of this study was to contribute to a clarification of the mechanisms of particle formation in the atmosphere by studying both homogeneous and heterogeneous nucleation and the influence of temperature on these processes. Further, to evaluate the influence of ions and seed particle properties on the response of particle counters.
The above goal was addressed through investigation of:

a) Nucleation of atmospherically relevant vapor mixtures, its temperature dependence and the effect of ions studied at the CLOUD experiment at CERN **(Chapter III and IV: Paper I and II)**

b) Temperature dependence of heterogeneous nucleation for water vapor and the effect of particle properties using Size Analyzing Nuclei Counter (SANC) **(Chapter V: Paper III)**

c) The effect of particle properties on the response of state-of-the-art condensation particle counters with different working liquids **(Chapter VI: Paper IV)**

Aims briefly described here are critically important to understanding atmospheric nucleation and its implications. A brief summary of the corresponding theory on homogeneous, heterogeneous and ion-induced nucleation and the temperature effect is presented in **Chapter II (Theory of Nucleation)**.

For nucleation to occur a certain combination of parameters such as vapor concentration, temperature and relative humidity is required. To explain atmospheric observations in the laboratory experiments such as at CLOUD chamber at CERN similar conditions need to be recreated. To mimic the natural solar radiation, a fibre-optic UV system has been installed at CLOUD. As the light induces photochemical reactions by the same mechanisms as they appear in the atmosphere generation of for instance sulfuric acid through ozone photolysis in the presence of water vapor and sulfur dioxide (SO_2) is possible. The characterization and performance of this unique UV fibre-optic system for H_2SO_4 production causing negligible thermal effects is presented in **Chapter III (Paper I)**.
According to theory, however, the boundary layer concentrations of sulfuric acid of 10^6-10^7 molecule cm^{-3} are not sufficient for the binary nucleation of H_2SO_4-H_2 O to occur [95]. In addition, the role of further species (e.g. ammonia, organics) and ions have not been quantified until now.

To fill in those critical gaps in the basic knowledge and advance our understanding of nucleation mechanisms a comprehensive effort has been made through the CLOUD project at the European Center for Nuclear research (CERN), Switzerland. The goal of the CLOUD experiment is to quantify the role of sulfuric acid, ammonia and ions in the atmospheric nucleation, and most importantly the temperature effect of nucleation of atmospherically relevant vapor mixtures **(Chapter IV, Paper II)**. There has been a suggestion that ions may serve as a possible physical mechanism for solar-climate variability, however their role in atmospheric nucleation has not been quantified [4, 68, 69].

The homogeneous and ion-induced nucleation studies at CLOUD significantly contribute to the understanding of atmospheric new particle formation. However, heterogeneous nucleation studies are important as well since aerosols are also formed on seed particles. Moreover, every cloud droplet in the atmosphere is formed on an aerosol particle [111], thus, heterogeneous nucleation plays a significant role in cloud formation. Adding to that, there is always a pool of pre-existing clusters (< 1.5 nm in diameter) present in the atmosphere. The initial growth of these could be also described as heterogeneous nucleation of vapor molecules onto these clusters [151]. Open questions still remain in this topic and include the effect of: a) temperature, b) particle properties (such as solubility or wettability), c) type and properties of condensing liquid, or d) charge state on particle activation.

In **Chapter V (Paper III)** the temperature effect of heterogeneous nucleation of water vapor on neutral sodium chloride (NaCl) and oxidized silver (Ag) seed particles with sizes down to 3.5 nm using SANC are presented. Water was chosen as it is the most abundant vapor and is a crucial component of atmospheric nucleation. In addition, recently water has been suggested by De La Mora [25] to be the most favorable liquid for small neutral particle detection.

The detection of particles < 3 nm is of significant importance for investigating mechanisms of currently still poorly understood new particle formation. In recent years several research groups have been working on improving the performance of commercially available condensation particle counters, in particular their ability to measure particle number concentration below 3 nm in diameter [53, 139]. Mostly this has been done by varying parameters such as aerosol flow and saturator/condenser temperatures or by using different types of condensing liquids. In **Chapter VI (Paper IV)** the performance of the state of the art commercially available water based N-WCPC has been characterized and compared to butanol-based U-CPC using particles with various properties.

The study of mechanisms of new particle formation is necessary for a better understanding of nucleation processes in the atmosphere and will help to clarify the aerosol impact on climate and human health.

CHAPTER 2

THEORY OF NUCLEATION

As described by Ford [38] the formation of clouds and fog exemplify a phase change of vapor into liquid droplets in the atmosphere. When - as a result of cooling - water vapor becomes thermodynamically unstable liquid drops are formed and the process is called nucleation. Nucleation plays a crucial role in condensation, precipitation, crystallization, sublimation, boiling or freezing processes [123].

Nucleation is a process leading to new particle formation. In the atmosphere free molecules are continuously colliding with each other and bonding occasionally [38, 141]. As a result clusters of molecules are built (e.g. dimers). These may either further grow by adding or evaporate by losing molecules. The phase change takes place when individual clusters grow through the unstable size range and pass the critical size beyond which they grow into large stable droplets [38]. If droplet nucleation takes place on the surface of a pre-existing seed particle - as frequently happens in the atmosphere - the process is called heterogeneous nucleation [47]. While in the case of homogeneous nucleation, the interactions of the vapor molecules take place only among themselves.
Clusters at the critical size are called critical clusters and may consist of up to few tens of molecules [37, 96]. The size and properties of these are central to the theory of nucleation as reaching the critical size defines whether the cluster will grow further or will evaporate [141]. The classical theory of nucleation (CNT) assumes clusters to be tiny droplets with a well-defined surface area and density characterized by properties of bulk condensed matter (capillary approximation) [35, 38, 47, 61].
So far the classical theory has been most frequently used for the qualitative under-

standing of nucleation. Its main strength is that only basic thermodynamic data such as liquid density, surface tension or saturation vapor pressures are required for it to be applied [141]. Further, it is the only approach that predicts critical cluster size (critical radius, r^*) and nucleation rates (how many clusters grow above the critical size in a unit volume and time). CNT combines both kinetic and thermodynamic theories derived by Becker and Döring [9] and Zeldovich [168, 169] and will be briefly described in the following sections.
Since the critical cluster can contain only few tens of molecules [96] the capillary approximation may be questionable at this extremely small scale [37]. Thus, a variety of alternative approaches have been used to explain nucleation e.g. molecular dynamics or density functional theory [37, 47, 141], however these are not in the focus of this thesis.

The goal of this chapter is to present a comprehensive approach to nucleation processes taking place in the atmosphere. A brief description on classical nucleation theory, covering the topics of homogeneous, heterogeneous and ion-induced nucleation, as well as phase transition thermodynamics is given.

2.1 Types of Nucleation Processes

Single or multicomponent nucleation can be either homogeneous, heterogeneous or ion-induced. In homogeneous nucleation the cluster is formed from vapor molecules itself, in heterogeneous nucleation on a seed nuclei, and in the case of ion-induced nucleation upon an ion or ion cluster (Figure 2.1).

a) Homogeneous Nucleation

In the initial state of homogeneous nucleation (self-nucleation) only vapor is present [141] (Figure 2.1). As a result solid or liquid particles are formed from highly supersaturated vapor in the absence of pre-existing seed particles (condensation nuclei). If the condensing vapor consists of one type of vapor molecules it is called unary nucleation such as of water vapor (H_2O). When two vapors are present a binary nucleation takes place e.g. sulphuric acid (H_2SO_4) and water. In case three vapors are involved it is described as ternary nucleation e.g. H_2SO_4-H_2O-X, where X represents a third component such as ammonia or organics e.g. amines [95].

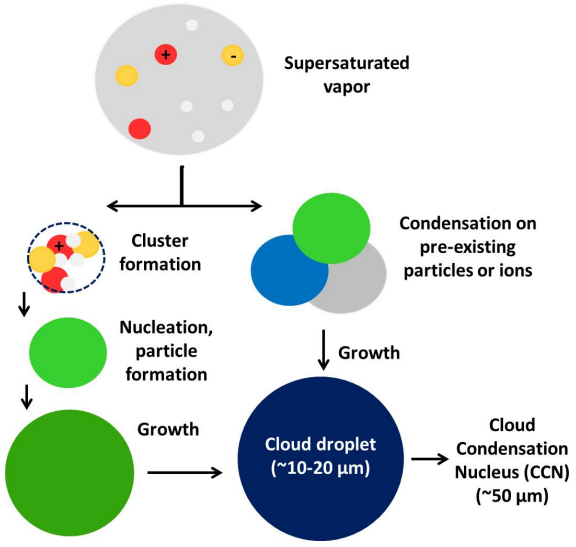

Figure 2.1: Simplified pathways of particle formation and growth of atmospheric vapors. Adapted from [142]

b) Heterogeneous Nucleation

Heterogeneous nucleation is the most common formation mechanism in the atmosphere and takes place in the presence of a seed particle surface onto which clusters are formed [74] (Figure 2.1). For instance formation of fog on pre-existing dust particles is driven by heterogeneous nucleation [142]. In this type of nucleation the seed particle is assumed to be insoluble (such as dust or soot) in the condensing liquid. For the case of soluble seed (such as salt) the situation is more complex and will be described in the following sections.

c) Ion-Induced Nucleation (IIN)

IIN takes place in the presence of ions. This process leads to the formation of stable clusters of the condensed phase upon ions or ion clusters as observed in 1911 by Wilson [157]. The ions in the atmosphere can be formed either by cosmic radiation, lightning, or combustion [47].

In general it is easier e.g. for water to nucleate on a seed surface or ions rather than on its own [161]. Assuming relative humidity (RH) of 200 % and a temperature

of 20 °C, it would take 10^{54} seconds for one droplet to appear in 1 cm^3 of air [123]. However, in the presence of a nuclei droplets in the atmosphere can form already at RH slightly above 100 %.

According to Kulmala et al. [76] the initial steps of aerosol growth may occur via condensation of nucleating vapors (after homogeneous nucleation took place), activation of soluble vapors, heterogeneous nucleation, charge-enhanced condensation, self-coagulation or multi-phase chemical reactions. Other processes such as evaporation, scavenging or coagulation may also occur along the way. Particle formation and growth processes may impact aerosol size distribution, and influence air quality and climate.

2.2 Classical Nucleation Theory and its Assumptions (Capillarity Approximation)

In recent years progress in understanding atmospheric droplet formation has been significant [69, 77, 91, 151, 161]. So far the most frequently used approach in the modeling studies have been based on classical nucleation theory which relies on macroscopic parameters for describing the properties of critical clusters [37, 39, 146, 168]. In CNT the critical cluster is treated as a scaled-down macroscopic droplet of the condensed phase [37] - a spherical liquid droplet with surface tension and bulk liquid density.

Nucleation theory consists of a set of rate equations describing changes of concentrations of clusters with different sizes as a result of gain or loss of molecules (monomers) [123]. At first a cluster is formed either by homogeneous, heterogeneous or ion-induced nucleation and may further grow to a detectable size [172]. As described by Vehkamäki and Riipinen [142] when two molecules (or a molecule and a cluster) meet they need to overcome different kinds of energy barriers before they can form a cluster. The barrier can be either a) structural e.g. atoms in the cluster need to rearrange themselves before they form a cluster, or b) energetic e.g. when the colliding particles have too much energy (excess) thus other particles colliding with the cluster need to carry this energy away - the free energy change (Gibbs free energy (G); [35, 141].

Classical nucleation theory assumes that [141]: *a*) in an ideal gas molecules cannot form clusters as they do not interact with each other, *b*) when a particle forms the temperature is kept constant, *c*) the volume of a cluster is calculated using bulk liquid density, *d*) cluster is spherical, *e*) its density gradually decreases when moving outwards from the center of the cluster, *f*) surface tension at the surface of the cluster is independent of the cluster size, *g*) the density of a liquid is much greater than the density of a gas and independent of the liquid pressure, and finally *h*) the exchange of molecules between the interior and the cluster surface layer is much faster than between the cluster and the gas phase.

2.2.1 Saturation Ratio and Equilibrium Vapor Pressure

The most abundant condensable vapor in the atmosphere is water (10^{19} molecules cm^{-3}), while concentrations of other condensable trace vapors such as ammonia, amines or sulphuric acid are below 10^{10} molecules cm^{-3} [142]. When a condensed phase is formed vapor molecules build up clusters that can be either solid or liquid. This process is driven by the vapor saturation ratio $S(T)$ and is temperature dependent (Equation 2.1).
When both vapor and liquid phase are present, the vapor molecules collide with the liquid surface and become a part of the liquid, or opposite, molecules in the liquid may escape and become part of the vapor. In case of equilibrium conditions the partial pressure of the condensable vapor is called the saturation vapor pressure $p_s(T)$ (that builds up over a plain surface of condensed matter) and depends on the type of molecules. Saturation ratio $S(T)$ is the ratio of the actual partial vapor pressure p_v and equilibrium vapor pressure $p_s(T)$:

$$S(T) = \frac{p_v}{p_s(T)} \tag{2.1}$$

Further assuming the gas to be ideal the difference of the chemical potentials μ_v and μ_l of vapor and liquid respectively can be determined as:

$$\mu_v - \mu_l = kTlnS \tag{2.2}$$

where k is the Boltzmann constant, T is the absolute temperature and S is the saturation ratio. The chemical potentials define the direction of phase change e.g. if $S < 1$ then $\mu_l > \mu_v$ forcing liquid molecules to evaporate. When $S > 1$ then $\mu_v > \mu_l$ and thus in the absence of liquid phase, a liquid phase may form through the forma-

tion of a molecular cluster. Vapor molecules will condense here as a result of higher chemical potentials. When $S = 1$, $\mu_v = \mu_l$ and there is no net transfer of molecules from one phase to the other.

2.2.2 Homogeneous Nucleation: Thermodynamical Aspects

For a cluster of i molecules the Gibbs free energy G_i is higher than the energy of the i molecules in the liquid phase ($i\mu_l$) because of the additional energy from the clusters surface area, A_i [36]:

$$G_i = i\mu_l + A_i\sigma \tag{2.3}$$

where σ is the surface tension. The energy necessary to form a cluster of i molecules from the vapor phase is given by:

$$\Delta G_i = G_i - i\mu_v \tag{2.4}$$

The above is the Gibbs free energy of a cluster reduced by the energy of i vapor molecules. When using 2.2,2.3 and 2.4 the energy needed to form a cluster can be written as:

$$\Delta G_i = A_i\sigma - ikTlnS \tag{2.5}$$

When assuming a spherical cluster with radius r, the above equations can be written in this form:

$$\Delta G_i = 4\pi r_i^2\sigma - \tfrac{4\pi}{3} n_l r_i^3 kTlnS \tag{2.6}$$

where n_l is the number of molecules per unit volume in the liquid phase. Since the resulting cluster may consist of $\geq$ 100 molecules a macroscopic parameters describing its properties are used.

The dependence of the free energy of cluster formation ΔG_i as a function of cluster radius r_i is presented in Figure 2.2, for a single component system (such as water vapor) for different saturation ratios S:

a) $S < 1$, $(p_v < p_s(T))$, the vapor is not saturated and liquid will evaporate until the equilibrium vapor pressure is reached (or until liquid runs out). This means that the vapor is stable and liquid does not form. In the liquid-vapor system molecules of the liquid evaporate into the vapor phase.

b) $S > 1$, $(p_v > p_s(T))$, the vapor is supersaturated. This means that the vapor

pressure is higher than the saturation vapor pressure and molecules are more likely to be in the liquid rather than in the vapor phase and a molecular cluster may form. The critical cluster radius r^* corresponds here to the maximum in Gibbs free energy (ΔG^*) (Figure 2.2) and defines whether the cluster will grow by condensation or will evaporate.

c) $S = 1$, $(p_v = p_s(T))$, there is no flux of molecules between the liquid and vapor as the vapor pressures of both phases are equal. Nucleation does not occur, since saturation ratio needs to exceed 1 for it to take place.

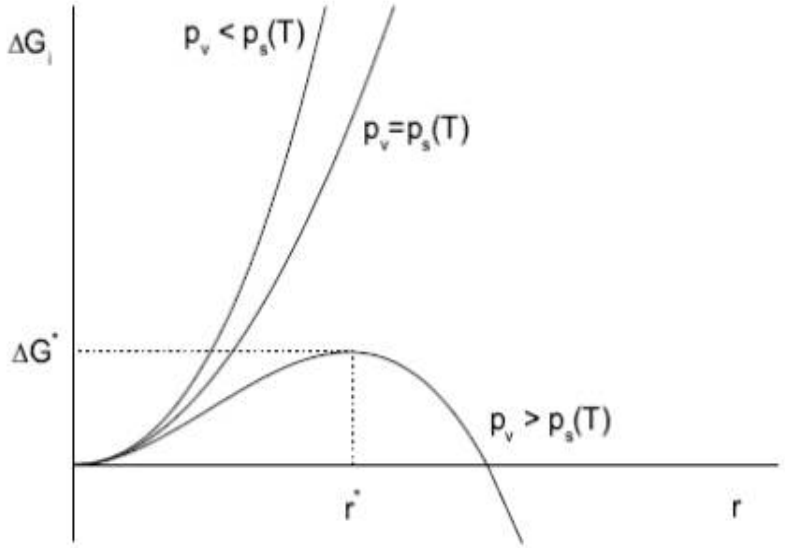

Figure 2.2: Schematic representation of the Gibbs free energy changes as a function of cluster diameter r and saturation ratio $S(T) = \frac{p_v}{p_s(T)}$. ΔG^* represents the nucleation barrier and r^* is the critical radius.

This means that the first macroscopic droplets of liquid are formed when clusters overcome the energy barrier at r^* [142]. Moreover, to form a liquid, the interface between the liquid and gas needs to be created. The molecules at the gas-liquid interface lack bonding partners which results in excess surface energy, which is higher than in the bulk liquid.
When the critical cluster at r^* forms, the Gibbs free energy of the nucleating system reaches maximum (ΔG^*) - nucleation barrier - beyond which the growth of the particle becomes spontaneous. Beyond the critical size r^* clusters are more likely to

grow spontaneously than evaporate, however clusters smaller than r^* will evaporate. Using Equation 2.6 and assuming that $\frac{\delta \Delta G_i^*}{\delta r} = 0$ the following equation can be derived defining the critical radius of a neutral cluster:

$$r^* = \frac{2\sigma}{n_l k T ln S} \tag{2.7}$$

Equation 2.7 depends on the surface tension (σ), number of molecules per unit volume of the liquid (n_l), absolute temperature (T) and the saturation ratio (S). This critical cluster will grow spontaneously if additional vapor molecules are added to the cluster. However this growth may be limited by the available vapor molecules. When a molecule leaves a critical cluster r^* the vapor pressure of its surface exceeds the ambient vapor pressure and the cluster evaporates. The saturation ratio expressed as a function of diameter critical cluster is defined by the Kelvin equation:

$$ln S = \frac{2\sigma}{n_l k T r^*} \tag{2.8}$$

The increase of saturation vapor pressure due to increased curvature of the surface is called the Kelvin effect [74, 123, 141]. Thus it is easier for molecules to escape from a curved surface as their bonds among each other are weaker and the saturation vapor pressure is higher [141]. Figure 2.3 presents the Kelvin diameter as a function of water vapor saturation ratio at four different temperatures.

It can be observed that nucleation depends both on the temperature and saturation ratio [14]. After some rearangement of the above equations, the critical cluster formation energy ΔG^* can be expressed purely in terms of surface tension σ and critical cluster radius r^*:

$$\Delta G^* \cong \frac{4\pi}{3} \sigma r^{*2} \tag{2.9}$$

The above section described the situation when neutral clusters form homogeneously. The rate at which these clusters are formed - nucleation rate (J) - will be considered next.

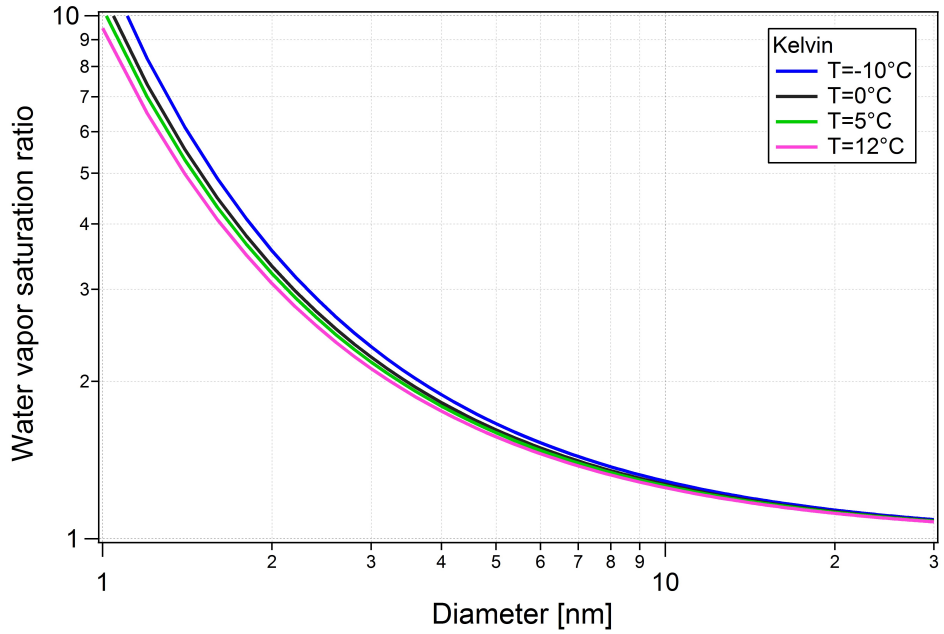

Figure 2.3: Kelvin diameter as a function of water saturation ratio and droplet diameter for various temperatures. For a certain droplet diameter higher temperature make it easier for nucleation to occur. This means that lower saturation ratio is necessary to activate droplets when temperatures are higher.

2.2.3 Homogeneous Nucleation Kinetics

Clusters of a particular size are formed by collisions of smaller clusters and/or evaporation of bigger clusters [123] (Figure 2.4). Thus, the size of clusters may change when they collide with other clusters or when they evaporate:

$$\frac{dN_i}{dt} = \beta_{i-1}N_{i-1}(t) - y_i N(t) - \beta_i N_i(t) + y_{i+1}N_{i+1}(t) \tag{2.10}$$

where $N_i(t)$ is the number concentration of clusters containing i molecules (monomers) at certain time t; β_i is the collision coefficient between i-mer and $i+1$-mer, and y_i is the rate coefficient for evaporation of i-mer decays producing an $i-1$-mer.

The following assumptions are being made: *a*) cluster-cluster collisions are so rare that they can be ignored; *b*) cluster fissions into two or more clusters are negligible; *c*) at equilibrium conditions every forward process is equal to its reverse process (if

cluster grows by one molecule, it can also evaporate by one at a time [123]); *d*) there are no spatial variations in vapor and cluster concentration.

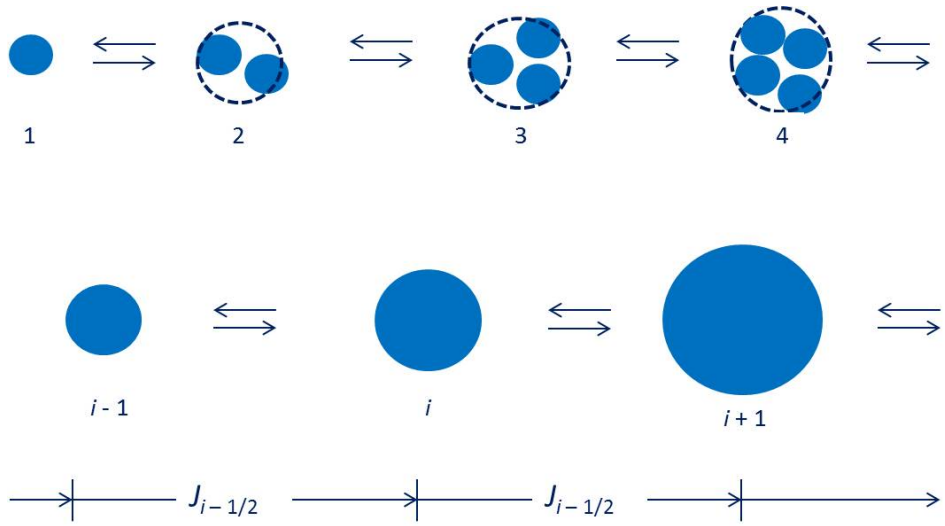

Figure 2.4: A schematic of the cluster growth and evaporation process. Clusters grow and evaporate through gaining or loosing of single molecules. Adapted from [123]

Nucleation rate provides the number of critical clusters formed per unit volume of parent phase in a unit time. After some rearangements and using Boltzmann distribution the nucleation rate for homogeneous nucleation can be expressed as:

$$J = K' e^{-\frac{\Delta G^*}{kT}} \tag{2.11}$$

where K' describes the particle kinetics. As the nucleation requires high number of monomers, J may be *a*) strongly time limited, or *b*) nucleation can be slow enough that the additional monomers can be provided. The nucleation rate J depends on the surface tension, temperature and the saturation ratio. Small variations in those parameters may strongly influence nucleation rates.

2.2.4 Heterogeneous Nucleation: Thermodynamic Aspects

In heterogeneous nucleation the critical cluster (spherical cap embryo) is formed on a pre-existing seed particle (condensation nucleus) and not as in the case of homogeneous nucleation in the middle of the vapor [141]. Here only a part of the surface has to be built from scratch, as part of it can be borrowed from the existing particle surface [161]. The presence of a surface decreases the energy barrier of cluster formation [78, 147]. Heterogeneous nucleation rate is higher than homogeneous one since the availability of the surface reduces the cost of surface formation. The location of the maximum formation free energy of the neutral cluster formed either due to homogeneous and heterogeneous nucleation is the same. This indicates that the critical radii are the same [141]. However, the number of molecules in the critical cluster is smaller in the case of heterogeneous nucleation. The latter can take place at much lower vapor concentrations.
As proposed by Fletcher [35] the formation free energy of heterogeneously formed cluster is proportional to the energy of formation of a homogeneously nucleated cluster and can be described by:

$$\Delta G^*_{het} = \Delta G^*_{hom} f(m, X) \tag{2.12}$$

where ΔG^*_{hom} is the free energy for homogeneous critical cluster formation.

The geometric factor $f(m, X)$ may vary between 1 and 0. It describes the reduction of the nucleation barrier from ΔG^*_{hom} to ΔG^*_{het} as a result of the presence of the seed. f can be expressed as:

$$f = \frac{1}{2}\left[1 + \left(\frac{1 - Xm}{g}\right)^3 + X^3\left(2 - 3\left(\frac{X - m}{g}\right)\left(\frac{X - m}{g}\right)^3\right) + 3mX^2\left(\frac{X - m}{g} - 1\right)\right] \tag{2.13}$$

where:

$$g = \sqrt{1 + X^2 - 2Xm} \tag{2.14}$$

The ratio of a spherical seed particle radius R and the radius of the critical cluster r^* is given by (Figure 2.5):

$$X \equiv \frac{R_{seed}}{r^*} \tag{2.15}$$

In CNT the seed particle is assumed to be spherical and the angle between the nucleating surface and the surface of the nucleating cluster is referred to as contact angle [161] (Figure 2.5). Young's equation relates the contact parameter to the

surface tension:

$$m \equiv \cos\phi = \frac{\sigma_{sv} - \sigma_{sl}}{\sigma_{lv}} \tag{2.16}$$

The angle ϕ lies between the surface and the tangent of the cluster surface at the point where these surfaces meet and is related to the surface tension between the solid (s) and the liquid (l), and vapor (v) and solid (s) as described above.

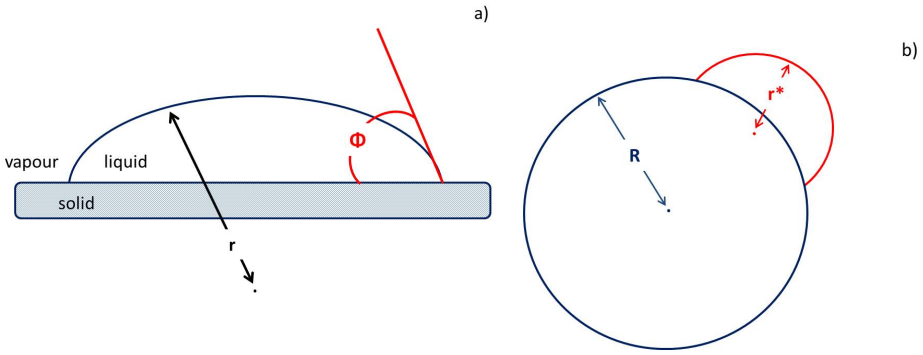

Figure 2.5: A spherical cap embryo of liquid on a planar surface (a) and a cluster with a surface curvature r^* on a surface of a spherical seed particle of radius R (b). Three phase system includes solid (s), liquid (l) and vapor (v) phase. Liquid phase is actually the cap embryo and r is the radius implied by the surface curvature of the embryo, while indicates the contact angle

The typical dependence of $f(m, X)$ is presented in Figure 2.6. To be an efficient condensation nucleus it is crucial for the particle to have not only a large diameter but a small contact angle e.g. for water [35] (Figure 2.7). Contact angle defines the wettability of the particle, it can be seen that the smaller the contact angle (more wettable seed) the easier the activation takes place.

The same temperature effect as in the case of Kelvin temperature dependence is observed for Fletcher curves at constant contact angle - ϕ here at 36°. At certain particle size the supersaturation that is required for activation is lower at higher nucleation temperatures. Further, for decreasing particle size increasing saturation ratios are required to activate the seed for both Kelvin and Fletcher theories.

The use of macroscopic parameters is only an approximation. Further, it is assumed that cluster grows only by the addition of molecules neglecting surface diffusion. Potential geometries of the cluster formation for various contact angles ϕ are presented in Figure 2.8.

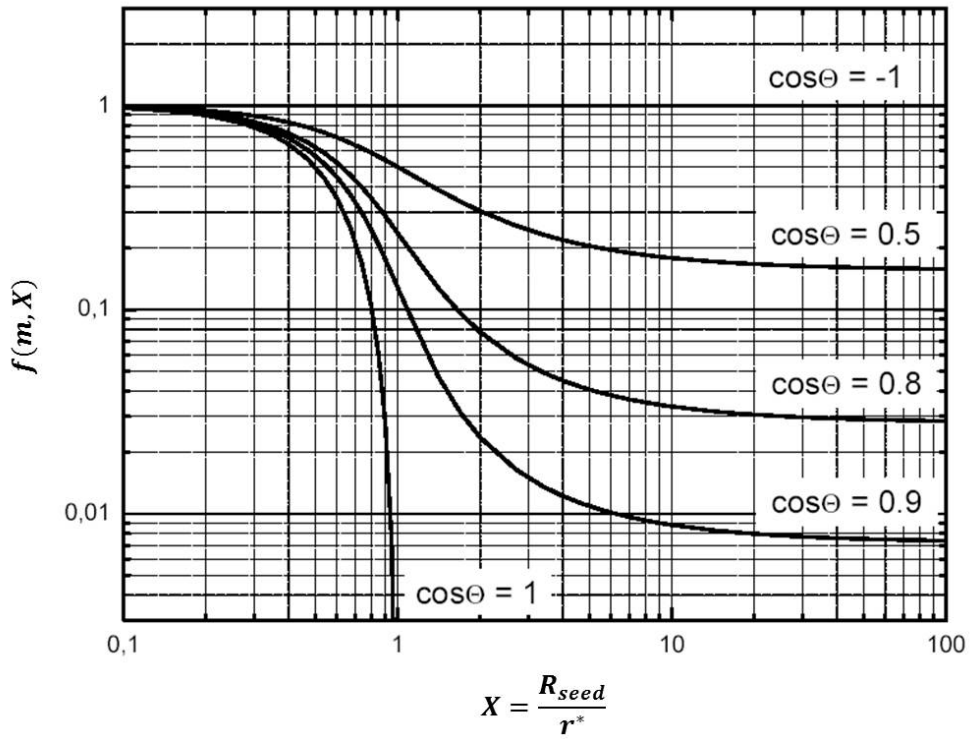

Figure 2.6: Dependence of factor $f(m, X)$ on the relative particle size X and the parameter m between the seed particle and the nucleating phase. The higher m ($cos\phi$) parameter the smaller the contact angle (e.g. for $m = 1$, $\phi = 0$) - the more wettable the seed particle is. Adapted from [35].

According to De la Mora [25] the critical supersaturation at which droplets are activated depends on the liquid properties. Thus selection of a proper working liquid in condensation based particle counters (CPC) is of crutial importance for small particle detection.The thermodynamics and kinetics of heterogeneous nucleation follow those of homogeneous case however with additional surface energy term and geometric relations.

Not much experimental data exist on heterogeneous nucleation [17, 107–109, 121, 161–163] to be used for evaluation of the theoretical predictions. One of the goals for experimentalists is to be able to use perfectly smooth spherical surfaces in order to confirm the theoretical assumptions [123].

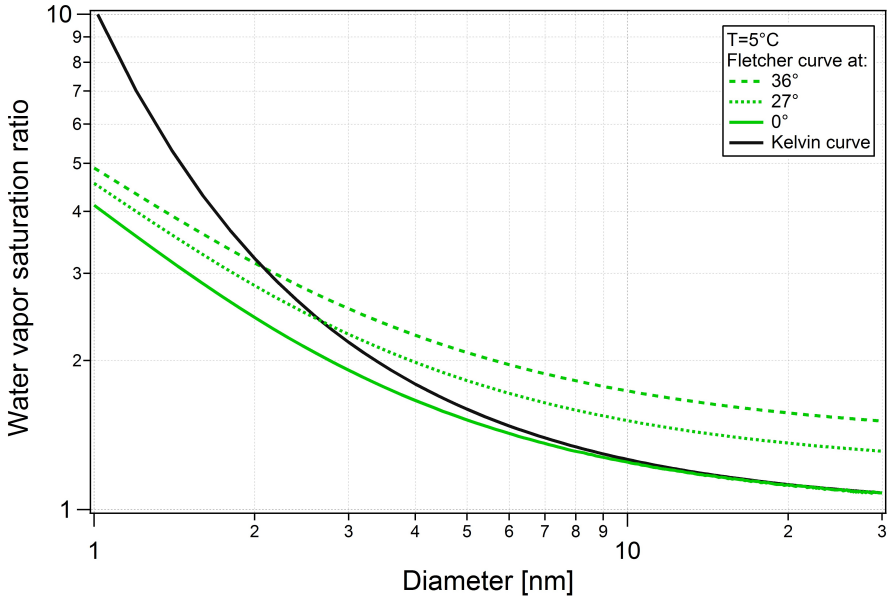

Figure 2.7: Fletcher diameter as a function of water saturation ratio and particle diameter. Kelvin curve is given for comparison.

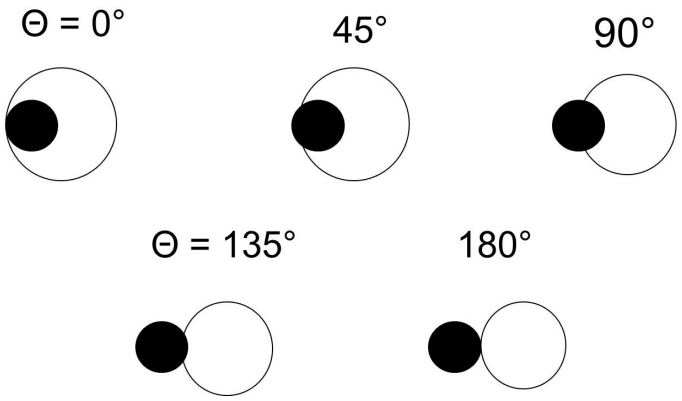

Figure 2.8: Schematic diagram illustrating potential geometries of cluster formation at various contact angles. Filled black circles represent seed particle, while hollow circles represent formed embryo (P.E. Wagner, private communication)

2.2.5 Heterogeneous Nucleation Kinetics

Heterogeneous nucleation rate and nucleation probability

The nucleation rate per seed particle can be expressed as (J''):

$$J'' = J'A \equiv K'Aexp\left(-\frac{\Delta G^*}{kT}\right) \tag{2.17}$$

where the seed particle surface $A = 4\pi r^2$. J' is defined as the rate of critical cluster formation per unit area of a planar surface. K' depends weakly on the seed particle radius, saturation ratio, temperature and number density of vapor molecules adsorbed at the seed surface. The actual value of K' requires information on the impingement rate, Zeldovich factor and other parameters as described in Winkler et al. [162].
To allow for easier experimental evaluation nucleation probability is introduced and defined as follows:

$$P = \frac{N_{act}}{N_{tot}} \tag{2.18}$$

where N_{act} is the number of activated particles at certain supersaturation (e.g. number of seed particles the cluster has formed on) that may grow further to droplets, while N_{tot} is the total number of seed particles activated.

Assuming the formation of multiple embryos on one particle is neglected, the probability that heterogeneous nucleation occurs at certain period of time t can be related to the nucleation rate:

$$P = 1 - exp(-J'At) \tag{2.19}$$

where t is the nucleation time and assuming that J is expressed as a rate per unit seed surface area and unit time ($m^{-2}s^{-1}$).

In the above approaches the assumptions have been considered only for planar or spherical surfaces and single component (one vapor) system. For atmospheric conditions those would need to include e.g. chemistry of the seed particle and calculations would be more complex. The assumptions based on macroscopic parameters such as surface tension, contact angle or densities may lead to strong discrepancies between theoretical predictions and experimental results.

According to recent findings of Winkler et al. [162] the critical cluster diameter

needs to be distinguished from seed particle diameter, and the latter is considerably smaller than critical cluster diameter. Further, electrical charge enhances the heterogeneous nucleation process and the sign preference is observed.

In **Chapter V (Paper III)** heterogeneous nucleation probabilities are studied for well-defined conditions of water vapor and either silver (Ag) or sodium chloride (NaCl) seed particles at various sizes and nucleation temperatures.

2.2.6 Ion-Induced Nucleation

Ion-induced nucleation is a special case of heterogeneous nucleation. Here the cluster is formed on a charged particle or a molecular ion [116, 141, 166]. The nucleation barrier is lower than in case of homogeneous nucleation as the electrostatic forces enhance the attraction of the nucleus and the vapor molecules.

According to Hegg and Baker [47] in ion-induced nucleation the ions (N^+, N_2^+, O^+, O_2^+) and related free electrons are converted to cluster ions of protonated bases (e.g. H_3O^+, $(H_2O)_n$) and of conjugate bases of strong acids (e.g. HSO_4^-, $(H_2SO_4)_n$ $(H_2O)_m$). In general ions can undergo: *a*) recombination with other ions of opposite polarity and *b*) reactions with aerosol particles. Formed clusters can be either negative or positive.

The enhancement of the ion presence in the nucleation rate is due to the attractive force between the ion center and the nucleating phase. This leads to the reduction in Gibbs free energy of formation. The consideration of charged clusters introduces the additional parameters and the formation free energy in a one component system nucleating around an ion is described by Thomson equation [135, 142]:

$$\Delta G = -kTlnS + A\sigma + \frac{q^2}{8\pi\epsilon_0}\left(1 - \frac{1}{\epsilon_r}\right)\left(\frac{1}{r_p} - \frac{1}{r_{ion}}\right) \tag{2.20}$$

where q is the charge of the ion, ϵ_0 is the permittivity of the vacuum, ϵ_r is the dielectric constant of the particle and r_{ion} is the radius of the ion, r_p is the size of the embryo. In case of homogeneous nucleation, the first two terms give the formation free energy. At moderate vapor concentrations there is a minimum in the free energy plotted as a function of cluster size. At high concentrations the minimum and the maximum disappear and formation free energy decreases with size. Thus,

a barrierless condensation takes place. If the ion is sufficiently big, there is no pre-critical minimum.

Recently many adjustments have been made and some include consideration of ion formation and recombination rates as described in Raes and Janssens [117]. Further, as suggested by Lovejoy et al. [88] and Curtius [24] ion-induced nucleation may be of importance in the upper troposphere or stratosphere but not in the lower troposphere. The number of ions available (defined by ion formation rate) can limit ion-induced nucleation rate [117]. Ion enhancement for binary - sulpuric acid and water - and ternary - sulpuric acid, water and ammonia - systems reported by Kirkby et al. [69] is described in Chapter IV/Paper II.

2.2.7 Activation of Soluble Seed Particles

As mentioned by Andreae and Rosenfeld [5] in the real atmosphere the presence of particles facilitates the nucleation and further condensational growth into droplets. Described so far the Fletcher effect refers to the saturation ratio necessary to activate insoluble seed particles, while the Kelvin effect is related to the diameter of the curvature that a cluster has to reach (critical cluster) to be able to grow further to become a macroscopic droplet. For soluble seed particles however, Köhler theory is considered [70]. According to Köhler the saturation ratio S over an aquaous solution droplet can be described by [87]:

$$S_{v,w} = 1 + \frac{A}{d} - \frac{B}{d^3} \tag{2.21}$$

$$A = \frac{2M_w\sigma_w}{RT\rho_w} \tag{2.22}$$

$$B = \frac{3m_s\vartheta}{4\pi M_s\rho_w} \tag{2.23}$$

where d is the seed particle diameter, M_w is the molar mass of water, M_s is the molar mass of solvent, m_s is the mass of dissolved substance (e.g. sodium chloride, NaCl), σ_w is the surface tension, R is the universal gas constant, ρ_w is the density of water and ϑ is the Vant' Hoff factor. NaCl masses in Köhler equation correspond to the dry particle seed diameters of 3.4 nm (m_s=4.5x10^{-23} kg), 5.8 nm (m_s=2.2x10^{-22} kg) and 7.8 nm (m_s=4.6x10^{-22} kg). For each seed particle diameter

the corresponding onset saturation ratio according to Köhler can be defined from the corresponding curve maximum (Figure 2.9). Köhler theory states that critical supersaturation decreases as the soluble particle size increases, or when the mass of a soluble fraction in a particle composed of soluble and insoluble material increases [114, 123].

As described in Wagner et al. [147] Köhler curves can be obtained when plotting saturation ratio as a function of droplet diameter for a certain amount of salt in the droplet (Figure 2.9). The curve that is a result of the competition between the Raoult and Kelvin effects exhibits a maximum at the relative humidity slightly above 100 %. Further, the maximum becomes higher as the diameter of the salt particle gets smaller. As soon as the relative humidity rises above the maximum, the solution droplet is activated and grows rapidly as a result of nonequilibrium condensation of water [70]. Further, seed particles do not activate for growth below the maximum of the Köhler curve has been reached (Figure 2.9), but they gather the vapor molecules around them (minimum).

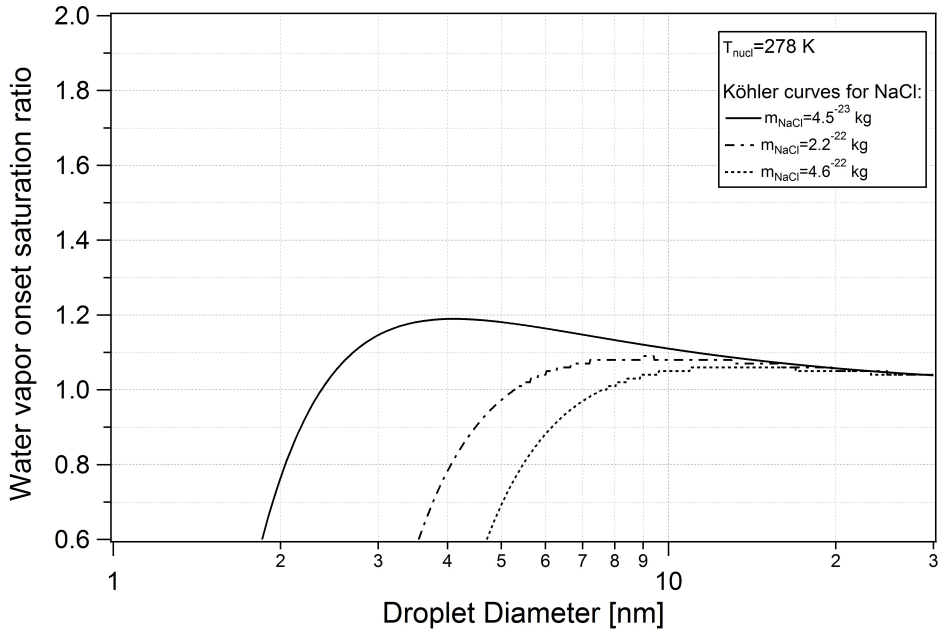

Figure 2.9: Köhler curves for 5 °C calculated for NaCl particles (3.4 nm m_s=4.5x10^{-23} kg, 5.8 nm m_s=2.2x10^{-22} kg and 7.8 nm m_s=4.6x10^{-22} kg

2.3 Limitations of classical nucleation theory

Classical nucleation theory gives a good qualitative description of particle formation systems however, it has some shortcomings [142]. Vapor to liquid homogeneous nucleation experiments have suggested that CNT well predicts the saturation ratio dependence on nucleation rate while fails in the prediction of the temperature dependence of nucleation rate [38, 59, 132, 148].

In general CNT provides a qualitative understanding of the nucleation however it has drawbacks in the quantitative evaluations [47]:

a) The concept of a compact embryo with an inside and a surface may not be applicable at a very small scale.

b) The macroscopic parameters (e.g. molecular density) may not have much meaning for clusters consisting of ten or less molecules.

c) The equations are based on equilibrium concepts (e.g. J) while according to definition those are used to describe a nonequilibrium situation where the net transfer of molecules takes place from one phase to the other. This may only describe the initial stage of the nucleation process.

d) The theory does not characterize density fluctuations in the parent phase.

According to CNT nucleation is a local process that occurs in microscopic volumes occupies by a small number of molecules. However, the thermodynamic parameters used to describe those volumes are those of the parent macroscopic phase.

In recent years many revisions to CNT have been developed. Some of them improve the agreement with experimental results, however only for particular conditions (e.g. substance or temperature) but are not representative for the whole range of interest.

2.4 Nucleation Theorems

Nucleation theorems can be used to obtain properties of critical clusters from macroscopic measurements. These theorems have been derived [38, 62, 90, 101, 140, 141] under quite general assumptions. Nucleation theorems allow to extract size as well

as excess free energies of critical clusters from experimental data.

1^{st} Homogeneous Nucleation Theorem

First nucleation theorem states that the supersaturation dependence of the nucleation rate is related to the critical size [38, 62, 101]. Further, it can be used to calculate the number of molecules in the critical cluster from the slope of nucleation rate data plotted as a function of supersaturation in a log-log scale [37] at constant temperature:

$$n^*_{hom} \equiv \left(\frac{\partial ln J_{hom}}{\partial ln S}\right)_T \tag{2.24}$$

The steeper the function $P(S)$ the more molecules are building up the critical cluster.

1st heterogeneous nucleation theorem

The heterogeneous nucleation rate J_{het} is related to the nucleation probability P by (see also Equation 2.19):

$$P = 1 - e^{-J_{het} A \Delta t} \tag{2.25}$$

Where A is the seed particle surface and Δt the nucleation time. This relation allows a reformulation of the nucleation theorem as follows:

$$n^*_{het} \equiv \frac{\partial ln\left(ln\frac{1}{1-P}\right)}{\partial ln S} \tag{2.26}$$

Thereby the number of molecules in the critical embryo can be determined from P vs. S curves.

CHAPTER 3

A FIBRE-OPTIC UV SYSTEM FOR H_2SO_4 PRODUCTION IN AEROSOL CHAMBERS CAUSING MINIMAL THERMAL EFFECTS (PAPER I)

PAPER I (PUBLISHED)

A fibre-optic UV system for H_2SO_4 production in aerosol chambers causing minimal thermal effects

Kupc, A., Amorim, A., Curtius, J., Danielczok, A., Duplissy, J., Ehrhart, S., Walther, H., Ickes, L., Kirkby, J., Kürten, A., Lima, J.M., Mathot, S., Minginette, P., Onnela, A., Rondo, L., Wagner, P.E.

(2011), *Journal of Aerosol Science*, 42, 8, 532-543
DOI:10.1016/j.jaerosci.2011.05.001

keywords: aerosol chamber experiments, ultraviolet system, (H_2SO_4) production, nucleation, optical fibre

ABSTRACT

A novel fibre-optic UV illumination system for sulphuric acid (H_2SO_4) production has been developed. The illumination system described in this paper provides sufficient ultraviolet light (UV) power while causing practically no thermal effect on the aerosol chamber (temperature variation < 0.005 °C at full UV illumination). A similar thermal stability has not been achieved in other comparable experimental set-ups so far. The spectrum provided by the fibre-optic UV system corresponds to the UVB region, illuminates the chamber in a reasonably uniform way and is comparable to the ground level actinic flux. The UV system has been installed for the Cosmics Leaving OUtdoor Droplets (CLOUD) chamber experiments at CERN. Precise, easily-adjustable and reproducible concentrations of H_2SO_4 were generated by adjusting the UV light intensity. This paper gives an overview on the design of this new system as well as insights on its performance and application.

3.1 Introduction

Various aerosol chambers are used to simulate atmospherically-relevant physical and chemical processes [26, 45]. During these experiments, generally, specific fundamental mechanisms can be isolated, e.g. organic aerosol nucleation [95]. In aerosol chambers natural solar radiation that initiates gas-phase reactions is usually mimicked by UV illumination systems that trigger photochemical processes, e.g. through the production of hydroxyl radicals (OH) which are the most abundant oxidizing agents in the atmosphere (between 10^6 and 10^7 molecule cm^{-3}) [60]. In turn, OH oxidizes SO_2 which leads to the production of H_2SO_4 that is an important compound for the nucleation and initial growth of aerosol particles in the atmosphere (present with gas-phase concentrations of $10^5 - 10^7$ molecule cm^{-3}) [10, 93, 172]. For experimental purposes, H_2SO_4 can be produced either by evaporation from a liquid reservoir [7] or in situ by photo-dissociation of O_3 in the presence of UV light, H_2O, O_2 and SO_2 [10] (Section 3.4.3). The latter method provides a constant level of H_2SO_4, without significant concentration and temperature gradients or losses caused by dilution. However, during these experiments major challenges arise. The chamber needs to be homogeneously illuminated by UV light which has a spectral profile representative for the atmosphere – while having no significant thermal effect on the chamber.

Temperature is one of the most crucial factors influencing both chemical mechanisms and the phase-partitioning thermodynamics [45]. These effects have received little attention so far [56, 57, 103, 104, 120], however, Duplissy et al. [27] reported that temperature enhancements caused by heat loads (at a rate of 0.1 °C per 10 min) from the UV system resulted in spurious nucleation events which were attributed to H_2SO_4 evaporating from the chamber walls.
During most photochemical studies UV systems consist of UV lamps with various light intensities and spectral profiles (UV-A (320 – 400 nm), UV-B (290 – 320 nm), UV-C (100 – 290 nm)) [113]. Commonly used lamps include xenon arc lamps with spectral filters [15, 16, 105] providing a representative spectrum for the atmosphere (300 – 800 nm), or UV-A and blacklights, which do not emit wavelengths above 400 nm [45]. Combinations of lamps could therefore provide the spectral distribution of interest [8, 28]. However, the temperature increase induced by the irradiation remains unaddressed.
Although various approaches exist which are aiming for a reduced heat load exerted

on the experimental chambers, none of them seems to be fully successful. Both blacklights combined with circulating fans at the FEP Teflon film Caltech smog chamber [21] and indirect illumination as used at the PSI smog chamber [105] show temperature variations of less than 1 °C. Other approaches to optimize UV systems can be found in Hallquist et al. [45] and Dodge [26].
A novel fibre-optic UV illumination system has been developed which provides a successful solution to transmit only a negligible heat load by the UV lamps (see Section 3.4.1). A similar thermal stability has not been achieved in other comparable experimental set-ups so far. The new design of the irradiation system is based on the experiences gained from experiments in 2006 where thermal load was still an issue [27]. Another advantage of this set-up is that no large windows are required for illumination, and thus thermal inhomogeneities and warm spots on inner surface of the aerosol chamber are avoided.

In this paper we focus on the performance of the novel UV fibre-optic system installed for the Cosmics Leaving OUtdoor Droplets (CLOUD) experiment. H_2SO_4 concentrations were produced precisely and reproducibly by the same mechanism that occurs in the atmosphere, while the change of internal chamber temperature is less than 0.005 °C at 95 % confidence level (CL) when the UV light is set to full intensity. In the present paper, we demonstrate the successful application of the novel fibre-optic UV system and provide an overview of its design.

3.2 Description of the fibre-optic UV system

The primary purpose of the fibre-optic UV system is the formation of H_2SO_4 through the in situ production of OH radicals. As the overall experimental set-up will be the subject of forthcoming papers only a short description relevant for the purpose of the UV system is given here.
The fibre-optic UV system considered is installed in a 3 m-diameter electropolished stainless-steel cylinder (26.1 m^3) [20] with a continuous gas flow (86 l min^{-1}) to the chamber. An array of fibre-optic feedthroughs on the top plate of the chamber provides adjustable UV light intensities to stimulate photolytic reactions. The temperature is controlled by air circulating in the space between the chamber and the thermal housing. Experimental runs can be performed at stable temperatures (0.05 °C) between +40 and -30 °C. Ultra-pure air is obtained from mixing evapo-

rated cryogenic liquid N_2 and O_2 at a ratio of 79:21. The air is humidified with a Nafion humidifier system, while deionized ultra- pure water is provided by a Millipore Super-Q system. Ozone is produced by irradiating a portion of the inflowing air with UV light. Trace gases, like SO_2 (Carbagas, 99.95 %) are added from gas cylinders. Two internal fans (one installed at the top and one at the bottom plate of the chamber, respectively) ensure homogenous mixing.
The fibre-optic UV illumination system consists of four Hamamatsu LightningCure LC8 (L9566-02) UV light sources (Figure 3.1). Each one is equipped with a 200 W Mercury - Xenon Lamp (L8252) and provides light with a spectrum in the range between 240 and 750 nm. The useful range for O_3 photolysis is between 250 and 317 nm. The aperture (which consists of an electronically adjustable iris) defines the light output intensity and can be adjusted between 0 % and 100 %. Each of the four lamps is connected to a synthetic silica Hamamatsu light guide (A10014-50-0110, 1 m length) with a diameter of 5 mm at its output, respectively. Each light guide is connected by a coupler to a Ceramoptec fibre bundle which contains 72 quartz fibres of 0.71 mm diameter and 8 m length.

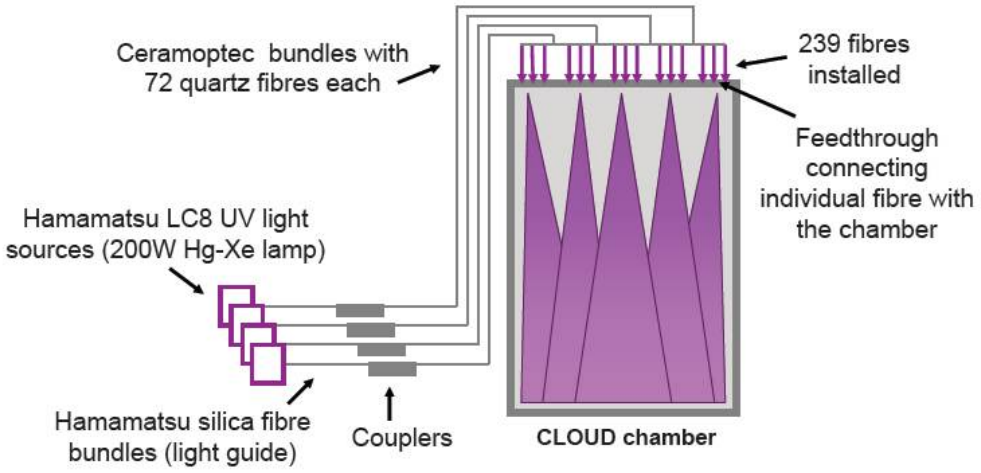

Figure 3.1: Schematic diagram of the UV fibre-optic system. Light from four UV lamps is transmitted through silica fibre bundles connected to custom designed with maximum light transmission efficiency adaptors and further to Ceramoptec quartz fibre bundles. Each bundle consists of 72 quartz fibres and 239 are currently installed on the chamber.

An optical fibre consists of a high-refractive-index core and a low refractive-index

cladding (UV600/600/P710/830 T, Ceramoptec), and can transmit light to distances far away from the light source with only little attenuation (5 %). From the total of 288 fibres, 239 are in place at the top of the chamber currently (this will be changed to 255 fibres in 2011). The UV light is introduced into the chamber through 239 custom made optical fibre vacuum feedthroughs (Figure 3.2) installed in a ring structure on the top plate to allow homogenous illumination (Figure 3.2). A UV sensor installed on the chamber bottom plate monitors the light intensity continuously.

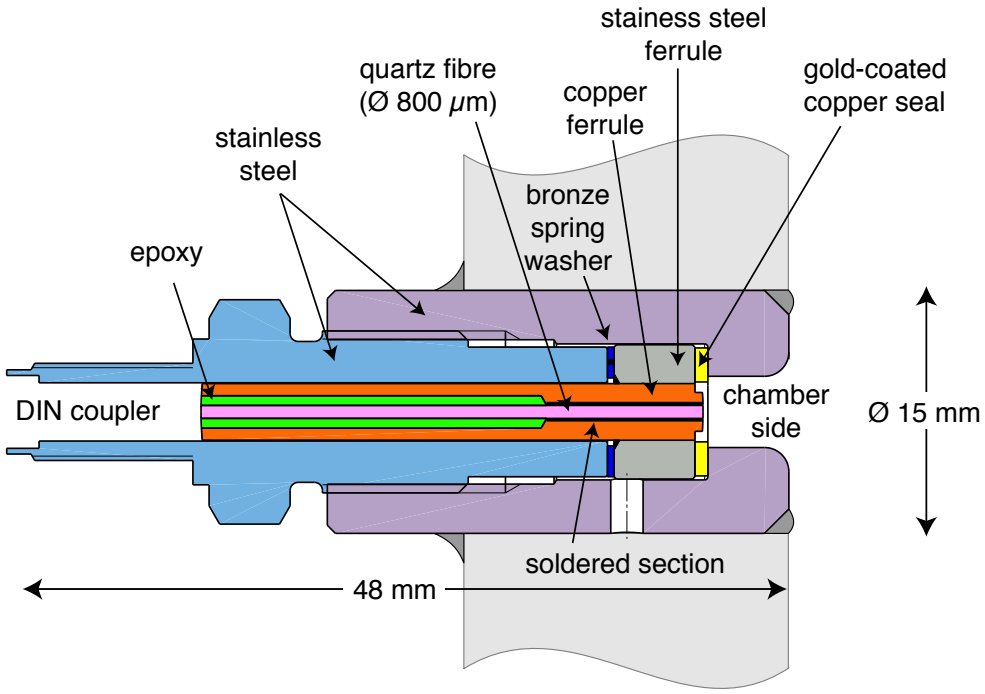

Figure 3.2: Design of the UV feedthrough. Feedthroughs are designed in a way that only gold-coated or stainless steel parts are in contact with the chamber air in order to avoid potential contamination. Additionally, they are installed at angles which avoid illumination of the chamber side walls. This is achieved by directing the UV light towards the chamber centre for the feedthroughs that lie on the rings with larger radii. This orientation also provides a constant integrated downward UV light flux across any transverse slice of the chamber.

A key component of the UV system is the design of the UV feedthroughs which transmit the UV light through the top plate of the chamber. Each feedthrough is

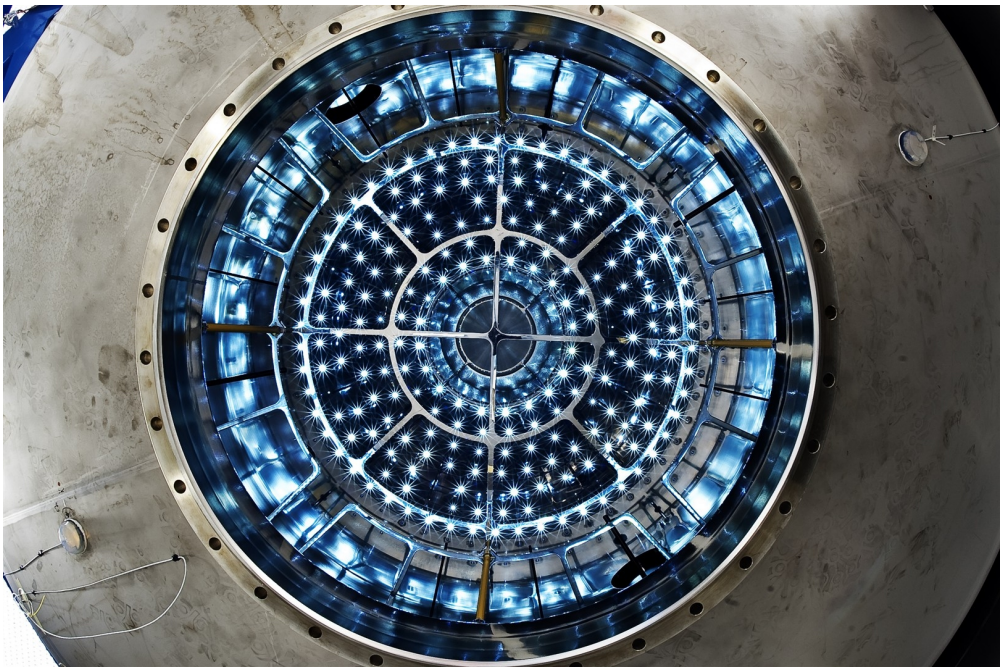

Figure 3.3: Fisheye image viewed from the bottom of the CLOUD chamber before the installation of the lower manhole cover and the thermal housing. Clearly visible is the UV illumination from the fibre-optics and the reflections on the electropolished interior as well as the fieldcage electrodes.

attached to a single optical fibre and produces a cone of light of 131 half-opening angle inside the chamber. The feedthroughs are arranged in concentric rings and are tilted with respect to the vertical central axis of the chamber in order to produce a uniform integrated column of UV light passing down the chamber.

The arrangement of the feedthroughs is optimized by model calculations with respect to the UV light distribution inside the aerosol chamber (Section 3.3.7). To find the optimal design for the most uniform illumination parameters influencing the light distribution in the chamber were varied. These parameters include the number of fibres and feedthroughs, the inclination of the feedthroughs and their position at different radii on the top plate.

The technologies used to manufacture the UV feedthroughs (Figure 3.2) are compatible with ultra high vacuum requirements. In order to avoid any contaminations interfering with experiments the use of glue or plastic materials to seal the optical

fibre is excluded. The basic requirement is to soft-solder a fibre inside a copper ferrule. To achieve this, the fibre is partly coated with a thin copper layer. The soldered length is limited in order to reduce the stress on the delicate fused quartz fibre and to improve the complete filling of the gap. Careful optimization of the soldering process is required to achieve good uniformity and absence of porosities. After soldering, the fibre is cut and polished at the ends of the copper body. Prior to these operations, the copper body is vacuum brazed into a stainless steel ring which serves as a hard surface that presses against a copper gasket when the feedthrough is installed at the CLOUD chamber. All the copper parts in contact with the chamber atmosphere are gold coated to render them chemically inert. All the installed feedthroughs are leak tested and confirmed to be vacuum tight, with leak rate below 10^{-9} mbar l s^{-1}. The feedthroughs can be operated from -196 up to 150 °C, which is suitable for chamber operating temperatures (-90 up to 100 °C).

3.3 Performance with respect to illumination characteristics

A series of laboratory and chamber measurements were undertaken to characterize the fibre optic UV system and its performance. Several parameters that may potentially affect the UV illumination during experiments, such as the transmission through the optical fibres, couplers, light guides and feedthroughs as well as the angle of the fibre lightcone were characterized. If not indicated otherwise, measurements were performed by recording the photocurrent [A] using a photodiode with an optical filter (Newport NIST calibrated model, SN 1845, with a responsivity given by the detector calibration report of 2.5 x 10^{-4} [AW^{-1}]) and a Keithley 487 Picoammeter/Voltage Source. Horizontal and vertical UV light distributions at different chamber profiles were simulated using a model (Section 3.3.7). In the following sections the results of the UV system characterization are presented.

3.3.1 Total power of the UV light source and comparison of four UV light sources

The total power of the Hamamatsu LC8 UV light source connected to a silica light guide (splitter) is given by the following equation:

$$P_{source} = \frac{I}{C} \tag{3.1}$$

where I is the measured photocurrent [568.55 $\pm$ 0.23 μA], and C the photodiode responsivity [2.5x10^{-4} AW^{-1}]. The total UV power from a single LC8 source P_{source} is therefore 2.27 W. Using Equation 3.1 and the mean photocurrent for each of the 4 silica fibres (142.14 μA), the mean UV intensity at the exit of the fibre is calculated. According to the specifications given by Hamamatsu the UV light intensity decreases with increasing distance from the exit of the fibres, while the UV light beam expands (Section 3.3.3). The UV light intensity at the exit (0 mm) of the fibres is 5685 mW cm^{-2}, while it is 3670 mW cm^{-2} at 10 mm distance. A comparison of the four light sources has been performed in the lab after the UV set-up had been upgraded from 1 to 4 light sources in 2010. The photocurrent of each light source was measured when connected to the same optical fibre. Differences of 1.3 - 1.8% were found among the three new LC8 sources indicating negligible variations. However, the output of the fourth light source which had been used in 2009 already was found to be 21 % lower although it had been equipped with a new mercury-xenon lamp. As indicated in the LC8 specifications, the intensity of UV light decreases with the lamp operating time ($\sim$ 20 % after 2500 h). However, as the lamp had been replaced, this cannot explain the difference in this case.

3.3.2 Uniformity distribution within the Ceramoptec fibre bundles. Transmission efficiency of fibres, couplers and feedthroughs

In order to analyse their uniformity fibres were chosen at various locations within the bundle. For these selected fibres the photocurrent was recorded at their output using the same method as before (Section 3.3.1). By comparing the measured photocurrents differences were found between fibres which are located in the centre and at the edges of the bundle. Therefore, one can say that light is not uniformly distributed within a bundle. Tests indicated that fibres located in the centre of the Ceramoptec bundle transmit more light (mean measured photocurrent of 1.1 $\pm$ 0.05 μA) than fibres close to the outer edge of the bundle (0.72 $\pm$0.04 μA). This indicates a difference up to 44.5 % in the light transmission depending on the location of a fibre within the bundle.
Additionally, the relative light transmission through the couplers and the 8 m long fibres was determined. The photocurrent at the output of each fibre was recorded.

The ratio of the sum of those (251.35 μA) to photocurrent at the output of light guides (586.55 μA, Section 3.3.1) defines the transmission of light of $44.8 \pm 6.7\%$. In both cases, non-optimized couplers were used during these measurements and have influenced both the light transmission through the fibres as well as the uniformity light distribution within the bundle. The design of these optical couplers was not optimal concerning the efficiency of light transmission mainly due to optical design and gap distance between the silica (light guide) and quartz fibre. In 2010 these were replaced by custom designed couplers without lenses and with an optimized gap distance allowing a more efficient UV light transmission to the chamber.
The mean UV light transmission through the feedthroughs installed on the chamber was determined by connecting the same fibre to each of the 239 feedthroughs and recording the photocurrent using a photodiode placed directly at the point where the light enters the chamber. We assumed the maximum recorded photocurrent of 0.88 μA to equal 100 % transmission, as basing on the laboratory tests the best feedthroughs have the transmission close to 100 %. The mean measured photocurrent of 0.566 μA indicates that the transmission is 64 %. This reduced transmission might be due to deposits on some of the entrance and exit fibre optic surfaces. These however have no contact with the chamber itself.
Additionally, a higher transmission was recorded for the feedthroughs which are installed at smaller angles (inner rings, 2 °C). This suggests there is a contribution from the photodiode not completely subtending the full output lightcone from the fibre.

3.3.3 Aperture vs. light profile from Hamamatsu light guide and Ceramoptec fibre

The transverse profiles of the light guide outputs were analysed using a Charge Coupled Device (CCD) video camera module (Sony XC-ST70CE) with a resolution of 752 x 582 pixels. To avoid saturation of the CCD an optical bandpass filter with 1 % transmission was used. The results indicate that the aperture determines how collimated the light that travels through the light guide and the fibres is. For instance, a narrow aperture should result in highly collimated rays of light and a sharp focus on the illuminated plane. A wide aperture should result in uncollimated light. We observed that a chosen intensity of the light source defined by aperture has an influence on the structure of the transverse profile. At low UV light intensities ($<$ 14 % aperture) the intensity profile shows a ring structure. At apertures $>$ 14-15

% the profile becomes more uniform. This might have an impact on the linearity of the aperture and intensity of the UV light which will be discussed in Section 3.4.2. These measurements were performed for the Ceramoptec quartz fibres and the same effect as for the light guide was observed.

3.3.4 UV light spectrum and intensity below 317 nm

Using a spectro-photometer (Ocean Optics miniature fibre spectrometer SD 200) the light spectrum delivered to the chamber from the optical fibres was measured. These measurements confirmed that it is in the range between 240 and 750 nm (Figure 3.4) as it is also stated in the lamp specifications. In addition, the spectrum provides a sufficiently large fraction of UV light to initialize photochemical reactions such as the photolysis of O_3 (below 317 nm).

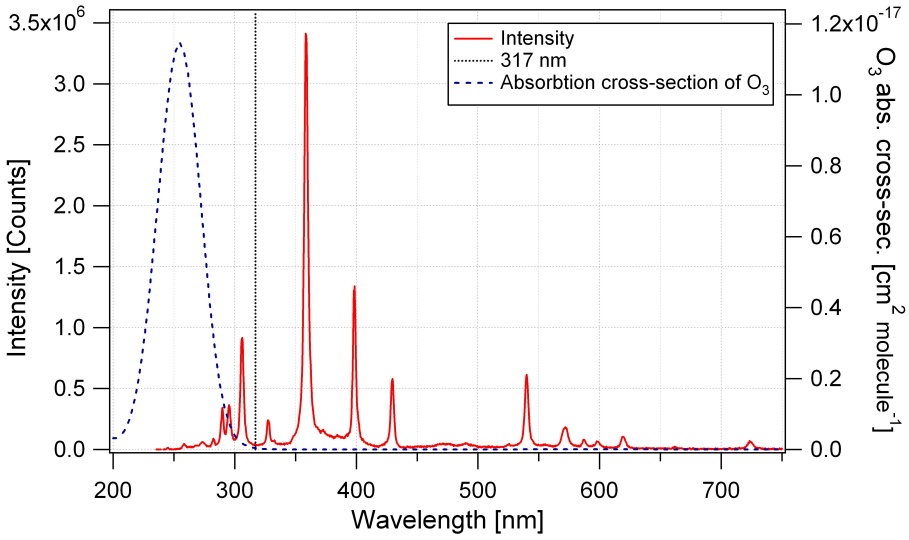

Figure 3.4: Light spectrum (red solid line) measured at the optical fibre output. The light flux in the UVB region is comparable to the ground level actinic flux. The black dotted line indicates the threshold for ozone photolysis, while the blue dashed line represents the ozone absorption cross section as a function of wavelength (maximum at 255 nm). Based on laboratory measurements (Section 3.3.5), a fraction of 31.8 % of the total UV intensity is below 317 nm.

The exact fraction of UV light below 317 nm was determined by placing a borosilicate glass filter (90 % transmission above 317 nm, 0 % transmission below 317 nm)

in front of the spectrometer and measuring the photocurrent at the light guide and a single optical fibre exit. The transmission of the filter was tested by analysing the light spectrum with and without the filter. The 50 % transmission of the filter was recorded at the 317 nm wavelength. The fraction of the UV power below 317 nm is given by:

$$F_{<317nm} = 1 - \left(\frac{P_{filter}}{0.9} * \frac{1}{P_{total}}\right) \tag{3.2}$$

where $F_{<317nm}$ is the fraction of UV light below 317 nm, P_{total} is the total UV power measured without the filter, P_{filter} is the UV power measured through the filter. The fraction of the UV light below 317 nm at the output of the optical fibre is thereby found to be 31.8 %.

3.3.5 UV power and UV intensity <317 nm inside the CLOUD chamber

Calculated UV intensity

Based on the measured quantities presented in the previous sections, the mean UV intensity inside the chamber can be calculated. For this, the following formula is used:

$$N_{<317nm} = N_l * P_{source} F_{<317nm} * T_{fibre} * T_{feedthrough} * T_{chamber} * N_{fibres} \tag{3.3}$$

$$I_{<317nm} = \frac{P_{<317nm}}{A_{chamber}} \tag{3.4}$$

where $P_{<317nm}$ is the UV power below 317 nm, N_l is the number of light sources (1 or 4), Psource is the power from one UV light source (2.27 W), $F_{<317nm}$ is the fraction of UV light transmitted below 317 nm (31.8 %), T_{fibre}, $T_{feedthrough}$ and $T_{chamber}$ are the transmissions from the light source to the fibre output (including light guides and couplers) (44.8 %), through feedthroughs (64 %) and the chamber (85 % due to fieldcage electrodes transparency), respectively, Nfibres is the fraction of fibres installed (83.9 %), $I_{<317nm}$ is the UV intensity below 317 nm, $A_{chamber}$ is the surface area in the mid plane of the chamber (7.065 m^2). The overall calculated mean UV intensity below 317 nm for one light source (2009) was therefore 20.89 and 83.57 mWm^{-2} for the set-up including four light sources (2010) (Table 3.1).

Table 3.1: UV intensities during the different CLOUD campaigns (both direct and reflected light).

CLOUD campaign	UV power (mW)		UV intensity [mWm^{-2}]	
	Total	< 317 nm[a]	Total	< 317 nm[a]
2009 (1 lamp)	194.61	61.88	27.55	8.76
2010 Spring (4 lamps)	953.72	303.28	134.99	42.93
2010 Fall (4 lamps)	873.75	277.84	123.67	39.33
Calculation for:				
1 lamp	464.16	147.60	65.70	20.89
2 lamps	1856.60	590.40	262.80	83.57

[a]31.8 % is the fraction below 317 nm.

Measured UV intensity

The actual UV intensity inside the aerosol chamber was measured before each CLOUD campaign by inserting a tube into one of the sampling ports in the mid plane of the chamber (1.7 m below the fibres) (Figure 3.5).

The same photodiode was mounted at the tube end measured the photocurrent in 10 cm steps between the centre and the chamber wall. Both the direct (measured at 0°) and the reflected from the bottom of the chamber (at 180°) light intensities were recorded. The results are given in Table 3.1. In the centre of the chamber the UV intensity is the lowest, as no rings of fibre-feedthroughs are installed close to the centre. A difference of 8 % in the UV light intensity was observed between the 2010 Spring and Fall campaigns, which can most likely be attributed to the aging of the lamps.

Comparison of calculated and measured UV light intensity

The calculated UV light intensity <317 nm for one LC8 source of 20.89 mW m^{-2} (147.6 mW) is a factor 2.4 higher than the intensity of 8.76 mW m^{-2} (61.88 mW, Table 3.1) actually measured inside the chamber during the 2009 campaign. The origin of this discrepancy is not understood but it indicates an overall poorer transmission through the complete fibre-optic system compared with the lab measurements.

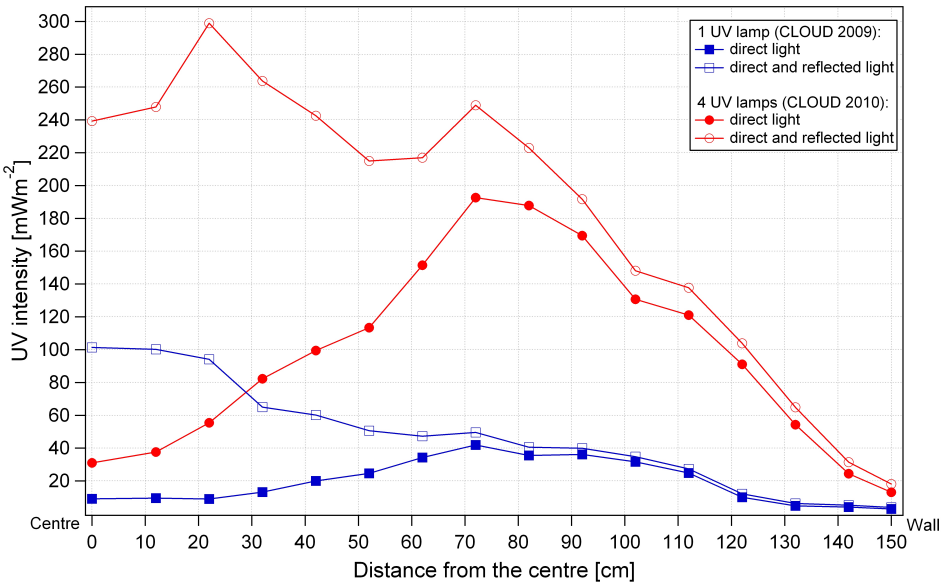

Figure 3.5: UV intensity distribution from the centre (0 cm) of the chamber to the chamber wall (150 cm) for one (2009, total UV intensity of 27.55 mW m^{-2}) and four lamps (2010 Spring, total UV intensity of 134.99 mW m^{-2}) for both direct, down going light (measured at 0°), and direct and reflected (at 180°) up going light. The light integrated over the whole cross sectional area of the chamber is constant as a function of z (height) since the down-going light column does not touch the chamber walls. The internal mixing fans further assure uniformity of the photolytic products.

3.3.6 Angular distribution of the fibre output

To allow for the simulation of the UV light distribution inside the aerosol chamber (Section 3.3.7), the half lightcone angle of a single optical fibre output illuminating the chamber was determined. Therefore, several Ceramoptec fibres were consecutively fixed on an optical bench and the diameter of the lightcone illuminating the screen was measured. This way, the half lightcone angle was found to be 13.72 ± 0.19°. Another method, where the fibres were placed in a distance of 17.5 mm from the CCD camera, was also used. This method yielded angles of 13.67 ±0.60° and confirms results obtained when using an optical bench (∼ 3.6 % difference). Whether a fibre was connected to the feedthrough or not, the angle remained the same meaning that the feedthrough design has no effect on the angle of the lightcone.

3.3.7 Reasonably uniform illumination-internal measurement vs. model prediction

Model calculations were performed to simulate the UV light distribution and to estimate the light profiles at different horizontal and vertical slices in the aerosol chamber (Figure 3.6). The model results help to understand how the density of photons is varying within the chamber volume. The model uses the geometric laws for light propagation to find the contribution from each fibre to the photon density at each part of the chamber. The simulation takes into account the half-angle lightcone of 13.72° (Section 3.3.6 and the fraction of the UV light below 317 nm (31.8 %), as well as the chamber geometry, fibre tip positions and their relative intensity. Given these parameters, one can predict the photon density inside the chamber and optimize the fibre position and angle to reduce the non-uniformities of the photon intensity. For simplicity the model does not include reflections from the chamber walls or clearing field electrodes. Because the UV illumination is not generated by a perfect plane wave, but instead by a superposition of light from many fibres which act like point sources, the density of photons is non-uniform. However the two internal mixing fans serve to mix the photolytic products rapidly throughout the chamber volume and establish uniform concentrations.

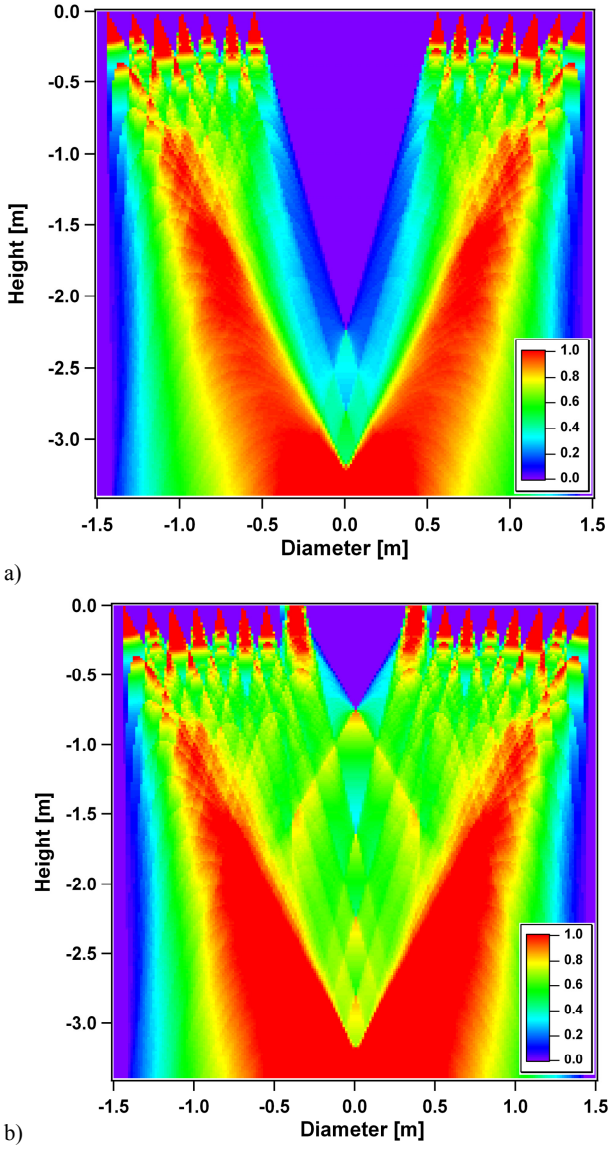

Figure 3.6: Modelled UV illumination below 317 nm inside the CLOUD chamber: **(a)** set-up with 7 feedthrough rings (239 fibres), **(b)** set-up with final 8 feedthrough rings (255 fibres to be installed in 2011) providing better illumination in the centre of the chamber.

3.4 Performance with respect to H_2SO_4 production

Having the initial experimental conditions established in the chamber - constant SO_2 and O_3 concentration, temperature (T), relative humidity (RH), and UV lamps warmed up - an equilibrium sulphuric acid concentration is typically reached within about 15 min after opening the shutter of the UV light source. Depending on the H_2SO_4 concentration produced, usually aerosol nucleation occurs at a constant rate after turning on the UV lights [95]. After switching off the UV light (closing the shutter), the OH production stops and the H_2SO_4 concentration decreases to a background level. An overview of the UV system performance is given below.

3.4.1 Negligible thermal effect

A unique feature of the UV fibre optic system described in this study is the negligible heat load it exerts on the chamber while delivering high UV power (Figure 3.7).

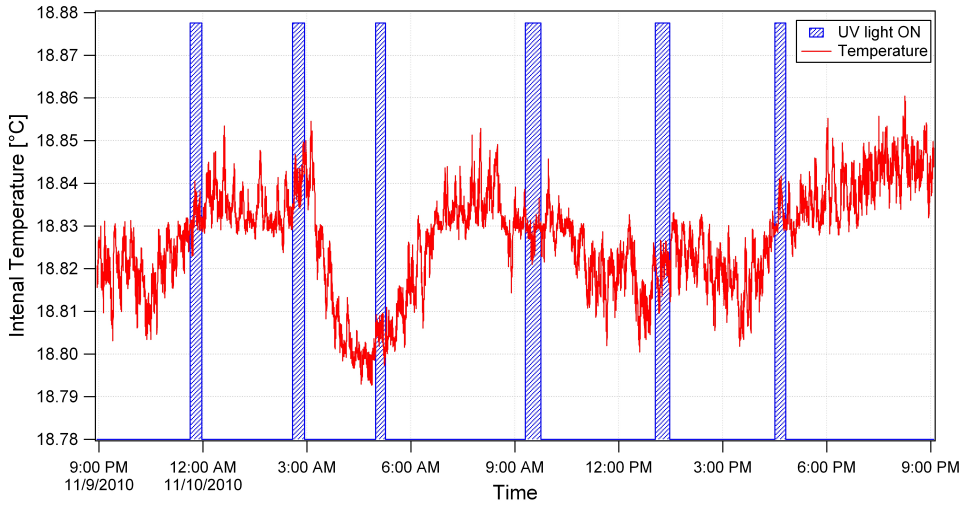

Figure 3.7: Internal temperature stability for 100 % UV intensity. Data is smoothed using Savitzky-Golay function (for 21 points, equivalent to 1 min). The UV fibre-optic system provided a total UV power of 0.873 W and 277.84 mW below 317 nm (Fall Run 2010).

On the basis of experiments where the maximum UV illumination was applied (total UV power of 0.873 W, and intensity of 123.67 mW m^{-2}), the change in chamber internal temperature was analysed and found to be less than 0.005 °C at

95 % CL within 24 h, which is better than expected 0.01 °C. The CLOUD chamber can be operated at stable temperatures (0.05 °C within 24 h at 18.8 °C) over a range between − 30 and +40 °C.

3.4.2 Control of the UV light intensity

By adjusting the aperture of the UV light source, the UV intensity can be precisely controlled, and thus the H_2SO_4 concentration inside the chamber. The dependence of the UV intensity and aperture was tested by varying the UV source aperture between 0 % and 100 % in 1 % steps while measuring the photocurrent response. Using a 3rd order polynomial fit the photocurrent can be converted into intensity [%] (Figure 3.8):

$$y = -0.28471 + 1.1534x + 0.0036461x^2 - 5.1715^{-5}x^3 \qquad (3.5)$$

where y is the UV intensity [%] for and x is the UV lamp aperture [%].

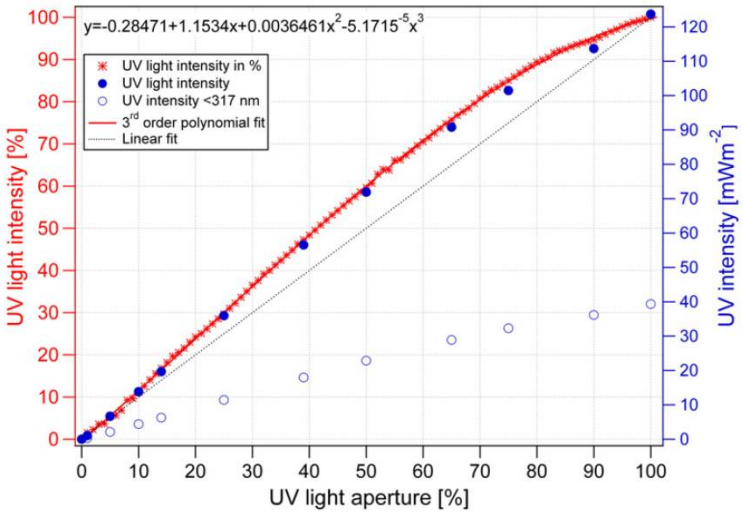

Figure 3.8: Relationship between UV aperture (%) and UV intensity (%) (red dots), where x in the fit is the aperture (%) and y is the resulted intensity (%). The total UV intensity measured inside the chamber for both direct and reflected light with a maximum value of 123.67 mW m^{-2} is presented by blue dots; UV < 317 nm (open circles) was calculated knowing that 31.8 % of total UV light is below 317 nm (Section 3.3.4). Light intensity vs. aperture is nearly linear to about 20 % and above it can be approximated by a 3rd order polynomial fit

Both total and <317 nm (31.8 % of total) UV intensity (direct and reflected) are included in the figure. The variation of the aperture is a very convenient method to produce desired H_2SO_4 concentration without having to change the O_3 concentration which requires much longer equilibration times. Although the light intensity vs. the source aperture is linear only to about 20 % (Figure 3.8, a 3rd order polynomial fit can provide a good control of the UV intensity delivered to the aerosol chamber. This non-linear dependence could be explained by different light profiles at apertures below and above 15 % (Section 3.3.3). As the profile of light becomes a filled disk at higher apertures, the intensity increases and linearity relation observed up to 20 % aperture, becomes 3rd order polynomial. For instance at an aperture of 50 % the intensity of light recorded is 60 % (Figure 3.8).

3.4.3 Precise and reproducible production of H_2SO_4

The UV fibre optic system allows the precise and reproducible production of H_2SO_4 (Figure 3.9). According to reaction 3.6 the UV light intensity can be adjusted to yield different H_2SO_4 concentrations. This is achieved by varying the UV light aperture to values between 0 % and 100 %. This way, the H_2SO_4 could be scaled to concentrations spanning about two orders of magnitude. Having constant initial parameters such as $[SO_2]$, $[O_3]$, RH and temperature established in the chamber, one can chose the UV intensity to produce a desired concentration of H_2SO_4 (Figure 3.9). For the cases discussed here, where the H_2SO_4 concentration is measured as function of the UV light aperture, the concentration of H_2SO_4 is always low enough to prevent strong nucleation events and therefore the sulphuric acid reaches a steady-state concentration (Figure 3.9). Sulphuric acid is produced in situ inside the chamber via the reaction between SO_2 and OH. The OH originates from the photolysis of O_3 to $O(^1D)$ and O_2 and the subsequent reaction with water vapour [123]:

$$O_3 + h\nu(\lambda < 317nm) \rightarrow O(^1D) + O_2(^1\Delta) \tag{3.6}$$

$$O(^1D) + H_2O \rightarrow 2OH \tag{3.7}$$

Once the OH is formed it can react to H_2SO_4 by the following reaction pathway:

$$SO_2 + OH \rightarrow HSO_3 \tag{3.8}$$

$$HSO_3 + O_2 \rightarrow SO_3 + HO_2 \tag{3.9}$$

$$SO_3 + 2H_2O \rightarrow H_2SO_4 + H_2O \tag{3.10}$$

The loss mechanisms for the sulphuric acid are deposition on the chamber wall, dilution of the gas and condensation on aerosol particles:

$$H_2SO_4 \rightarrow \text{wall loss, dilution, condensation} \tag{3.11}$$

After the production of sulphuric acid is initiated by turning on the UV light it typically takes about 15 min until a steady concentration of H_2SO_4 is reached. Then the production rate is balanced by the wall loss rate and the dilution. However, if the sulphuric acid concentration is high enough it leads to the formation of new particles and their subsequent growth, thereby increasing the available surface area for condensation. Thus, at high concentrations (strong new particle formation), the sulphuric acid gets depleted and its concentration can decrease.

The magnitude of the sulphuric acid concentration can also be adjusted by changing the ozone concentration in order to cover a large range of [H_2SO_4]. In principle, the water vapour and sulphur dioxide concentrations could be adjusted as well. However, the dependence on SO_2 is rather weak because reaction 3.8 is limited by the availability of OH. Since the experiments are always carried out at defined RH, the humidity is not used to adjust the sulphuric acid concentrations. The content of the chamber is continuously analysed by state-of-the-art instruments. Parameters relevant for the production of H_2SO_4 such as relative humidity (Dewpoint mirror, Edgtech), concentrations of SO_2 (42i-TLE, Thermo Fisher Scientific, Inc.) and O_3 (TEI 49C, Thermo Environmental Instruments) are monitored. During the CLOUD experiment sulphuric acid is measured by a Chemical Ionization Mass Spectrometer from THS Instruments (THS Instruments LLC, USA). In this instrument gaseous sulphuric acid is detected through the following proton transfer reaction [30]:

$$H_2SO_4 + NO_3^- \rightarrow HSO_4^- + HNO_3 \tag{3.12}$$

The CIMS was operated to yield one data point for the sulphuric acid concentration every 5 s and its lower detection limit was estimated to be $\sim$ 3x10^5 molecule cm^{-3} of sulphuric acid for an integration time of 20 min. The sulphuric acid CIMS measurements will be described in more detail in forthcoming papers.

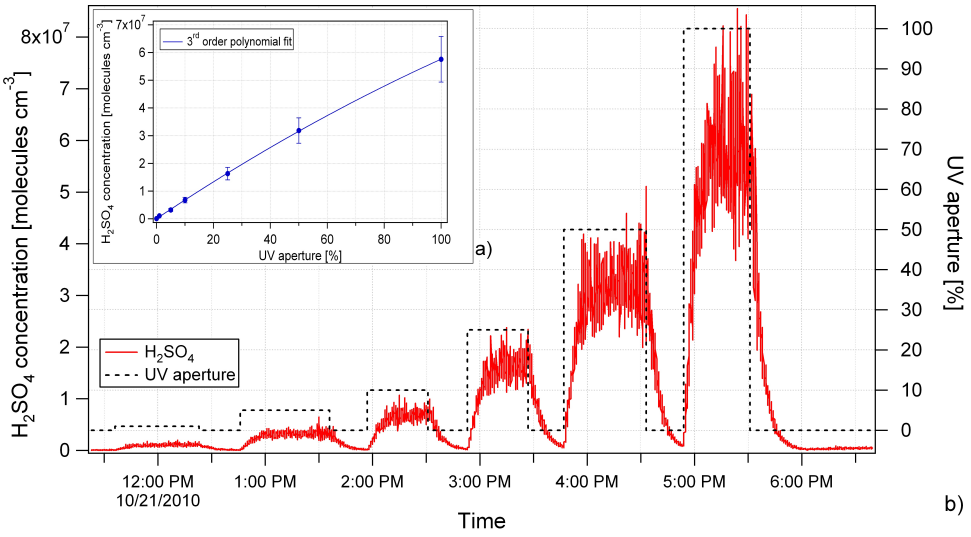

Figure 3.9: H_2SO_4 concentration vs. UV source aperture: **(a)** For aperture settings up to 20 % a linear dependence can be assumed for larger apertures the concentration of H_2SO_4 follows a 3rd order polynomial curve; **(b)** production of H_2SO_4 as a function of UV aperture. The concentration of H_2SO_4 is always low enough to prevent strong nucleation events and therefore the sulphuric acid reaches a steady-state concentration. Here the experimental conditions were set to be: SO_2 at 24 ppb, O_3 at 212 ppb, RH at 38 % and fan speed at 50 %.

3.5 Summary

It is challenging to simulate atmospheric processes realistically under laboratory conditions in aerosol chambers. One of the main issues when investigating aerosol formation and initial growth is the thermal load from UV illumination systems because nucleation is sensitively dependent on temperature and thus thermal changes can produce spurious formation of new aerosol particles. In this paper we have demonstrated that this problem can be solved by means of a fibre optic UV system. For the system installed at the CLOUD aerosol chamber at CERN it is demonstrated that the change of the internal chamber temperature at full UV intensity (100 %) is as small as 0.005 °C.

The UV fibre-optic system reported in this study is a powerful tool for nucleation experiments. It provides (1) an extremely low thermal load, while delivering high total UV power (0.873 W), additionally, (2) it provides a light spectrum in the

UVB region which is comparable to the atmospheric ground level actinic flux while having a fraction of 31.8 % in intensity below 317 nm, (3) reasonably uniform illumination inside the chamber, (4) electronic control of the UV light intensity that enables reproducible and readily-adjustable production of H_2SO_4, (5) compatibility with the chamber operation in the temperature range between -90 and +100 °C and (6) compatibility of material and components with ultra high vacuum standards (UHV). Another advantage of this set up is that (7) no large windows are required for illumination, and thus thermal inhomogeneities and warm spots on inner surface of the aerosol chamber are avoided, (8) the use of material other than stainless steel are kept at minimum to avoid contamination that could cause an impact on nucleation studies.
Moreover, in combination with other trace gases involved, the UV fibre-optic system offers the capability to generate various other photochemical reactions that take place in the atmosphere. In the future experiments (e.g. CLOUD 2011 campaign) the UV illumination system will be upgraded by one additional inner fibre feedthrough ring, which will further improve the homogeneity of the illumination. Furthermore, two additional photodiodes will be installed in the mid plane of the chamber to continuously monitor the UV intensity during experiments.

Acknowledgements

The authors would like to thank Andre Braem and Dr. Axel Metzger for their valuable inputs during both the setting-up of the UV system and the evaluation of the respective data, Maximilien Brice (CERN official photographer) for providing pictures (`http://cdsweb.cern.ch/record/1221293`) and Alain Straus for proofreading the manuscript. Additionally, we would like to thank CERN for supporting CLOUD with important technical resources, and for providing a particle beam from the CERN Proton Synchrotron. This research has received funding from the EC's Seventh Framework Programme under the grant agreement no. 215072 (Marie Curie Initial Training Network 'CLOUD-ITN'), from the German Federal Ministry of Education and Research (project no. 01LK0902A), from the Swiss National Science Foundation, from the Academy of Finland Center of Excellence Program (project no. 1118615), from the Fundac ao para a Ciencia e a Tecnologia (project no. CERN/FP/109326/2009), and from the Austrian Science Fund (project no. P 19546, L593).

CHAPTER 4

ROLE OF SULPHURIC ACID, AMMONIA AND GALACTIC COSMIC RAYS IN ATMOSPHERIC AEROSOL NUCLEATION (PAPER II)

PAPER II (PUBLISHED)

Role of sulphuric acid, ammonia and galactic cosmic rays in atmospheric aerosol nucleation

Kirkby, J., Curtius, J., Almeida, J., Dunne, E., Duplissy, J., Ehrhart, S., Franchin, A., Gagne, S., Ickes, L., Kurten, A., **Kupc, A.**, Metzger, A., Riccobono, F., Rondo, L., Schobesberger, S., Tsagkogeorgas, G.,Wimmer, D., Amorim, A., Bianchi, F., Breitenlechner, M., David, A., Dommen, J., Downard, A., Ehn, M., Flagan, R. C., Haider, S., Hansel, A., Hauser, D., Jud, W., Junninen, H., Kreissl, F., Kvashin, A., Laaksonen, A., Lehtipalo, K., Lima, J., Lovejoy, E. R., Makhmutov, V., Mathot, S., Mikkila, J., Minginette, P., Mogo, S., Nieminen, T., Onnela, A., Pereira, P., Petaja, T., Schnitzhofer, R., Seinfeld, J. H., Sipila, M., Stozhkov, Y., Stratmann, F., Tome, A., Vanhanen, J., Viisanen, Y., Vrtala, A., Wagner, P. E., Walther, H., Weingartner, E., Wex, H., Winkler, P. M., Carslaw, K. S., Worsnop, D. R., Baltensperger, U., and Kulmala, M.

(2011), *Nature*, 476, 429-433, DOI:10.1038/nature10343

Note: *Nature Letter Format*[1]

[1]For the purpose of this PhD thesis the following publication *(Nature Letter format)* has been divided into sections

ABSTRACT

Atmospheric aerosols exert an important influence on climate [54] through their effects on stratiform cloud albedo and lifetime [32] and the invigoration of convective storms [119]. Model calculations suggest that almost half of the global cloud condensation nuclei in the atmospheric boundary layer may originate from the nucleation of aerosols from trace condensable vapours [94], although the sensitivity of the number of cloud condensation nuclei to changes of nucleation rate may be small [110, 129]. Despite extensive research, fundamental questions remain about the nucleation rate of sulphuric acid particles and the mechanisms responsible, including the roles of galactic cosmic rays and other chemical species such as ammonia [172]. Here we present the first results from the CLOUD experiment at CERN. We find that atmospherically relevant ammonia mixing ratios of 100 parts per trillion by volume, or less, increase the nucleation rate of sulphuric acid particles more than 100-1,000-fold.

Time-resolved molecular measurements reveal that nucleation proceeds by a base - stabilization mechanism involving the stepwise accretion of ammonia molecules. Ions increase the nucleation rate by an additional factor of between two and more than ten at groundlevel galactic cosmic ray intensities, provided that the nucleation rate lies below the limiting ion-pair production rate. We find that ion-induced binary nucleation of H_2SO_4-H_2O can occur in the mid- troposphere but is negligible in the boundary layer. However, even with the large enhancements in rate due to ammonia and ions, atmospheric concentrations of ammonia and sulphuric acid are insufficient to account for observed boundary-layer nucleation.

4.1 Introduction

The primary vapour responsible for atmospheric nucleation is thought to be sulphuric acid. However, theory suggests that peak concentrations in the boundary layer (10^6-10^7 cm^{-3}; [66]) are usually too low for the binary nucleation of H_2SO_4-H_2O to proceed. Furthermore, after nucleation there is generally insufficient H_2SO_4 to grow the clusters to cloud condensation nucleus sizes (more than 50 nm), so organic species are primarily responsible for particle growth [12, 150]. Nucleation of sulphuric acid particles is known to be enhanced by the presence of ternary species such as ammonia [7, 22, 175] or organic compounds [170] such as amines [10, 98, 127] or oxidized organic compounds [95, 171]. Ions are also expected to enhance nucleation [6, 88, 117, 128, 137], and ion-induced nucleation has been observed n the atmosphere [29, 84]. Because the primary source of ions in the global troposphere is galactic cosmic rays (GCRs), their role in atmospheric nucleation is of considerable interest as a possible physical mechanism for climate variability caused by the Sun [68, 133].
Here we address three issues that currently limit our understanding of atmospheric nucleation and its influence on climate [172]. First, quantitative measurements of the roles of ions and ternary vapours are lacking. Second, the nucleation mechanism and the molecular composition of the critical nucleus have not been directly measured. Third, it remains an open question whether laboratory measurements are able to reproduce atmospheric observations: recent experiments have concluded that atmospheric concentrations of H_2SO_4 and H_2O without ternary vapours are sufficient [125] or insufficient [95] to explain boundary-layer nucleation rates.

We present here the first results from the CLOUD experiment at CERN (see Methods, Supplementary Information and Supplementary Figure 4.6 for experimental details). The measurements, obtained at the CERN Proton Synchrotron, represent the most rigorous laboratory evaluation yet accomplished of binary, ternary and ion-induced nucleation of sulphuric acid particles under atmospheric conditions.

4.2 Results and Discussion

The nucleation rates (J, cm^3 s^1) are measured under neutral (J_n), GCR (J_{gcr}) and charged pion beam (J_{ch}) conditions, corresponding to ion-pair concentrations

of about 0, 400 and 3,000 cm^{-3}, respectively. A typical sequence of J_n, J_{gcr} and J_{ch} measurements is shown in Supplementary Figure 4.7 and is described in the Supplementary Information. Both J_{gcr} and J_{ch} comprise the sum of ion-induced and neutral nucleation rates, whereas J_n measures the neutral rate alone. The nucleation rates are shown in Figure 4.1 as a function of $[H_2SO_4]$ at 248, 278 and 292 K. As the temperature is reduced, lower H_2SO_4 concentrations are sufficient to maintain the same nucleation rates, as a result of the decrease in the H_2SO_4 saturation vapour pressure. Apart from contaminants (see below), the only condensable vapours present in the chamber for these data are H_2SO_4 and H_2O. The experimental results are slightly higher than model calculations [63] based on thermochemical data for charged H_2SO_4-H_2O clusters [88] under J_{ch} ionization conditions, but they show similar curvature and slope.

The presence of ions from ground-level GCR ionization (J_{gcr} curves) enhances the neutral nucleation rate roughly twofold at 292 K and more than tenfold at 278 and 248 K. The enhancement factor is up to five times larger at the higher ion-pair concentrations typical of the upper troposphere (Figure 4.2 and J_{ch} curves in Figure 4.1). Overall, we find that the nucleation rate varies with negative ion concentration, $[ion^-]$, as:

$$J = J_n + k\,[ion^-]^p \tag{4.1}$$

where p=0.7-1.0 (Figure 4.2).

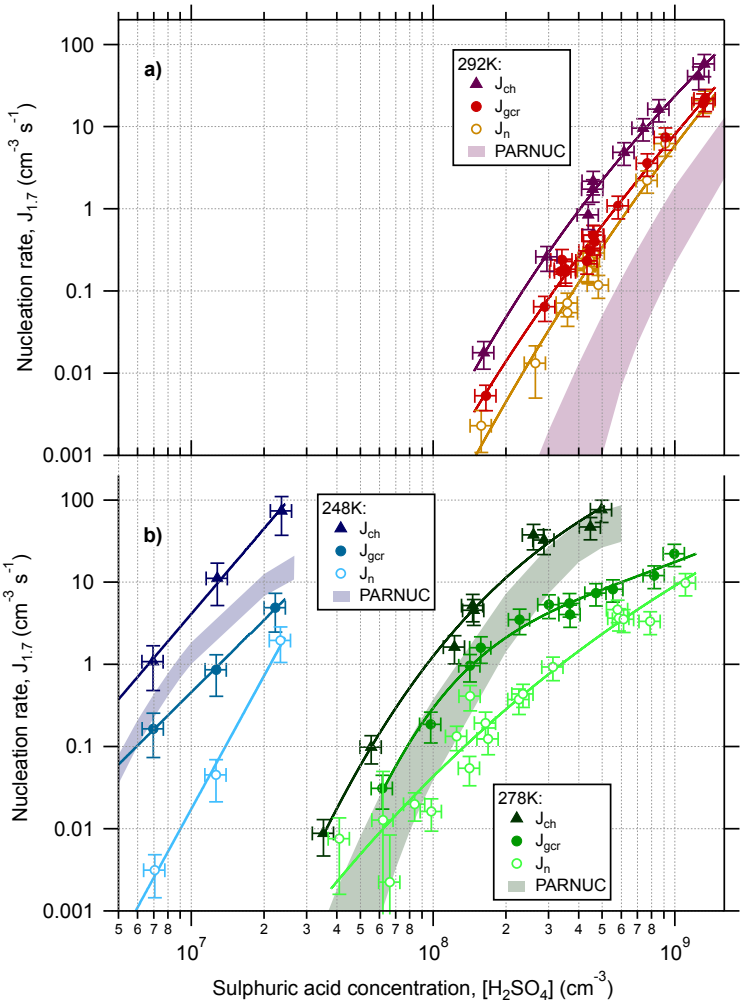

Figure 4.1: Plots of nucleation rate against H_2SO_4 concentration. Neutral, GCR and charged (pion beam) nucleation rates are shown at 1.7 nm diameter, $J_{1.7}$, as a function of sulphuric acid concentration at 38 % relative humidity. **a**, Rates at 292 K; **b**, rates at 248 K (blue) and 278 K (green). The NH_3 mixing ratios correspond to the contaminant level ($<$ 35 p.p.t.v. at 278 and 292 K, 50 p.p.t.v. at 248 K). Triangles, J_{ch}; filled circles, J_{gcr}; open circles, J_n. The predictions of the PARNUC model [63] for binary H_2SO_4-H_2O charged nucleation, Jch, are indicated by the coloured bands. The fitted curves are drawn to guide the eye. The error bars indicate the estimated total statistical and systematic 1σ measurement uncertainties, although the overall factor 2 systematic scale uncertainty on $[H_2SO_4]$ is not shown.

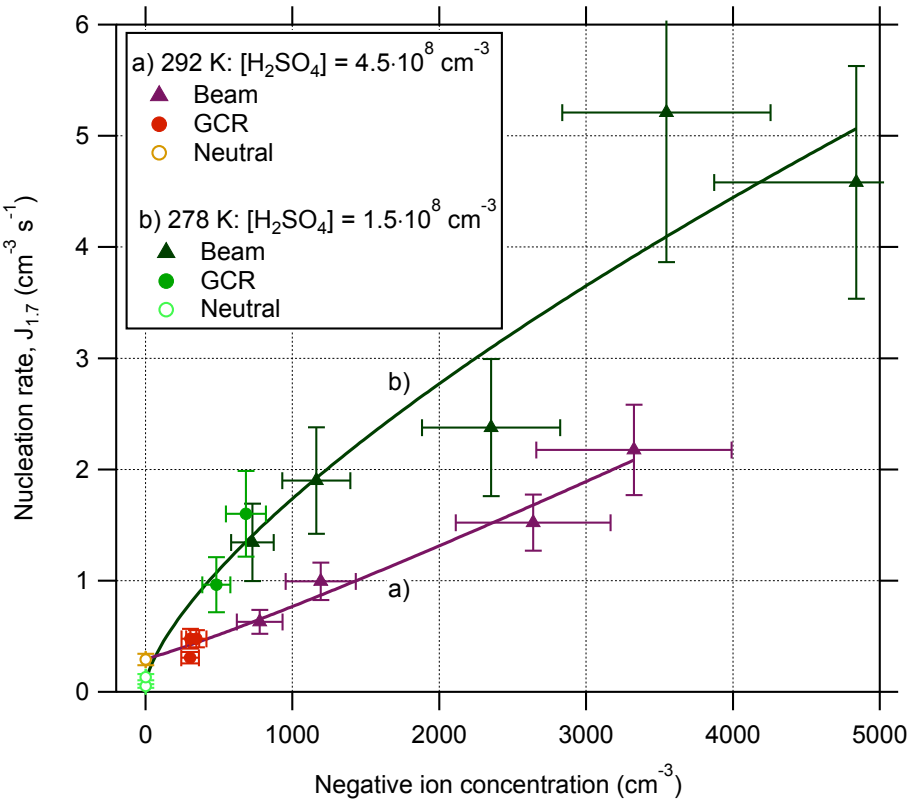

Figure 4.2: Plots of nucleation rate against negative ion concentration. Nucleation rates as a function of negative ion concentration at 292 K and $[H_2SO_4]$=4.5 × 10^8 cm^{-3} (purple line), and at 278 K and $[H_2SO_4]$=1.5 × 10^8 cm^{-3} (green line). Triangles, J_{ch}; filled circles, J_{gcr}; open circles, J_n. All measurements were made at 38 % relative humidity and 35 p.p.t.v. NH_3. Neutral nucleation rates, J_n, were effectively measured at zero ion pair concentration (ion or charged-cluster lifetime $< 1s$). The curves are fits of the form J=j_0 + k[ion^-]^p, where j_0, k and p are free parameters. The error bars indicate only the point-to-point 1σ errors; the nucleation rates and ion concentrations each have estimated overall scale uncertainties of ± 30 %

Our measurements show evidence of saturation of J_{gcr} and J_{ch} by their convergence with J_n at high nucleation rates (Figure 4.1), where almost every negative ion gives rise to a new particle [117]. However, even with ion enhancement, our measurements show that binary nucleation of H_2SO_4-H_2O will proceed at extremely low rates in the atmospheric boundary layer. In contrast, in the cooler mid-troposphere and perhaps at lower altitude in some polar regions, ion-induced binary nucleation

can proceed at ambient acid concentrations [88].

CLOUD has measured the molecular composition of nucleating charged clusters from monomers up to stable aerosol particles, and has time-resolved each step of their growth. Example mass spectra are shown in Supplementary Figure 4.8. The ion-induced nucleation measurements in Figure 4.1 exclusively involve negative clusters, containing the HSO_4^-, HSO_5^- or SO_5^- ion (Supplementary Figure 4.9 shows an example of a nucleation event). However, at higher ammonia concentrations (see below) we have also observed positively charged nucleation, involving the NH_4^+ ion.

The chemical composition of nucleating clusters containing up to $n = 20$ sulphuric acid molecules, including the HSO_4^- ion, is shown in 4.3. At 292 K the clusters above $n = 4$ are found always to be accompanied by additional nitrogen-containing molecules, comprising NH_3, amines (mainly dimethylamine and ethylamine) and urea (Figure 4.3c,d). Although these ternary vapours were not intentionally added to the chamber-at least initially-they are crucial to the nucleation. The measured contaminant mixing ratios of ammonia and total amines were less than 35 parts per trillion by volume (p.p.t.v.) and less than 50 p.p.t.v., respectively. It is notable that the nucleating H_2SO_4 clusters included only nitrogen-containing bases, even though a broad spectrum of gas- phase contaminants was identified in the chamber. A clear progression is observed from almost pure binary nucleation at 248 K to pure ternary nucleation at 292 K; both binary and ternary nucleation contributed at 278 K. From the molecular measurements, the binary fraction (or upper limit) can be determined for each J_{ch} measurement. After application of these corrections, there is excellent agreement between the experimental binary J_{ch} values and the model predictions shown in Figure 4.1.

Further measurements were made with NH_3 intentionally added to the chamber. The nucleation rates were highly sensitive to small additions of ammonia up to about 100 p.p.t.v., with evidence of saturation at higher mixing ratios (Figure 4.4). In some cases the saturation also resulted from the ionization rate limits of about 4 cm^{-3} s^{-1} for GCRs and 80 cm^{-3} s^{-1} for the pion beam. The onset of positively charged nucleation was observed at about 900 p.p.t.v. NH_3 at 292 K and at 300 p.p.t.v. NH_3 at 278 K, which contributed to a further rise of J_{gcr} and J_{ch}. With additional NH_3 the nucleating clusters revealed a distinctive increase in the NH_3 molecular content (compare Figure 4.3c with Figure 4.3d). These observations pro-

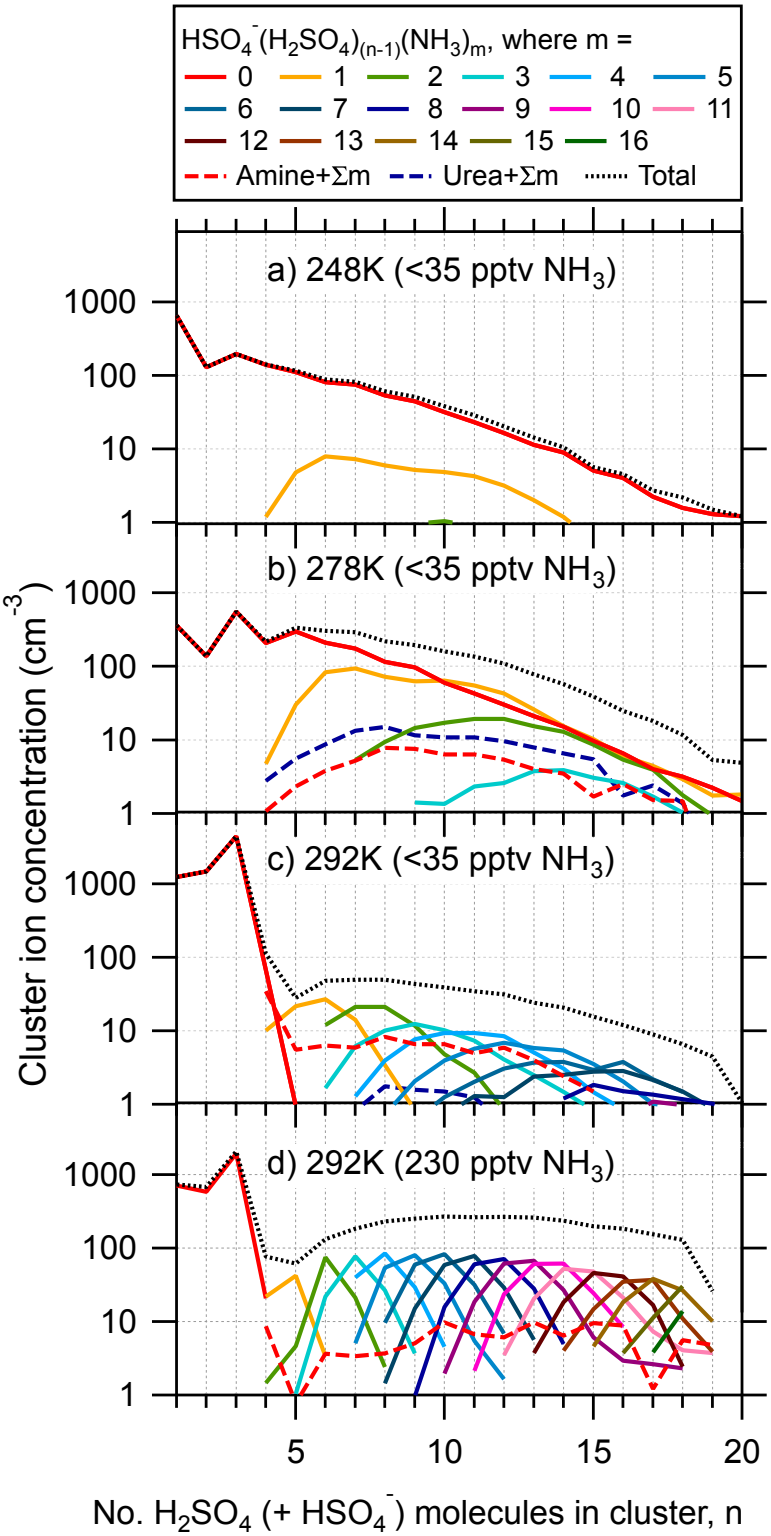

Figure 4.3: Ion cluster composition. **a-d**, The chemical composition of charged nucleating clusters at 248 K (<35 p.p.t.v. NH_3) **(a)**, 278 K (< 35 p.p.t.v. NH_3) **(b)**, 292 K (<35 p.p.t.v. NH_3) **(c)** and 292 K (230 p.p.t.v. NH_3) **(d)**. The cluster spectra are averaged over the steady-state nucleation period. To simplify the figures, only the overall envelopes are shown for organic species. The concentrations are approximately corrected for detection efficiency.

vide clear experimental evidence that the nucleation rates are strongly limited by the availability of NH_3 at mixing ratios below 100 p.p.t.v., and further strengthen our argument that binary nucleation is not significant in the global boundary layer.

The negative cluster ion spectra (Figure 4.3) show strong, quasi-stable peaks corresponding to the charged pure monomer, dimer and trimer of sulphuric acid. Here 'pure' implies only H_2SO_4 and H_2O, although we point out that no water molecules were detected because they were lost by collisional dissociation or rapid evaporation from the sulphuric acid clusters on entering the vacuum of the instrument. At 292 K, pure acid clusters with $n \geq 4$ were highly suppressed, showing that the charged pure tetramer was unstable and evaporated rapidly. The clusters grew by a striking stepwise accretion of NH_3 molecules, each stabilizing a distinct additional number of acid molecules, depending on the ammonia concentration. Figure 4.3d shows how the cluster maintained a strict 1:1 molar ratio of ammonia and sulphuric acid as it grew, suggesting that the most stable growth path involved ammonium bisulphate ($NH_4^+HSO_4^-$) cluster formation.
All clusters showed this 1:1 molar ratio above 100 p.p.t.v. ammonia-and a decreased NH_3 content below. The observed change in the nucleation rate from a strong to weak NH_3 dependence at some value below 100 p.p.t.v. (Figure 4.4) is therefore explained as a transition from NH_3-limited to NH_3-saturated nucleation (that is, where each acid molecule condensing on the cluster is immediately stabilized by an ammonia molecule, thereby suppressing its evaporation). Quantum chemical calculations indicate that NH_3 and amines bind strongly to neutral acid clusters [83], indicating that ternary nucleation of neutral clusters above $n = 1$ may proceed by the same mechanism as that observed for charged clusters above $n = 4$, after which the negative charge becomes sufficiently shielded to allow NH_3 to bind. We term this stepwise stabilization of H_2SO_4 clusters the base-stabilization nucleation mechanism.

The CLOUD measurements address a long-standing controversy in atmospheric nucleation, namely whether binary nucleation of sulphuric acid and water vapour can account for new particle formation in the boundary layer. Figure 4.5 presents a comparison of our GCR nucleation rates with atmospheric observations of boundary-layer nucleation [66, 72, 102] and recent laboratory experiments [95, 125].

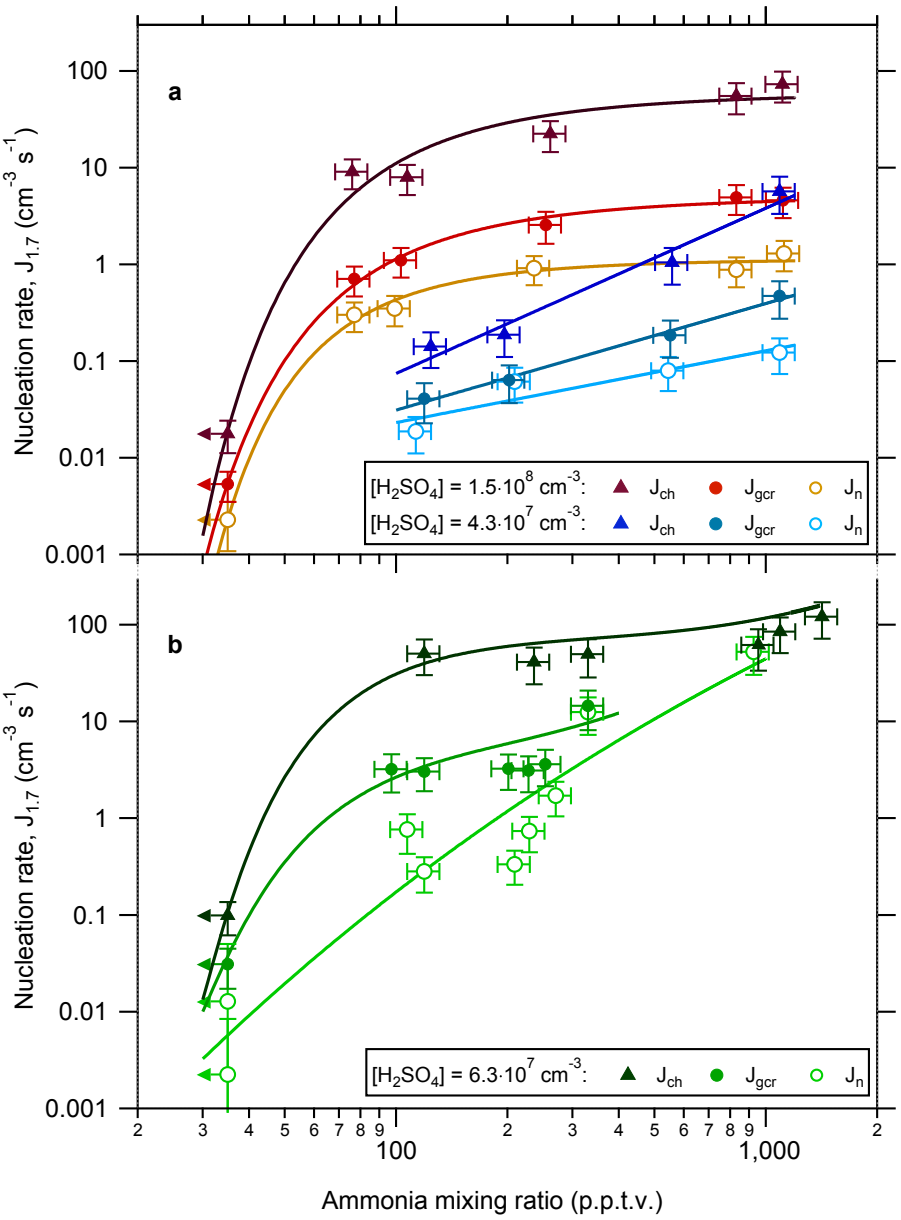

Figure 4.4: Plots of nucleation rate against NH_3 concentration. Nucleation rates are shown as a function of ammonia mixing ratio. **a**, At 292 K and [H_2SO_4]=1.5 $\times$ 10^8 cm^{-3} (curves) and 4.3 $\times$ 10^7 cm^{-3} (straight lines); **b**, at 278 K and [H_2SO_4]=6.3 $\times$ 10^7 cm^{-3}. All measurements were made at 38 % relative humidity. Triangles, J_{ch}; filled circles, J_{gcr}; open circles, J_n. The fitted lines are drawn to guide the eye. The bars indicate 1σ total errors, although the overall ammonia scale uncertainty of a factor 2 is not shown.

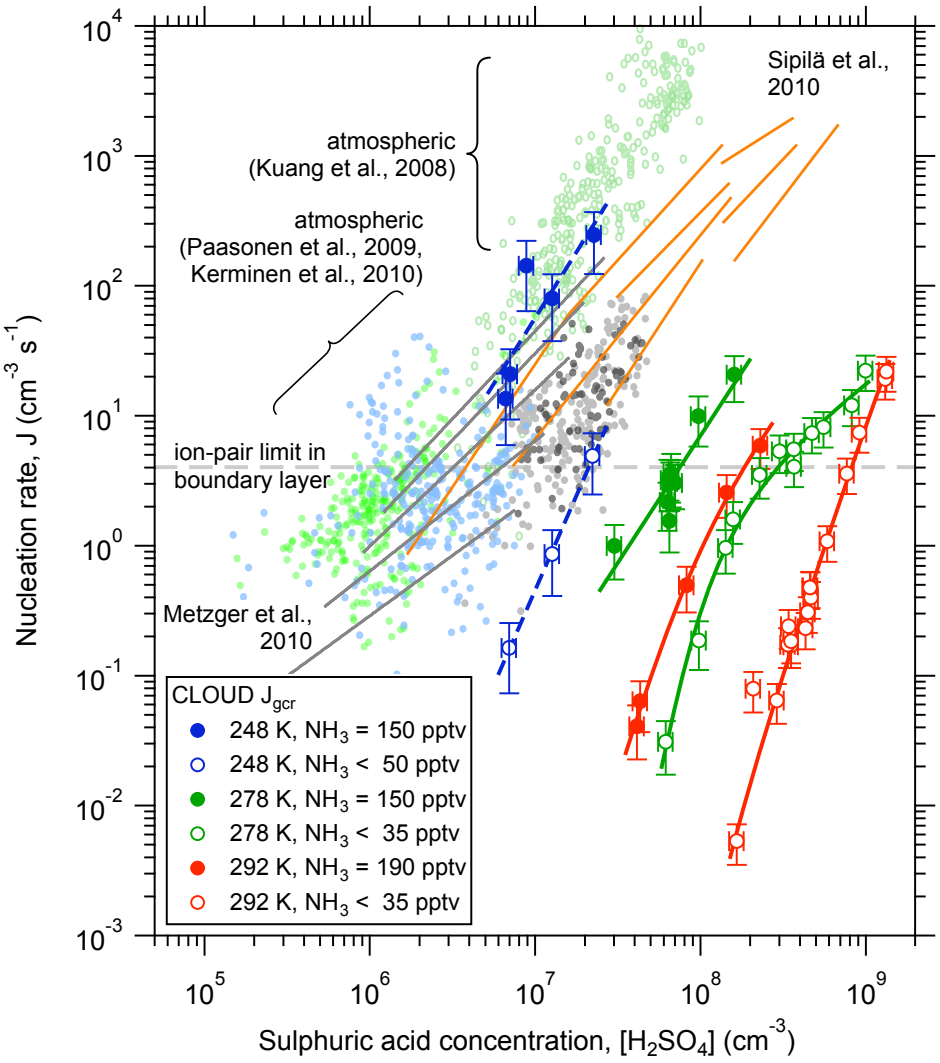

Figure 4.5: Nucleation rate comparison. Comparison of CLOUD data with measurements of the nucleation rate of new particles as a function of $[H_2SO_4]$ in the atmospheric boundary layer (pale filled circles [66, 102] and pale open circles [72]) and with recent laboratory experiments at room temperature (grey [95] and orange [125] lines). The CLOUD data (large, darker symbols and lines) show the galactic cosmic ray nucleation rates, J_{gcr}, measured at 248 K (blue), 278 K (green) and 292 K (red) and at NH_3 mixing ratios of $<$ 35 p.p.t.v. (open green and red circles), $<$ 50 p.p.t.v. (open blue circles), 150 p.p.t.v. (filled blue and green circles) and 190 p.p.t.v. (filled red circles). The bars indicate 1s total errors, although the overall factor 2 scale uncertainty on $[H_2SO_4]$ is not shown. The measurements at 278 and 292 K bracket the typical range of boundary-layer temperatures, whereas those at 248 K reflect exceptionally cold conditions. Ion-induced nucleation in the boundary layer is limited by the ion-pair production rate to a maximum of about 4 cm^{-3} s^{-1}.

We find that ion-induced binary nucleation proceeds at a significant rate in the cool temperatures of the free troposphere at atmospheric concentrations of sulphuric acid, and may be an important process when ternary vapour concentrations are low. Some fraction of these particles may be transported downwards and could constitute an important source in the remote marine boundary layer. In contrast, we show that binary nucleation within the boundary layer is negligible in all except the coldest conditions, so additional species are required. It has been reported [125] that H_2SO_4 at atmospheric concentrations can explain atmospheric nucleation rates in most locations even without the clear participation of ammonia or organic substances. In view of the CLOUD results, we consider it likely that the result in [125] was affected by the presence of ternary vapours below the detection limits of the experiment.

Under the conditions studied so far in CLOUD (no intentional addition of organic vapours), essentially all nucleating sulphuric acid clusters at 292 K include nitrogen-containing bases or amides: NH_3, amines or urea. However, for typical boundary-layer ammonia mixing ratios, below about 1 p.p.b.v., ternary nucleation of NH_3-H_2SO_4-H_2O, with or without ions, is unable to explain atmospheric observations (Figure 4.4, 4.5). This implies that other species, most probably organic compounds [95, 171], are necessary for boundary-layer nucleation.

The CLOUD experiment provides direct measurements of the molecular composition from single molecule to stable aerosol particle. This has provided new insight into how the ternary nucleation of sulphuric acid particles in the region of the critical cluster proceeds by a base-stabilization mechanism: the clusters grow by a stepwise accretion of basic molecules, each stabilizing a distinct additional number of acid molecules in the cluster, depending on the vapour concentrations. The CLOUD measurements have also quantified the enhancement of ion-induced nucleation compared with neutral nucleation.

Ground-level GCR ionization substantially increases the nucleation rate of sulphuric acid and sulphuric acid-ammonia particles, by between twofold and tenfold or more, provided that the nucleation rate lies below the limiting ion-pair production rate. Although we have not yet duplicated the concentrations or complexities of atmospheric organic vapours, we find that ion enhancement of nucleation occurs for all temperatures, humidities and cluster compositions observed so far. Ion-induced

nucleation will manifest itself as a steady production of new particles that is difficult to isolate in atmospheric observations because of other sources of variability but is nevertheless taking place and could be quite large when averaged globally over the troposphere. However, the fraction of these freshly nucleated particles that grow to sufficient sizes to seed cloud droplets, as well as the role of organic vapours in the nucleation and growth processes, remain open questions experimentally. These are important findings for the potential link between galactic cosmic rays and clouds.

4.3 Methods Summary

CLOUD is designed to study the effects of cosmic rays on aerosols, cloud droplets and ice particles, under precisely controlled laboratory conditions. The CLOUD chamber and gas system have been built to the highest technical standards of cleanliness and performance. Owing to its large volume (26 m^3) and highly stable operating conditions, the chamber allows nucleation rates to be reliably measured over a wide range from 0.001 to well above 100 $cm^{-}3$ $s^{-}1$. The loss rate of con- densable vapours onto the walls of the chamber (0.0015 $^{-1}$) is comparable to the condensation sink rate onto ambient aerosols under pristine atmospheric boundary-layer conditions. The experiment has several unique aspects, including precise control of the 'cosmic ray' beam intensity from the CERN Proton Synchrotron, the capability to create an ion-free environment with an internal electric clearing field, precise and uniform adjustment of the H_2SO_4 concentration by means of ultraviolet illumination from a fibre-optic system, and highly stable operation at any temperature between 300 and 183 K. The contents of the chamber are continuously analysed by a suite of instruments connected to sampling probes that project into the chamber.

Acknowledgements

We thank CERN for supporting CLOUD with important technical and financial resources, and for providing a particle beam from the CERN Proton Synchrotron. We also thank J.-L. Agostini, S. Atieh, J. Baechler, D. Bloess, G. Bowden, A. Braem, T. Callamand, A. Castel, L.-P. De Menezes, G. Favre, L. Ferreira, L. Gatignon, D. Gregorio, M. Guinchard, E. Ivanova, F. Josa, I. Krasin, R. Kristic, A. Kuzmin, O. Maksumov, S. Mizin, R. Richter, R. Sitals, A. Vacca, R. Veenhof, A. Wasem and M. Wilhelmsson for their contributions to the experiment. This research has received

funding from the EC Seventh Framework Programme under grant agreement no. 215072 (Marie Curie Initial Training Network, 'CLOUD-ITN') and ERC-Advanced Grant 'ATMNUCLE' no. 227463, the German Federal Ministry of Education and Research (project no. 01LK0902A), the Swiss National Science Foundation (project nos 206621-125025 and 206620-130527), the Academy of Finland Center of Excellence program (project no. 1118615), the Austrian Science Fund (FWF; project nos P19546 and L593), and the Russian Academy of Sciences and Russian Foundation for Basic Research (grant N08-02-91006-CERN).

Author Contributions

J.A. performed the nucleation rate analysis. S.S. conducted the APi-TOF analysis. J.A., F.B., M.B., A. Downard, E.D., J. Duplissy, S.E., A.F., S.G., D.H., L.I., W.J., J.K., F.K., A. Kurten, A. Kupc, K.L., V.M., A.M., T.N., F.R., L.R., R.S., S.S., Y.S., G.T. and D.W. conducted the data collection and analysis. J.A., K.S.C., J.C., E.D., S.E., L.I., E.R.L. and F.S. performed the modelling. J.K. wrote the manuscript. U.B., K.S.C., J.C., J.K., M.K., J.H.S. and D.R.W. did data interpretation and editing of the manuscript. All authors contributed to the development of the CLOUD facility and analysis instruments, and commented on the manuscript.

4.4 Methods

The CLOUD chamber (Supplementary Figure 4.6) is a 3-m-diameter electropolished stainless steel cylinder of 26.1 m^3. After tests with a pilot experiment [27], the chamber and gas supply are designed to achieve the highest standards of cleanliness and temperature stability. To stimulate photolytic reactions - in particular the oxidation of SO_2 to H_2SO_4 in the presence of O_3 and H_2O - the contents of the chamber are irradiated by ultraviolet radiation in the range 250-400 nm, introduced by means of 250 optical fibre vacuum feedthroughs installed on top of the chamber. The chamber temperature is controlled by precisely regulating the temperature of the air circulating in the space between the chamber and its surrounding thermal housing. Experiments can be performed at temperatures between 300 and 183 K. In addition, the chamber can be raised to 373 K for bakeout cleaning. The temperature stability of the chamber is about $\pm$ 0.01 K, with no observable change when the ultraviolet lights are turned on at full power. The nominal operating pressure is one atmosphere. However, rapid adiabatic expansions of up to 200 mbar can be generated to operate in a classical cloud chamber mode for the creation and growth

of droplets and ice particles.

Pure air, free of condensable vapours, is obtained from the evaporation of cryogenic liquid N_2 and liquid O_2, mixed in the ratio 79:21, respectively. The air is humidified with a Nafion humidifier using water stabilized to $\pm$ 0.01 K and purified by recirculation through a bank of Millipore Super-Q filters and irradiated with ultraviolet radiation to suppress biological activity. Ozone is added to the inlet air by ultraviolet irradiation (less than 200 nm). Trace gases such as SO_2 or NH_3 are obtained from gas cylinders containing 100 p.p.m.v. and 1 % concentrations, respectively, in pressurized N_2. Each trace gas is diluted with pure air to the required concentration before entering the chamber, and has an individual circuit, with an isolation valve at the chamber, to avoid cross-contamination or reactions with other gases outside the chamber. To suppress contamination from plastic materials, the gas piping is made from stainless steel, and all chamber seals and most gas seals are metal (gold-coated to render them chemically inert). To compensate for sampling losses, there is a continuous flow of fresh gases into the chamber of 85 l min^{-1}, resulting in a dilution lifetime of 5 h.

The chamber can be exposed to a 3.5 GeV/c secondary π^+ beam from the CERN Proton Synchrotron, spanning the galactic cosmic-ray intensity range from ground level to the stratosphere. The beam is defocused to a transverse size of about 1.5 x 1.5 m2 at the chamber. The horizontal and vertical beam profiles and rates are measured with a plastic scintillator hodoscope. An ionization-counter array, located nearby but outside the beam region, monitors the ambient flux and angular distribution of galactic cosmic rays. Two stainless steel fans are mounted inside the chamber, and coupled magnetically to flexible drives connected to motors located outside the thermal housing. The fans produce a counter-flow inside the chamber, to rapidly mix the fresh gases and the ions generated by the pion beam, and ensure good uniformity. To study neutral nucleation, the beam is turned off and an internal electric field of up to 20 kV m^{-1} is applied by means of two transparent field cage electrodes. This rapidly (in about 1 s) sweeps out the background ions produced by galactic cosmic rays. The electrodes are supported on partly conducting ceramic insulators to eliminate surface charges and stray electric fields when the high voltage is set to zero.

The contents of the chamber are continuously analysed by instruments connected

to sampling probes that project 0.5 m into the chamber. The chamber instrumentation for the results reported here comprise a chemical ionization mass spectrometer (CIMS) for H_2SO_4 concentration, an atmospheric pressure interface time-of-flight (APi-TOF) mass spectrometer for molecular composition of positive and negative ions up to 2,000 Th (thomson units; $1Th = 1Da/e$) [58], a condensation particle counter (CPC) battery at 2.5-12 nm thresholds (mobility diameters), a di-ethylene glycol CPC (DEG-CPC) at 2.0 nm threshold [53], a scanning particle size magnifier (PSM) in the threshold range 1.3-2 nm [139], a radial differential mobility analyser (rDMA) in the size range 2-10 nm [13], a scanning mobility particle sizer (SMPS) in the size range about 10-100 nm, a neutral cluster and air ion spectrometer (NAIS) [78], a small-ion counter (Gerdien counter), trace gas analysers (O_3 and SO_2), a proton transfer reaction time-of-flight (PTR-TOF) mass spectrometer for organic vapour concentrations [44], two instruments for NH_3 measurements (a long-path absorption photometer (LOPAP) and a proton transfer reaction mass spectrometer (PTR-MS) [100], and instruments to measure chamber conditions (dewpoint, ultraviolet intensity, temperature and pressure). A central data acquisition (DAQ) system controls the operating conditions of the experiment, collects and backs up the data from the instruments, provides multi-user access for monitoring the performance of the instruments and chamber, and provides real-time physics analysis using the combined data from multiple instruments.

The APi-TOF [58] measures the ion cluster mass spectra in the chamber. Chemical species are identified from their exact mass signatures and isotopic fractions. Owing to the high mass resolution ($\Delta m/m$ = 3x10^{-4}) and accuracy ($\theta m/m <$ 2x10^{-5}) of this instrument, unambiguous identification of the constituent chemical species is achieved for almost all charged clusters up to a mass/charge limit of 2,000 Th. This excludes water molecules, which are lost by collisional dissociation or rapid evaporation from the sulphuric acid clusters on entering the vacuum of the instrument. Previous measurements have established that water molecules are indeed present in these charged clusters42. In contrast, the evaporation of ammonia and amine molecules from acid clusters in the APi-TOF is thought to be small. This is supported by the sharp cluster maxima seen in Figure 4.3d

Examples of raw APi-TOF spectra during nucleation events without additional NH_3 at 292 K are shown in Supplementary Figure 4.8 The negative-ion spectrum shows strong peaks corresponding to the charged monomer, dimer and trimer of

sulphuric acid (A_n^-, $n = 1{-}3$, where A represents H_2SO_4 or the HSO_4^- ion); higher sulphuric acid clusters ($n > 3$) are predominantly accompanied by an additional species that is either NH_3, dimethylamine or ethylamine. In contrast, the positive-ion spectrum shows no evidence for any sulphuric acid molecules, but shows pure water clusters, $H_3O^+(H_2O)_n$, n$\leq$ 3 and a broad range of organic compounds, of which strong lines are usually produced by protonated pyridine ($C_5H_5N_2.H^+$), urea ($CH_4N_2O.H^+$), dimethylamine and ethylamine ($C_2H_7N.H^+$), and $C_3H_8N_2O.H^+$, which corresponds to dimethylurea or other compounds (mostly amides).

The nucleation rates are obtained from the formation rates, dNd/dt (where the subscript d refers to the detection threshold diameter of the particle counter), measured with a TSI 3776 CPC (50 % detection threshold diameter d =2.5 nm), DEG-CPC (2.0 nm) and PSM (1.7, 1.9 and 2.1 nm) [64, 79]. The nucleation rates are determined at the critical size (taken to be 1,200 Da, or about 1.7 nm mobility diameter) from measurements made with particle counters at thresholds between 2 and 2.5 nm, because the PSM was not available for the entire campaign. To determine the nucleation rates, the measured formation rates are corrected for losses between 1.7 nm and the detection size threshold. This requires experimental measurements of the wall loss rates and particle growth rates. Other losses, such as coagulation and dilution losses are also accounted for, but are negligible. The corrections are calculated with a kinetic model (AeroCLOUD) and are cross-checked analytically [64, 79]. The nucleation rates are independently verified by direct measurements with the PSM at 1.7 nm threshold, where available.

Neutral nucleation rates are measured with zero beam and with the field cage electrodes set to $\pm$ 30 kV. This completely suppresses ion-induced nucleation because, under these conditions, small ions are swept from the chamber in about 1 s. For ion-induced nucleation to produce a critical cluster that is not removed by the electric field, the primary negative ion from a traversing ionizing particle must, within 1 s, reach an H_2SO_4 molecule, which grows beyond the critical size and is then neutralized by ion-ion recombination before reaching an electrode or the chamber wall. In the presence of the electric field, the recombination lifetime alone is estimated to exceed $5x10^4$ s, so ion-induced nucleation can be completely excluded as a background to the measured neutral nucleation rates. The error on J has three components, which are added together in quadrature to provide the total error indicated in Figure 4.1: first, a statistical measure- ment error derived

from the scatter of the particle counter measurements, evaluated separately for each nucleation event; second, an estimated 50 % uncertainty on the modelled correction factor, $J_{1.7}/J_d$, where J_d is the nucleation rate at size d, obtained after correcting dN_d/dt for detection losses, and third, an estimated 30 % systematic uncertainty on J_d estimated from the run-to-run reproducibility of dN_d/dt under nominally identical chamber conditions.
When the chamber is operated below 292 K, the particle counters and certain other detectors are cooled to about 280 K to minimize cluster evaporation on entering the warm instrument from a cold chamber and sampling probe. However, we caution that the measurements presented here at low temperatures are subject to uncorrected evaporation effects due to relatively warm instruments.

The overall experimental uncertainty on [H_2SO_4] measured by the CIMS is estimated to be $-50\%/+100\%$, on the basis of three independent measurements: particle growth rate, the depletion rate of [SO_2] by photo-oxidation, and an external calibration source. However, the run-to-run relative experimental uncertainty on [H_2SO_4] is smaller, typically $\pm 10\%$. The concentrations of SO_2, O_3 are measured with calibrated instruments and are known to $\pm 10\%$. The overall uncertainty on the NH_3 mixing ratio is estimated to be $-50\%/+100\%$. Ammonia mixing ratios are measured with a PTR-MS and LOPAP. Although the former is more sensitive (5 p.p.t.v. lower detection limit compared with 35 p.p.t.v. for the LOPAP), the sampling probe of the LOPAP has a higher efficiency, resulting in a higher overall sensitivity for the LOPAP. Because liquid water is used in its sampling probe, the LOPAP only provides measurements above 273 K.

4.5 Supplementary Information

Typical measurement sequence The nucleation rates (J cm^{-3} s^{-1}) are measured under neutral (J_n), galactic cosmic ray (J_{gcr}) or charged pion beam (J_{ch}) conditions. For J_{gcr} a beam stopper blocks the pions and the chamber is irradiated by GCRs together with a small parasitic component of penetrating beam muons, whereas, for J_{ch}, the beam stopper is opened and the pion beam is normally set to a time-averaged rate of (5 - 6)$\times$ 10^4 s^{-1} . Neutral nucleation rates are measured without any beam and with the high voltage (HV) of the clearing field electrodes set to $\pm$ 30 kV. Ion-induced nucleation is therefore completely excluded as a background to

the measured neutral nucleation rates since, under these conditions, small ions are swept from the chamber in about one second. Both J_{gcr} and J_{ch} comprise the sum of ion-induced and neutral nucleation rates, whereas J_n measures the neutral rate alone.
The ion pair concentration is around 4000 cm^{-3} for J_{gcr} , representative of the boundary layer, and around 3000 cm^{-3} for J_{ch}, corresponding to high latitudes and altitudes [31, 138]. Over the continental boundary layer at mid- and low-latitudes, ionisation from radon decay exceeds that from cosmic rays [173]. Radon decay does not contribute significantly over oceans or above the boundary layer. Radon decay is also absent from the CLOUD chamber since the air is prepared from cryogenic liquid nitrogen and oxygen.

Figure 4.7 shows a typical sequence of measurements of the nucleation rates, J_n , J_{gcr} and J_{ch}. The experimental conditions are first established (gas concentrations, temperature, etc.) and the chamber largely cleared of pre- existing aerosols so that the initial loss of freshly nucleated particles is well characterised and determined by the chamber walls. High voltage is applied to the clearing field electrodes to sweep ions from the chamber. The run is started by opening the shutter of the UV system at a selected aperture (Figure 4.7a 03:45 UTC), which rapidly establishes a chosen [H_2SO_4] in the chamber by photolytic oxidation of SO_2 in the presence of O_3 and H_2O (Figure 4.7b).

Particles begin to appear in each aerosol counter after a time delay that depends on the particle growth rate and the detection size threshold (Figure 4.7c). The nucleation rates are derived from the formation rates measured in the particle counters, dN/dt (i.e. the gradients of the curves in Figure 4.7c), according to the procedure described in 4.4. When the neutral nucleation rate, J_n, has been measured, the clearing field is turned off (04:33 UTC). This allows GCRs to generate ion pairs that remain in the chamber, as shown by the appearance of small ion clusters (nH_2SO_4, $n \leq 3$) in the Atmospheric Pressure Interface Time Of Flight (APi-TOF) mass spectrometer (Figure 4.7b). Larger cluster ions appear and build up at progressively later times, reaching a steady state distribution just as the particle counters show an acceleration of the counting rate. The ions give rise to a distinct increase in the nucleation rate, J_{gcr}, due to ion-induced nucleation at ground-level GCR intensity (Figure 4.7c). In the next step, the CERN pion beam is turned on (04:58 UTC) and a further sharp increase is observed in the nucleation rate, corresponding to J_{ch}. At low NH_3 concentrations, the ion-induced nucleation exclusively involves negatively-

charged clusters (an example nucleation event is shown in Figure 4.9). Finally, the run is ended by closing the UV shutter, turning on the clearing field HV and starting to clear the chamber of aerosols in preparation for the next run (05:19 UTC).

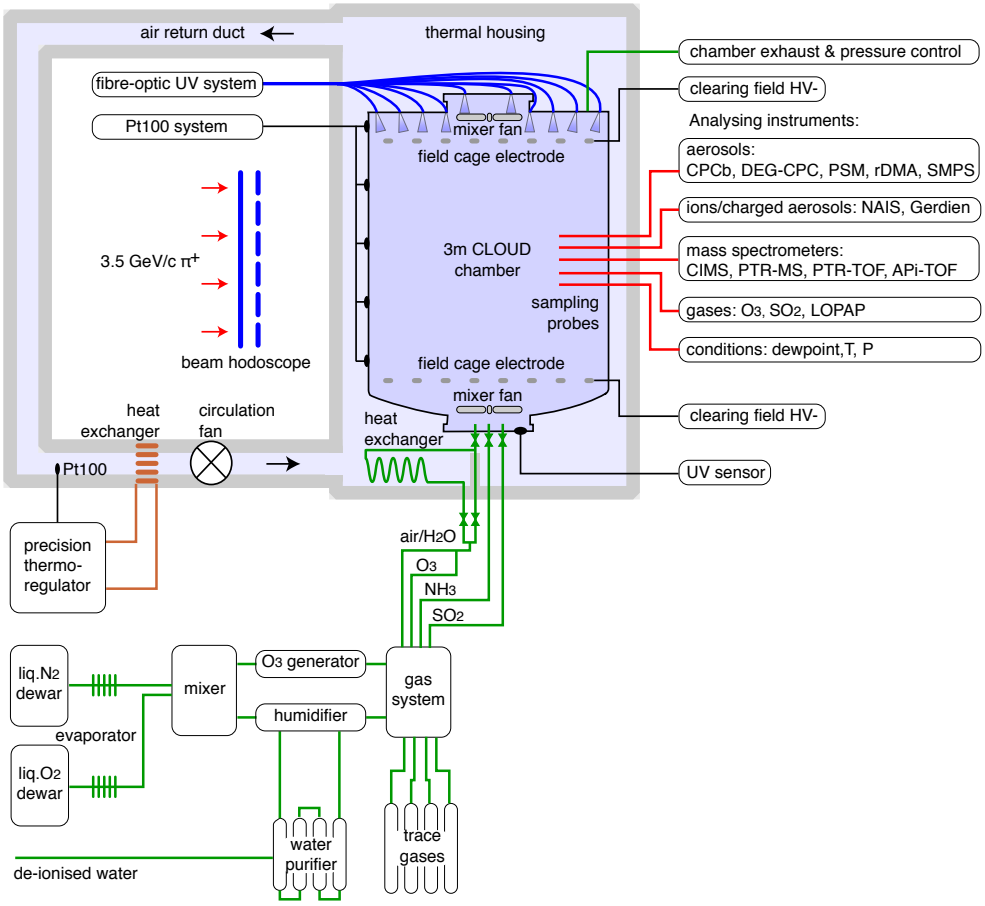

Figure 4.6: CLOUD schematic. Schematic diagram of the CLOUD experiment at the CERN Proton Synchrotron.

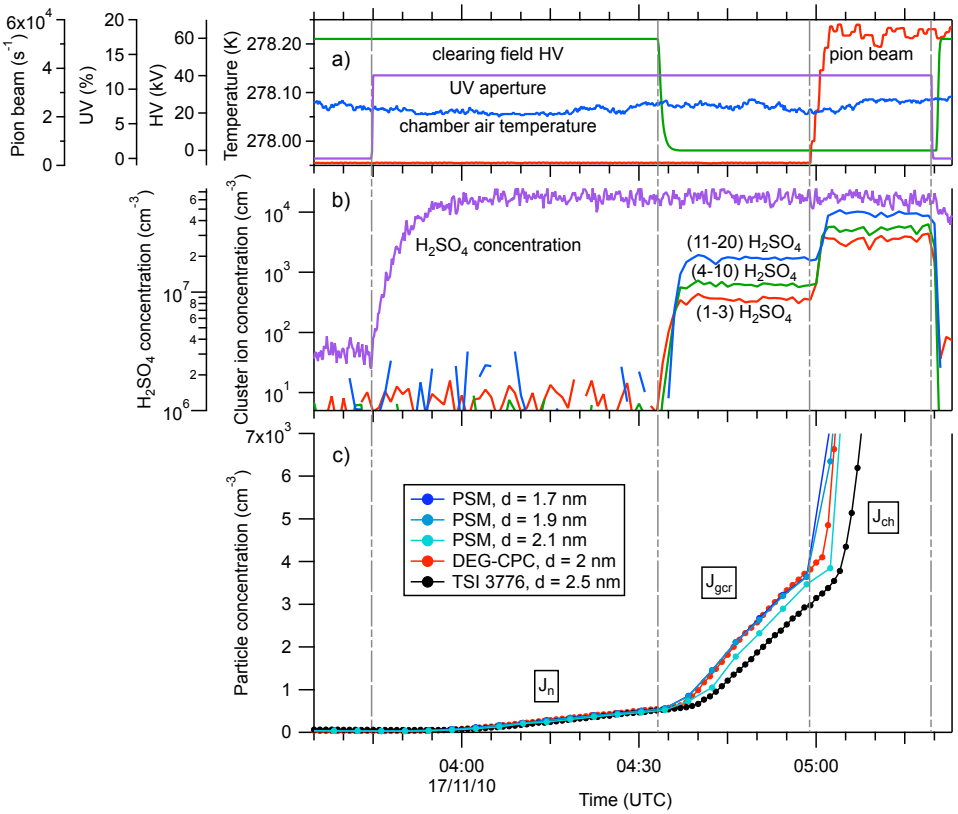

Figure 4.7: Typical measurement sequence. Example of a typical run sequence, as a function of Coordinated Universal Time (UTC), to measure a set of neutral, GCR and charged pion beam nucleation rates, J_n, J_{gcr} and J_{ch}, respectively: **a)** control parameters and chamber air temperature, **b)** [H_2SO_4] and cluster ion concentrations, and **c)** aerosol particle number concentra- tions. The run conditions are NH_3 = 200 pptv and RH = 38 %. The production of ions from GCRs and then, at higher rate, from the pion beam causes sharp increases in the cluster ion concentrations **(b)** and particle formation rates **(c)**. The onset times are progressively delayed according to the number of H_2SO_4 molecules in the cluster **(b)** or the 50 % detection size threshold, d, of the particle counter **(c)**.

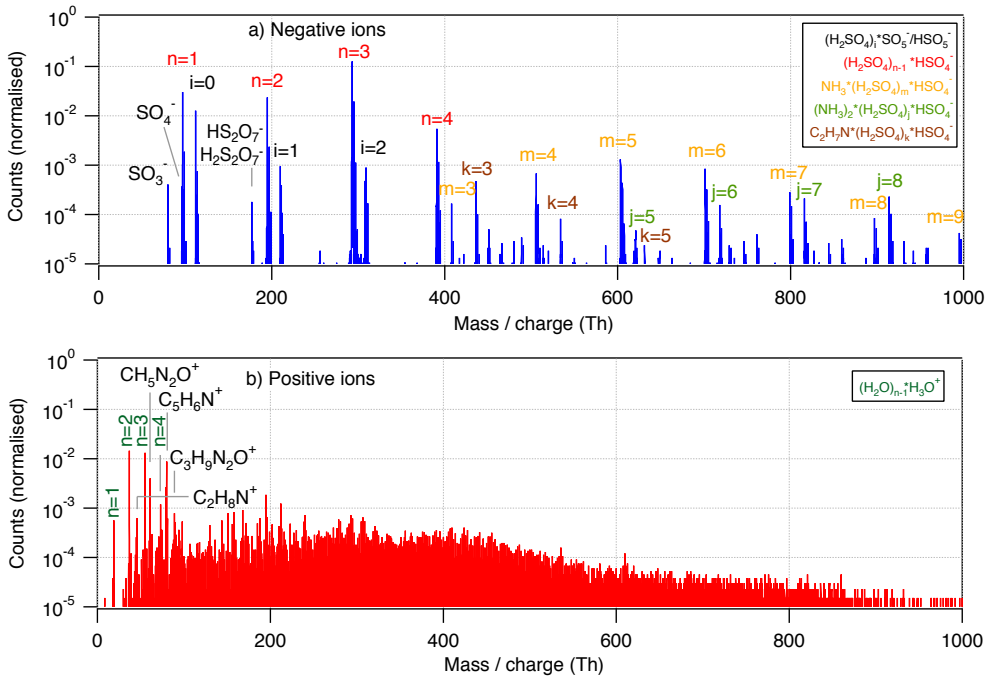

Figure 4.8: Cluster spectra examples. Examples of raw APi-TOF spectra at 292K: **a)** negative and **b)** positive ions. The run conditions are $[H_2SO_4] = 10^9$ cm^{-3} , $NH_3 = 35$ pptv, RH = 38 %, and $J_{ch} \sim 10$ cm^{-3} s^{-1}.

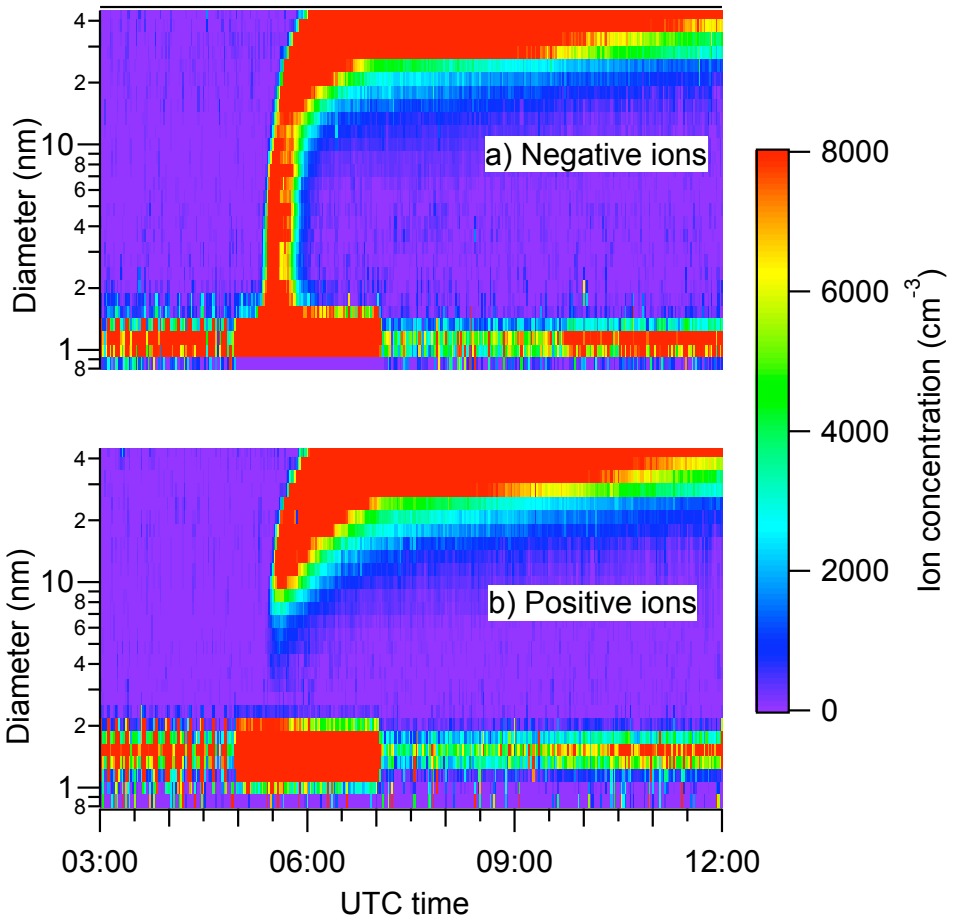

Figure 4.9: Nucleation event example. Example of a nucleation event (without additional NH_3) showing the growth versus time of **a)** negatively and **b)** positively charged particles, measured with the NAIS. The chronology is: 05h00 pion beam on, 05h15 UV on, and 07h00 pion beam and UV off (the nucleation of new particles is quenched by depletion of H_2SO_4] on the large aerosol population). Charged nucleation is observed only for negative particles; diffusion charging of both signs is observed for particles larger than about 10 nm.

CHAPTER 5

UNUSUAL TEMPERATURE DEPENDENCE OF HETEROGENEOUS NUCLEATION OF WATER VAPOR ON Ag PARTICLES (PAPER III)

PAPER III (SUBMITTED)

Unusual temperature dependence of heterogeneous nucleation of water vapor on Ag particles

Kupc, A., Winkler, P.M., Vrtala, A. and Wagner, P.E.

Manuscript in the form of an Aerosol Research Letter submitted to the Aerosol Science and Technology: 20th February 2013

Keywords: *heterogeneous nucleation, temperature dependence, SANC, condensation, water vapor*

5.1 Introduction

The initial condensational growth of pre-existing stable clusters formed through homogeneous nucleation can be described considering heterogeneous nucleation processes [151]. Quantification of heterogeneous nucleation, however, is complex. Physico-chemical properties of the seeds, such as charging state, solubility, wettability (commonly expressed in terms of contact angle), shape or size, all may affect the interactions between particle surface and the vapor molecules. According to McGraw et al. [91] seed surface properties may lead to different activation efficiencies or unusual temperature dependence. Understanding the basic mechanisms involved in heterogeneous nucleation on ultrafine particles may crucially contribute to climate research and is relevant for instrumentation development.

Recently, the effect of temperature on heterogeneous nucleation has gained some attention. In the case of well explored homogeneous nucleation [14, 34, 144, 145, 153, 164, 165] the temperature trend usually agrees with Classical Nucleation Theory (CNT). Studies explicitly investigating the temperature effect in heterogeneous nucleation have been reported by Chen et al. [17] for water nucleation, Pichelstorfer [109] for n-nonane and Schobesberger et al. [121] for n-propanol. While the first two studies found temperature trends in qualitative agreement with theory, the latter revealed unexpected inversed temperature dependence for n-propanol nucleating on sodium chloride (NaCl) particles. No such strange behavior was found for this system using silver (Ag) seeds, as was in the case of alkyl salt molecules [163].

To further investigate this behavior we performed similar heterogeneous nucleation measurements for water vapor and Ag and NaCl particles at various sizes and nucleation temperatures using the Size Analyzing Nuclei Counter (SANC) expansion chamber [147]. Water vapor has been chosen due to its relevance to atmospheric processes. It is one of the most important substances involved in atmospheric nucleation and participates in more complex interactions such as binary or ternary systems [46]. Further, in theoretical studies water has revealed to be one of the most promising fluids in condensation based techniques for aerosol detection. Its potential ability to facilitate the growth and detection of smallest particles has been pointed out by Magnusson et al. [89] and De la Mora [25].
Previous investigations involving water vapor focused on relatively large particles ($>$ 15 nm) and high nucleation temperatures (283-288 K) [17, 18]. However, to better

understand the response of condensation particle counters it is crucial to extend the size range below 15 nm in diameter and consider temperatures < 283 K as reported in this study.

5.2 Experiment description

To study the temperature effect nucleation temperatures between 263 and 288 K were chosen for monodisperse seed particles with geometric mean diameters between 3.4 and 7.4 nm. A modified version of an experimental set-up described by Wagner et al. [147] was used (Figure 5.3). At first polydisperse particles generated in a tube furnace were brought to charge equilibrium (^{241}Am bipolar charger) and sent to a Vienna-type nano-Differential Mobility Analyzer (NDMA; tapcon and analyse systeme GmbH) for size selection. Subsequently, the particles were passed through a neutralizer (^{241}Am) and an ion trap that removed any ions created in the neutralizer. For the size dependent study of heterogeneous nucleation, NaCl and Ag diameters of 3.4, 5.8 and 7.4 nm, and 3.5, 5.5, and 7 nm respectively were used. The actual classified diameters for NaCl were slightly bigger, but were corrected for particle shrinkage occurring in the presence of polar vapors [71]. Further experimental details are discussed in the Supplemental Information.

The geometric standard deviation was usually found around 1.036 for NaCl and 1.037 for Ag, while the total number concentrations of activated droplets ranged between 2.000 and 42.000 cm^{-3}. Water vapor was produced by injecting a beam of liquid water through a micro-orifice into a heating unit where it was evaporated and mixed with clean dry air. By varying the infusion rate of the liquid from a syringe pump it was possible to adjust the saturation ratio while keeping the nucleation temperature constant. A nearly saturated vapor air mixture together with monodisperse particles were passed to the temperature controlled SANC expansion chamber, where adiabatic expansion caused uniform vapor supersaturation. Saturation ratio and nucleation temperature after expansion were determined using Poisson's law. The radius and the droplet number concentration (N_a) were determined simultaneously at various times during growth using the Constant Angle Mie Scattering method (CAMS; Figure 5.4) [149]. Comparison of the experimental and theoretical droplet growth rates as a function of time after expansion (Figure 5.5) provides a confirmation of the calculated saturation ratio S as described in Winkler et al. [161]. Further details are provided in Supplemental Information. This

study focused on measuring the number of activated particles (Nact) relative to the total particle number concentration (N_{tot}) at a certain temperature (T) and vapor saturation ratio (S). The ratio of N_{act} to N_{tot} results in heterogeneous nucleation probability:

$$P = \frac{N_{act}}{N_{tot}} \tag{5.1}$$

The heterogeneous nucleation process considered can be characterized by the onset saturation ratio Sonset, i.e., the saturation ratio, at which P=0.5 and thus half of the particles are activated.

5.3 Results and Discussion

5.3.1 The effect of particle size and composition

Figure 5.1 presents heterogeneous nucleation probability vs. saturation ratio S for the nucleation of water vapor at a temperature of 278 K for both neutral NaCl and Ag seed particles of different size. Firstly, for seed particles of a certain composition it can be observed that for decreasing particle diameters increasing saturation ratios are required to activate the seed particles (Figure 5.1, 5.8; Table 5.1. This is a consequence of the Fletcher effect [35] associated with insoluble seed particles assumed to be spherical (such as Ag). The hydrophobic character of Ag seeds is represented by the contact angle (ϕ). ϕ is defined as the angle between the seed surface and the condensing liquid and characterizes particle wettability [35]. According to Fletcher the seed size and wettability influence their activation. In 2001 Petersen [107] reported the contact angles for oxidized Ag in water vapor equal to 74° (advancing) and 12° (receding). The larger the contact angle the more hydrophobic the particle is, thus a higher saturation ratio is needed for activation (Figure 5.8).

Secondly, nucleation is very sensitive to changes in particle composition and a soluble particle requires lower saturation ratio to induce the activation (Figure 5.1). For instance the Sonset is higher for insoluble 3.5 nm Ag particles (S_{onset}=2.57), than for soluble NaCl (S_{onset}=1.33) of the same size. This is a consequence of the Köhler effect [70] associated with nucleation involving soluble particles such as NaCl considered in this study. According to Köhler for each seed diameter there is a critical saturation that decreases with increasing soluble particle size as observed in

Figure 5.1, 5.8 [123]. Köhler considers two effects. On one hand the salt depresses the equilibrium vapor pressure of water above the droplet surface manifesting the Raoult effect. On the other hand the curvature of the droplet tends to increase it due to the Kelvin effect [5].
Thirdly, for both soluble NaCl and insoluble Ag particles, the slopes of heterogeneous nucleation probability curves show quite a consistent trend over the range of saturation ratios considered in this study.
The saturation ratio at which nucleation occurs can be influenced by two effects: particle size and particle physico-chemical properties (Figure 5.8). However, nucleation temperature is another crucial factor to consider (Figure 5.9).

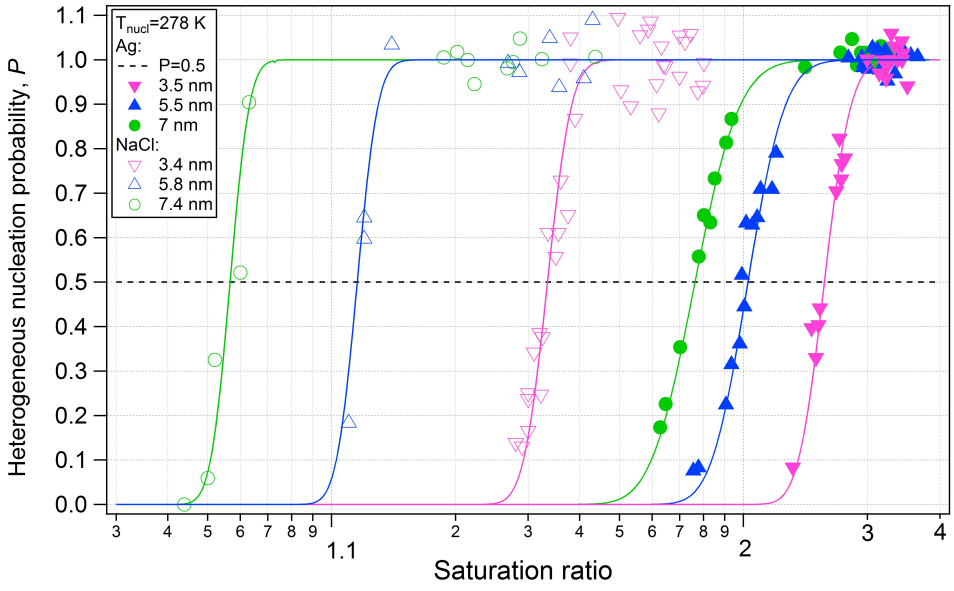

Figure 5.1: Heterogeneous nucleation probability (P) versus saturation ratio (S) for nucleation of water vapor on NaCl and Ag seeds. Results for particles with geometric mean diameters between 3.4 and 7.4 nm at 278 K nucleation temperature are presented. The solid lines are shown to guide the eye.

5.3.2 The effect of nucleation temperature

In Figure 5.2 S_{onset} of water vapor is presented as a function of temperature for both NaCl and Ag seed particles. Experimental results are compared to theoretical

predictions according to Fletcher and Köhler. Additionally, results for n-propanol vapor reported by Schobesberger et al. [121] are provided for comparison.

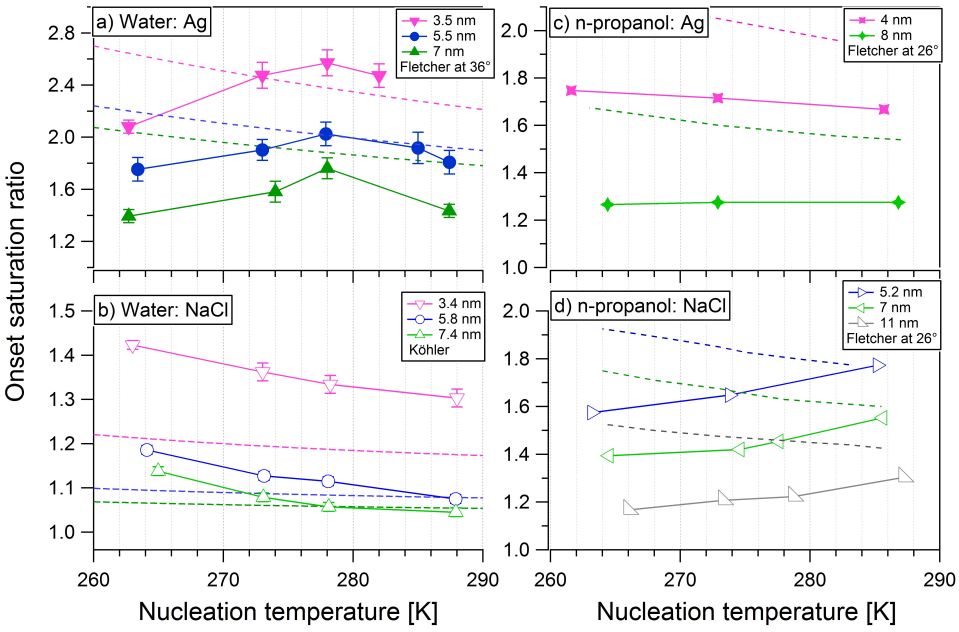

Figure 5.2: The onset saturation ratio versus nucleation temperature for Ag and NaCl particles of different diameters in water vapor: Experimental data corresponding theoretical predictions according to Fletcher (ϕ=36°; a) and Köhler (b). Additionally, data reported by Schobesberger et al. [121] for n-propanol vapor have been included for comparison (c,d). The data at 278 K are the corresponding onset values from Fig. 5.1. Error bars for saturation ratio of n-propanol vapor as well as temperature for water and n-propanol are covered by the data point symbols. Solid lines between data points have been introduced to guide the eye.

The particle activation process is generally temperature dependent and according to theory at higher temperatures both homo- and heterogeneous nucleation require lower saturation ratios (Figure 5.2, 5.9). In the temperature range considered here this trend was observed for NaCl particles where Sonset decreases with increasing nucleation temperature (Figure 5.2b, 5.10). Surprisingly, for all three Ag seed particle diameters Sonset increases with increasing temperature until it reaches a maximum at 278 K and drops again with increase in temperature (Figure 5.2a). This behavior differs from the prediction by Fletcher theory and is not yet well un-

derstood. The temperature dependencies of liquid density or surface tension do not seem to explain this behavior. Numerical computations accounting for the density anomaly of water have not reproduced this trend. As pointed out by McGraw et al. [91] an unexpected temperature dependence could be the evidence for strong surface effects that are not easily incorporated into macroscopic properties used in CNT.

Results reported here for Ag seeds are not the first case of a strange temperature trend. The experimental uncertainties are too small to explain this behavior. In 2000 Chen et al. [17] reported unexpectedly high decrease rate of onset saturation ratios for water insoluble silicon and titanium dioxide particles, while Schobesberger et al. [121] observed a reversed temperature dependence for n-propanol and NaCl particles (Figure 5.2d). For Ag particles, however, the experimentally observed trend agreed fairly well with classical nucleation theory.

5.3.3 The effect of temperature on homogeneous nucleation of water vapor

To check for any potential experimental artifacts an investigation of homogeneous nucleation of water vapor using the SANC was undertaken. Further experimental details are discussed in Supplemental Information. A comparison to the literature data indicates a satisfactory agreement (Figure 5.15). The onset saturation ratio is decreasing with increasing temperature, indicating no maximum at 278 K. This observation rules out any systematic experimental error that could explain the unexpected temperature trend for Ag seeds.

Further it seems that this anomaly is specific for the heterogeneous nucleation of water on insoluble silver particles. What is particularly surprising is the fact that these findings seem to be independent of the silver particle diameter. Clearly the physico-chemical particle properties account for this effect.

5.4 Conclusions

We have studied heterogeneous nucleation for nearly monodisperse neutral Ag and NaCl seed particles in supersaturated water vapor. While for NaCl particles the

results were in qualitative agreement with theory, an unusual temperature dependence was observed for Ag particles, where the onset saturation ratio exhibits a pronounced maximum at about 278 K. To check for possible experimental artifacts, a series of homogeneous nucleation measurements for water vapor was performed. The results were found to be in good agreement with previously published data and do not show any irregular temperature dependence indicating proper operation of the measuring system. The unusual temperature trend observed for heterogeneous nucleation of Ag in water seems to be evidence for strong surface effects, as pointed out by McGraw et al. [91]. Findings reported here could provide a helpful guidance for choosing appropriate temperature setting for the growth and detection of small particles in water-based CPCs, and possibly contribute to further advances in lowering the size threshold for particle detection. Further studies applying the second nucleation theorem [38] are planned.

Acknowledgements

This work was supported by the EC's Seventh Framework Programme under the grant agreement no. 215072 (Marie Curie Initial Training Network 'CLOUD ITN'), and by the Austrian Science Fund (project no. P 19546, L593, J3198-N21).

5.5 Supplemental Material

5.5.1 Experimental description

Figure 5.3 illustrates the experimental set up that consists of the SANC expansion chamber [147], as well as particle and vapor generation units.

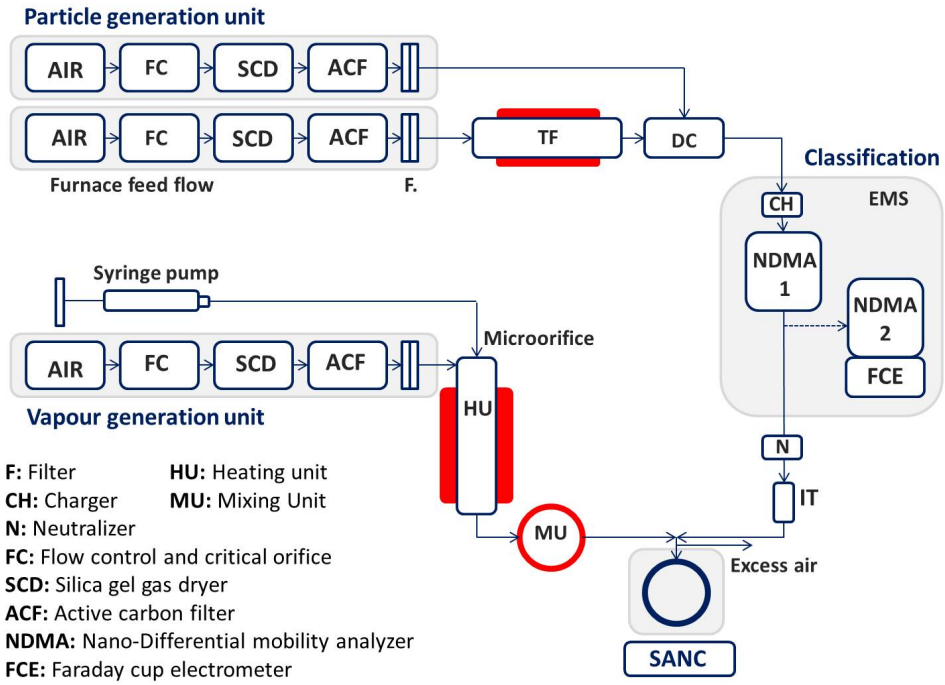

Figure 5.3: Schematic of an experimental set up includes SANC expansion chamber, aerosol and vapor generation unit

Both NaCl and oxidized Ag particles were formed by evaporation and subsequent condensation method using a tube furnace (TF) at about 1193-1333 K for oxidized Ag and 823-903 K for NaCl at a flow rate of 1.8 lmin^{-1} and 1.7 lmin^{-1} dilution respectively. Neutral particles leaving the furnace were brought to charge equilibrium in a ^{241}Am charger (CH) and then sent to the Electrical Mobility Spectrometer (EMS) consisting of two Vienna-type nano-Differential Mobility Analyzers (NDMA1 and NDMA2; tapcon and analyse systeme GmbH). NDMA1 was used for particle size classification, while NDMA2 coupled with Faraday Cup Electrometer (FCE) provided information on the size distribution of the classified aerosol. Monodisperse particles leaving NDMA1 were sent through a ^{241}Am neutralizer (N). In addition,

an ion trap (IT) was installed downstream in order to remove ions that were created in the neutralizer. The sizes of classified NaCl particles were chosen somewhat bigger than Ag particle diameters to compensate for the shrinkage effect described below in this Supplementary Information.
Water vapor added through a liquid beam was evaporated in the heating unit (HU) at 413 K and mixed with dry clean air (3-5 lmin^{-1}). Further a well-defined mixture of air and vapor together with monodispearse particles were passed to the temperature controlled expansion chamber (SANC). Vapor supersaturation was obtained by adiabatic expansion and droplet growth was observed by means of the constant-angle Mie scattering method (CAMS) [134, 149]. This provided radius and number concentration at various times during droplet growth. Further details of the experimental system are presented in Wagner et al. [147] and Winkler et al. [161]. In this study we measured heterogeneous nucleation probabilities P. The number concentration of heterogeneously nucleated droplets was measured as a function of saturation ratio. Figure 5.4 presents normalized scattered light flux vs. time (experimental) and vs. radius (theoretical).

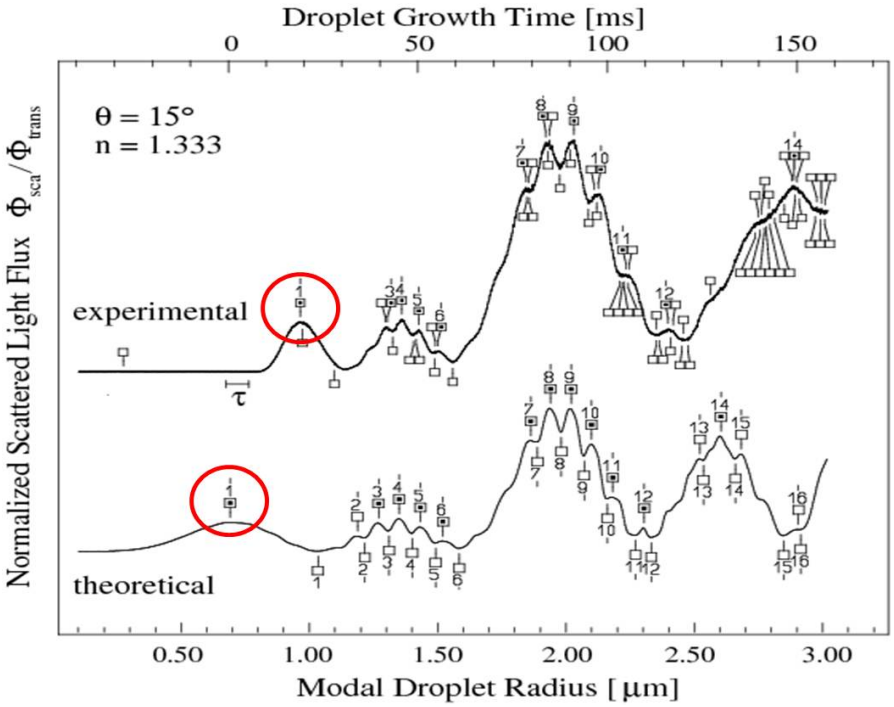

Figure 5.4: Normalized scattered light flux vs. time (experimental) and vs. radius (theoretical)

The number concentration is determined from the height of the corresponding maxima, which also yields droplet diameters at specific times. The scattered light flux with characteristic extrema is found to be in agreement with Mie theory. As the growing droplet is illuminated by a laser beam both the light flux transmitted through the (cylindrical) expansion chamber and scattered at the constant angle (15°) are recorded. By normalizing scattered to transmitted light fluxes an absolute determination of the particle number concentration is possible without the necessity to calibrate light flux sensors [149]. By establishing a correspondence between experimental and theoretical light scattering maxima and minima, size and droplet number concentration are determined at various times during droplet growth (Figure 5.5). Droplet growth measurements allow a precise verification of S as well as a corresponding error estimation.

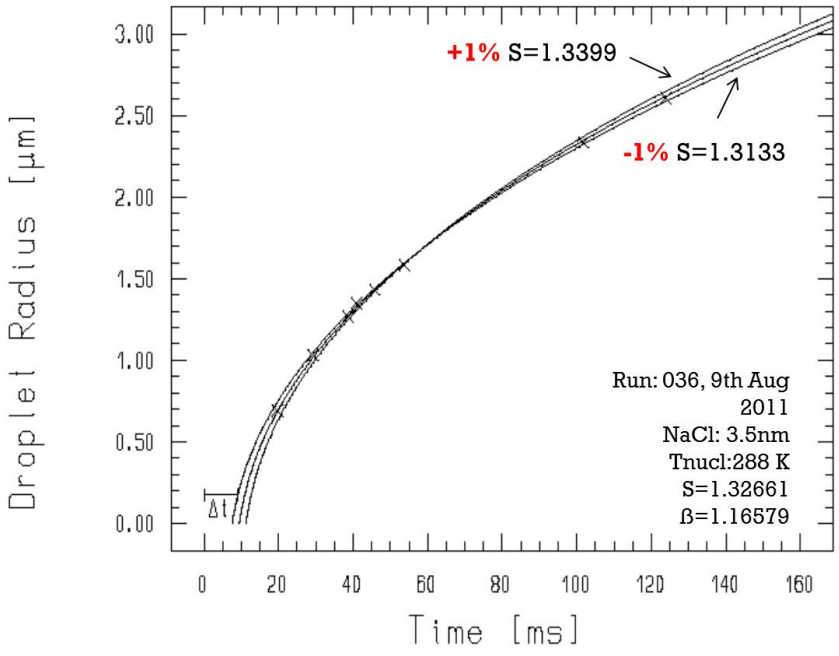

Figure 5.5: Radii of the growing water droplets measured versus time after expansion. Error estimation of saturation ratio S (± 1 %): comparison of experimental and theoretical droplet growth rates. Markers display the measured values, lines result from numerical calculations [143]

Heterogeneous nucleation takes place at sufficiently high saturation ratios (> 1). Depending on the particle diameter and particle properties too low saturation ratio will not lead to particle activation. On the other hand, when the saturation ratio

is too high (> 4) homogeneously formed water droplets will appear. Using CAMS method we are able to distinguish heterogeneous from homogeneous nucleation [161]. To assure reproducibility, experiments were repeated on a daily basis. Additionally, a diffusion tube humidifier [112] was used as an alternative to double check the validity of the results.

5.5.2 Particle shrinkage investigation (NaCl particles)

It has been reported previously that NaCl particles generated by evaporation and condensation method undergo structural change (microstructural rearrangements) in the presence of water [71, 107, 108] or n-propanol vapor [121] that results in particle diameter reduction. Additional analysis of the NaCl particles shrinkage has been undertaken for particles of 3.5, 6 and 8 nm in diameter and the experimental approach is presented in Figure 5.6.

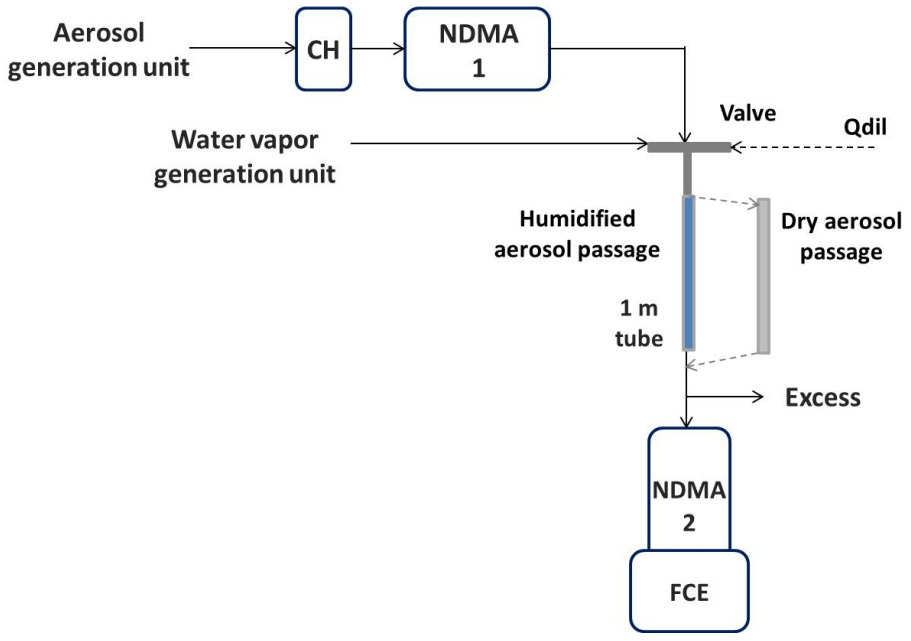

Figure 5.6: Schematic diagram of an experimental set up for NaCl shrinkage investigation

The same set up as in Petersen [107], Schobesberger [121] and Pichelstorfer [109] has been used here. NaCl particles were generated in a tube furnace by the same method as previously described for the SANC experiments. Particles were classified

in NDMA1 according to the description provided in Section 5.5.1 of this Supplemental Material. The particular RH was achieved by varying the syringe infusion rates and dilution flow (dry air; Q_{dil}) as described in Section 5.5.1. Water was injected in the heating unit and as vapor carried further to the mixing unit (MU, Figure 5.3). A valve was used to define whether dry monodisperse aerosol coming from EAC continues to flow through the dry passage or whether it mixes with humid air and flows through the passage designated for humidified aerosol. The difference in mean aerosol particle diameter caused by the water vapor was investigated for relative humidity (RH) up to 95 %. The growth factor (GF) was calculated as the ratio of the mean particle diameter of the humid to dry particle.
The results of these measurements (Figure 5.7) were compared to Petersen [107].

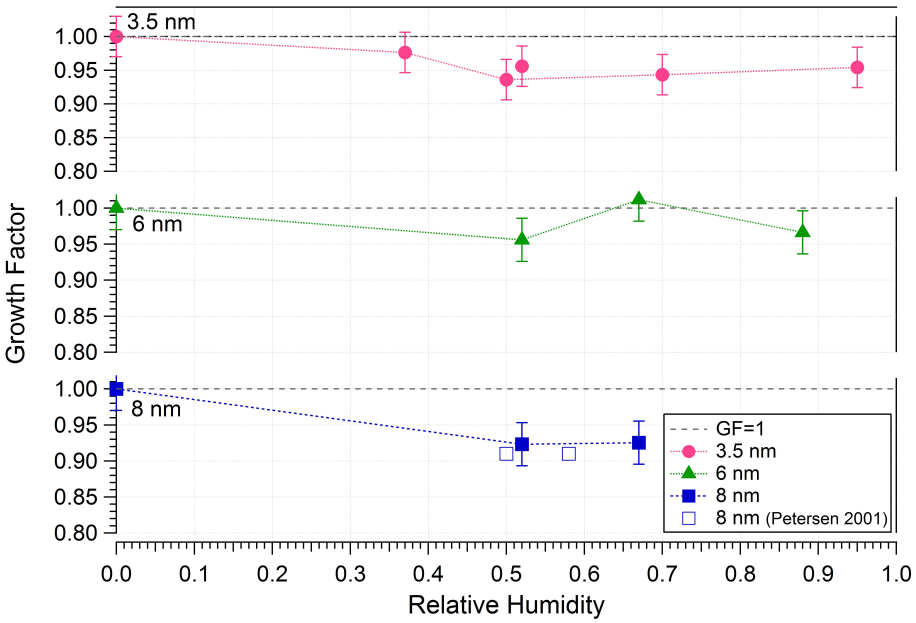

Figure 5.7: Growth factor as a function of relative humidity for NaCl particles having diameters equal to 3.5, 6 and 8 nm. Dashed lines are given to guide the eye.

It was observed that the particle shrinkage increases with increasing level of vapor saturation. When considering RH around 50 %, the GF for 3.5 nm on average was found to be 0.96, for 6 nm is 0.959 and for 8 nm equals 0.92 (0.91 in Petersen [107]). It looks like for bigger particles the GF gets smaller at fixed RH, while with increasing RH above 70 % it increases again. The resulting NaCl particle diameters

considered in this study were equal to 3.4, 5.8 and 7.4 nm in diameter.

5.5.3 The effect of seed particle size, composition and nucleation temperature

Table 5.1 presents the summary of investigations of heterogeneous nucleation of water vapor on neutral NaCl and oxidized Ag particles with various sizes and at various nucleation temperatures.

Table 5.1: Summary of the results of the temperature dependence of the activation properties of NaCl and Ag particles in water vapor. D_p is the mobility particle diameter, T is the nucleation temperature and Sonset is the onset saturation ratio at T. Dp error represents the DMA transfer function and error on Sonset is derived from the slopes of heterogeneous nucleation probability curves.

NaCl			**Ag**		
D_p [nm]	T[K]	S_{onset}	D_p [nm]	T[K]	S_{onset}
3.4 ± 0.25	263.00 ± 0.10	1.42 ± 0.01	3.42 ± 0.24	262.70 ± 0.01	2.08 ± 0.05
3.4 ± 0.25	273.02 ± 0.12	1.36 ± 0.02	3.50 ± 0.25	272.90 ± 0.10	2.48 ± 0.10
3.4 ± 0.25	278.24 ± 0.10	1.33 ± 0.02	3.44 ± 0.25	278.00 ± 0.10	2.57 ± 0.10
3.4 ± 0.25	288.00 ± 0.01	1.30 ± 0.02	3.45 ± 0.25	281.90 ± 0.13	2.47 ± 0.09
5.8 ±0.38	264.10 ± 0.11	1.19 ± 0.01	5.50 ± 0.35	263.40 ± 0.10	1.75 ± 0.09
5.7 ±0.38	273.13 ± 0.13	1.13 ± 0.01	5.51 ± 0.35	277.90 ± 0.10	2.03 ± 0.09
5.8 ±0.38	278.08 ± 0.11	1.12 ± 0.01	5.50 ± 0.35	285.10 ± 0.10	1.92 ± 0.12
5.7 ±0.38	287.89 ± 0.22	1.08 ± 0.01	5.43 ± 0.35	287.40 ± 0.10	1.81 ± 0.09
7.3 ±0.49	264.98 ± 0.09	1.14 ± 0.01	7.09 ± 0.44	262.70 ± 0.10	2.08 ± 0.05
7.4 ±0.50	273.08 ± 0.09	1.08 ± 0.01	7.09 ± 0.44	274.00 ± 0.10	2.08 ± 0.08
7.4 ±0.50	278.12 ± 0.12	1.06 ± 0.02	7.05 ± 0.44	278.00 ± 0.10	2.08 ± 0.08
7.4 ±0.50	287.91 ± 0.09	1.05 ± 0.01	7.05 ± 0.44	287.40 ± 0.10	2.08 ± 0.05

Figure 5.8 illustrates experimental onset saturation ratio as a function of seed particle size along with predictions according to Fletcher [35], Köhler [70] and Kelvin [135] theory at 278 K. Three different contact angles for Fletcher curves were applied [35, 36] (curves calculated using approach from Winkler et al. [163]). For NaCl particles Köhler theory associated with soluble seed particles is considered [70]. Further it can be observed that the effect of seed diameter increases for diameters below 10 nm as suggested by Fletcher, Kelvin and Köhler theories.
The NaCl masses used in Köhler calculations (equations provided below) correspond to the dry NaCl seed diameter considered experimentally. For each NaCl seed diameter the corresponding onset saturation ratio was determined from the height

of the maximum of the respective Köhler curve.

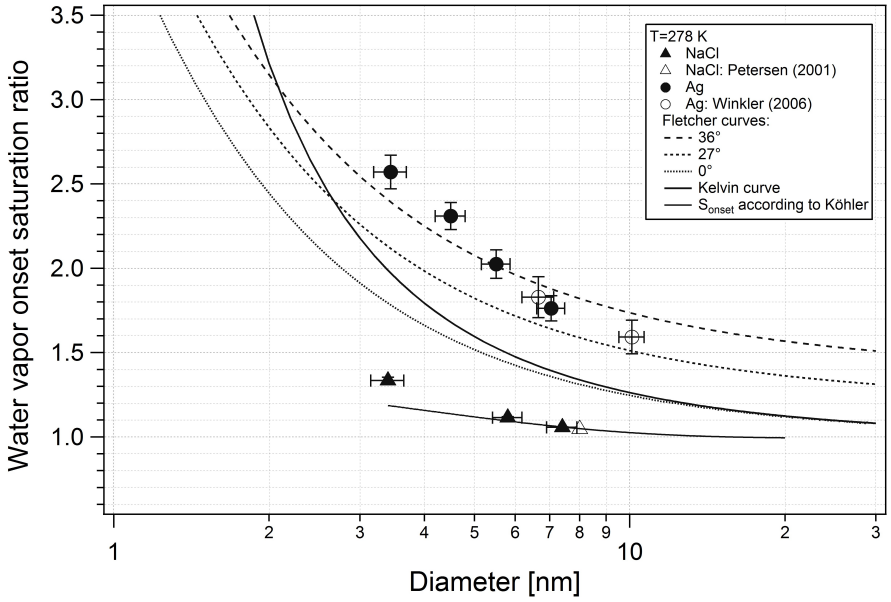

Figure 5.8: Experimental onset saturation ratio as a function of seed particle size at 278 K along with predictions according to Fletcher theory at various contact angles, Kelvin theory and Köhler theory for corresponding NaCl particle mass (for 3.4 nm m_s=4.5x10^{-23} kg; for 5.8 nm m_s=2.2x10^{-22} kg, for 7.4 nm m_s=4.6x10^{-22} kg). The uncertainty on Dp represents the DMA transfer function, while the uncertainty of the S_{onset} was retrieved from the slopes of heterogeneous nucleation probability.

The agreement of experimental S_{onset} for soluble NaCl particles with diameters $\geq$ 5.8nm is remarkable. However, for 3.4 nm NaCl seeds some deviation from the theoretical prediction is observed. This probably indicates that for the smallest NaCl particles their mass density might be somewhat below the macroscopic value. The Fletcher effect described in this study refers to the saturation ratio necessary to activate insoluble seed particles, while Kelvin effect is related to the diameter of curvature that a critical embryo has to reach to be able to grow to macroscopic droplet [135].

Fletcher curves for various contact angles (Figure 5.8) and temperatures (Figure 5.9) were calculated according to the equation described in Schobesberger et al. [121], Kelvin curves according to the equation described in Winkler et al. [161], while S_{onset} according to Köhler was obtained from Köhler curve maxima using the

equation [87]:

$$S_{v,w} = 1 + \frac{A}{a} - \frac{B}{a^3} \tag{5.2}$$

$$A = \frac{2M_w\sigma_w}{RT\rho_w} \tag{5.3}$$

$$B = \frac{3m_s\vartheta}{4\pi M_s\rho_w} \tag{5.4}$$

where a is the seed particle diameter, M_w is the molar mass of water, M_s is the molar mass of solvent, m_s is the mass of dissolved substance (e.g. sodium chloride, NaCl), σ_w is the surface tension, R is the universal gas constant, ρ_w is the density of water and ϑ is the Vant' Hoff factor. The mass of dissolved NaCl was based on particle diameter and mass density.

Figure 5.9 presents theoretical onset saturation ratio as a function of particle diameter described by Fletcher (ϕ=36° contact angle), Kelvin and Köhler theories for various nucleation temperatures. As can be seen in Figure 5.9 Fletcher, Kelvin and Köhler theories predict the same temperature trend.

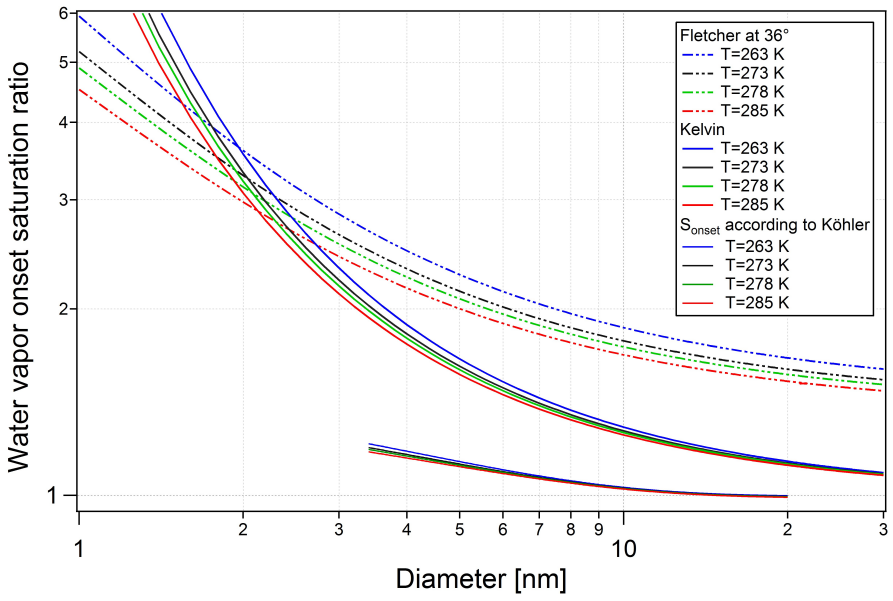

Figure 5.9: Theoretical onset saturation ratio as a function of seed particle size along with predictions according to Fletcher, Köhler and Kelvin theories

Figure 5.10 presents experimental onset saturation ratio as a function of soluble

NaCl seed particle size along with predictions according to Köhler and Kelvin theory at various temperatures. It can be seen that experimental and theoretical data are exhibiting the same temperature trend.

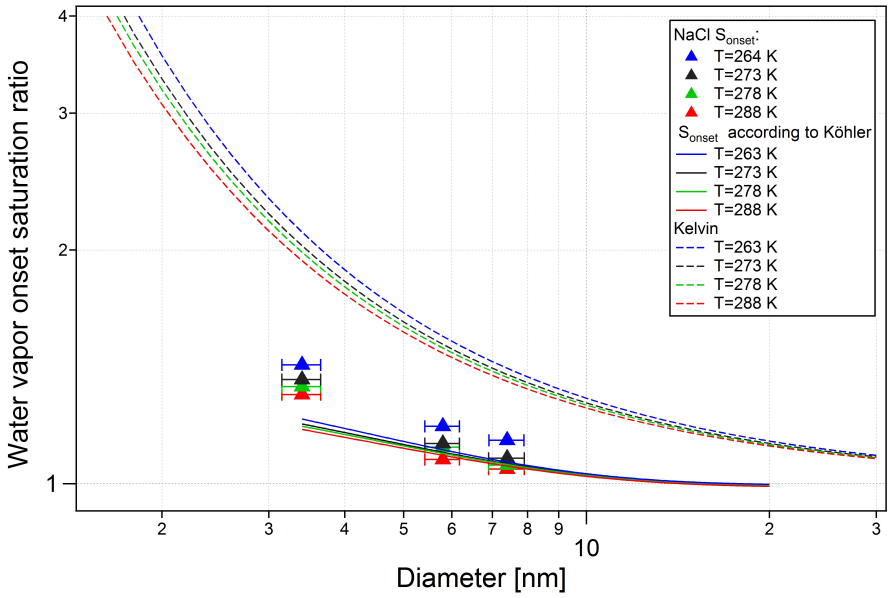

Figure 5.10: Experimental water onset saturation ratio as a function of NaCl seed particle diameter along with predictions according to Köhler and Kelvin theory at various temperatures.

Further, Figures 5.11, 5.12, 5.13, 5.14 present experimental heterogeneous nucleation probabilities as a function of water vapor saturation ratio. The size dependence of soluble NaCl and insoluble Ag particles at fixed nucleation temperature is presented in Figure 5.11 and 5.13, respectively, while the temperature dependence of NaCl and Ag seeds is provided in Figure 5.12 and 5.14.

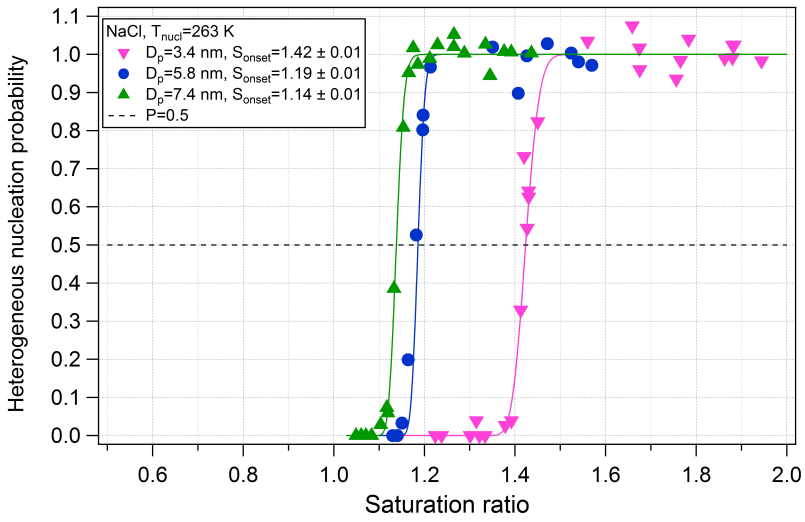

Figure 5.11: Experimental heterogeneous nucleation probabilities for soluble NaCl particles at constant nucleation temperature (263 K) as a function of water vapor saturation ratio. Solid lines are given to guide the eye. The effect of particle size according to theory can be observed.

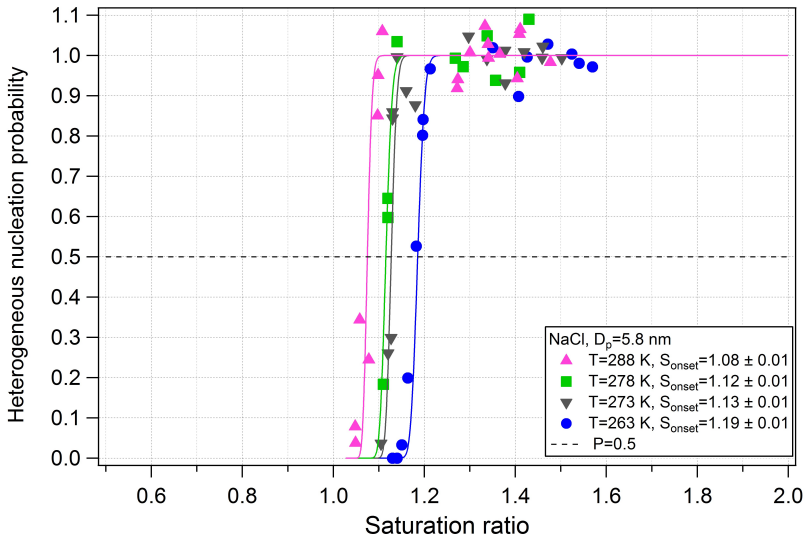

Figure 5.12: Experimental heterogeneous nucleation probabilities for soluble NaCl particles (5.8 nm) at various nucleation temperatures as a function of water vapor saturation ratio. Solid lines are given to guide the eye. The effect of nucleation temperature according to theory can be observed

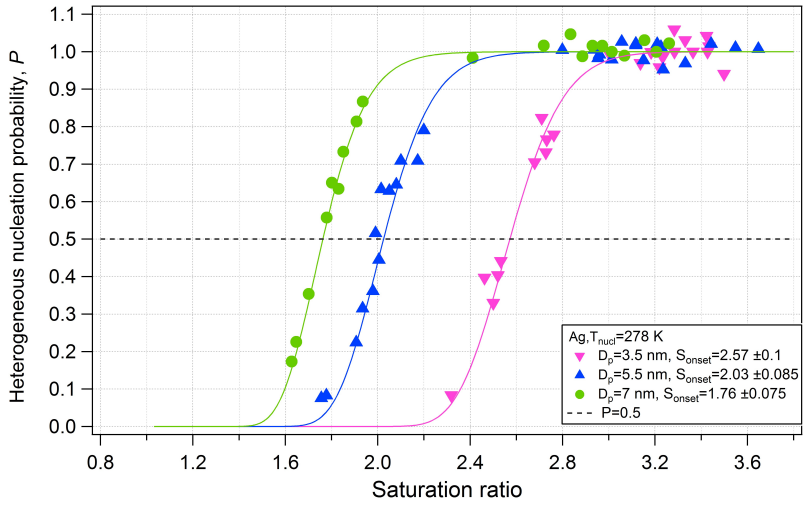

Figure 5.13: Experimental heterogeneous nucleation probabilities for insoluble oxidized Ag particles at one nucleation temperature (278 K) as a function of water vapor saturation ratio. Solid lines are given to guide the eye. The effect of particle size according to theory can be observed.

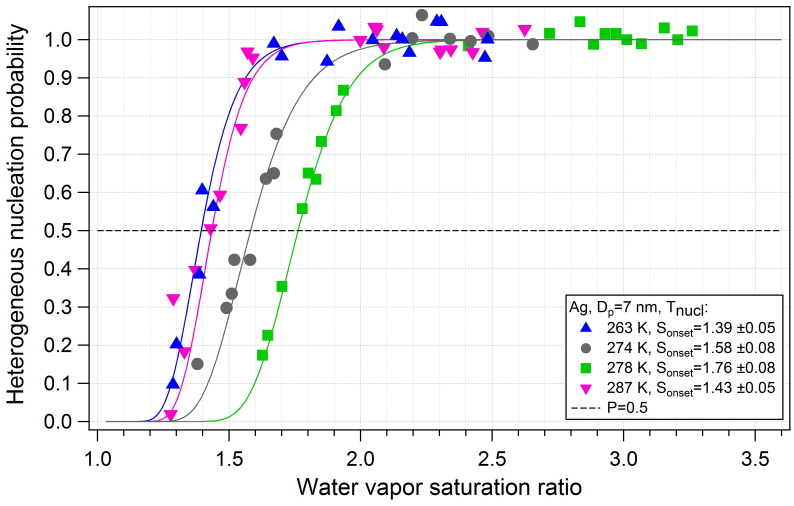

Figure 5.14: Experimental heterogeneous nucleation probabilities for insoluble Ag particles (7 nm) at various nucleation temperatures as a function of water vapor saturation ratio. Solid lines are given to guide the eye. The effect of nucleation temperature different to theoretical expectations can be observed.

5.5.4 Homogeneous nucleation of water vapor

A series of homogeneous nucleation measurements were undertaken to check for potential experimental artifacts. For measurements of homogeneous nucleation filtered humidified air was provided to the chamber. Adiabatic expansion resulted in high supersaturation (> 3.5) and homogeneously formed droplets appeared and were counted. These measurements were done at various nucleation temperatures between 255 and 278 K. Here we define onset saturation ratio S_{onset},hom as the saturation ratio corresponding to a nucleation rate of about 10^6 cm^{-3}s^{-1}. The latter was estimated by taking a drop concentration of 10^4 cm^{-3} and a nucleation time of 10 ms. From Wölk and Strey [164] we have obtained saturation ratios corresponding to the nucleation rate of 10^6 cm^{-3}s^{-1} for several nucleation temperatures and compared them with our data. The results are shown in Fig. 5.15.

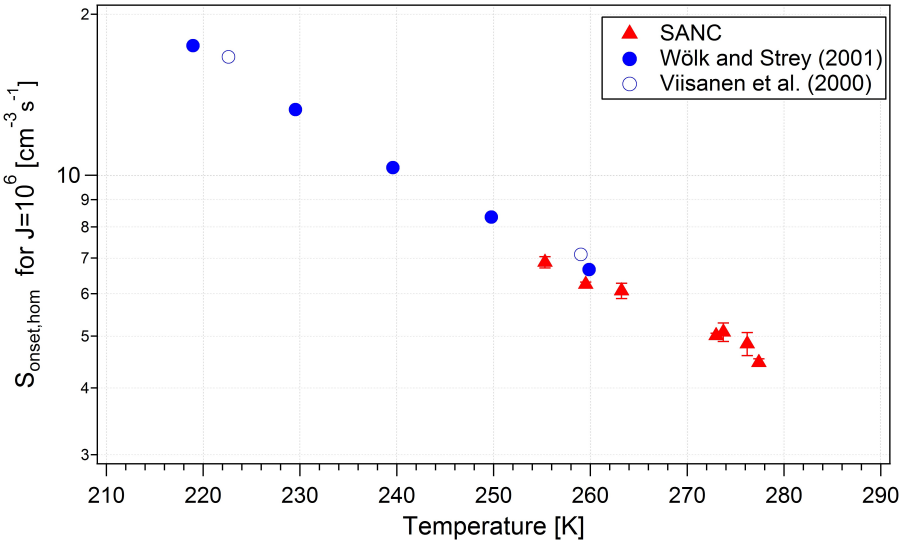

Figure 5.15: The experimental onset saturation ratio ($S_{onset,hom}$) for homogeneous nucleation of water vs. nucleation temperature.

It can be seen that our experimental results fit well to previously published data [144, 145, 164]. The onset saturation ratios are monotonously decreasing with increasing temperatures up to about 278 K in satisfactory agreement with the theoretical trend. According to these data a maximum $S_{onset,hom}$ at 278 K can be excluded and no unexpected results are observed. Considering these results there is no indication for a systematic experimental error causing strange behavior around

278 K. In contrast to homogeneous nucleation, for the heterogeneous nucleation on Ag particles we have observed a maximum of the onset saturation ratio at about 278 K (Figure 5.2). Only beyond this temperature we have found decreasing onset saturation ratios.

CHAPTER 6

LABORATORY CHARACTERIZATION OF A NEW NANO-WATER-BASED CPC 3788 AND PERFORMANCE COMPARISON TO AN ULTRAFINE BUTANOL-BASED CPC 3776 (PAPER IV)

PAPER IV (PUBLISHED)

Laboratory Characterization of a New Nano-Water-Based CPC 3788 and Performance Comparison to an Ultrafine Butanol-Based CPC 3776
Kupc, A., Bischof, O., Tritscher, T., Beeston, M., Krinke, T. and Wagner, P.E. **(2013)**, *Aerosol Science and Technology*, 47:2, 183-191
DOI:10.1080/02786826.2012.738317

ABSTRACT

This study provides insights into the performance of a new nano-water-based condensation particle counter (N-WCPC, TSI 3788) and presents a comparison to the well-established butanol- based ultrafine CPC (UCPC, TSI 3776). The suitability of the N-WCPC to measure ambient airborne nanoparticles of various compositions has been assessed with an urban background aerosol in a light industrial area and provided comparable results (within 2 %) to the 3776 at various particle number concentrations. The subsequent investigation using laboratory generated nearly monodisperse positively charged sucrose, sodium chloride, proteins, emery oil, and candle-generated particles in the diameter range of 2-53 nm showed material-dependent N-WCPC cut-off sizes between 2.2 and 17.2 nm at standard operating temperatures.

6.1 Introduction

Agarwal et al. [2] presented a description of a condensation particle counter (CPC) using butanol alcohol as the working fluid, which became the first commercial instrument capable of counting single particles down to about 7 nm, the model 3020 [136]. Since then butanol-based laminar flow CPCs have been the most commonly used [52]. It then took until 2004 when Hering and Stolzenburg [48] patented a method to use water as the condensing fluid in a laminar flow particle counting instrument.

This development lead to the first generation of commercially available water-based CPCs (WCPCs) introduced by TSI Inc. [50], the models 3782, 3785, and 3786. As water overcomes the main disadvantages of butanol as a working fluid, which are odor, flammability, and toxicity, WCPCs can be used in inhabited places, such as offices, homes, or clean rooms [49]. In recent years water has been revealed to be one of the most promising fluids in condensation-based techniques for particle counting. Its potential ability to facilitate the growth and detection of the smallest particles has been pointed out through theoretical considerations by Magnusson et al. [89] and De la Mora [25]. Building on the multitude of experiences with WCPCs in the field and in the laboratory as well as with extensive modeling, the next generation of a laminar flow WCPCs was developed. The new nano-WCPC 3788 (N-WCPC) as characterized in this study has a nominal detection limit of 2.5 nm, which was demonstrated for sucrose particle (same as for UCPC 3776).

One of the main advantages of particle counters is their ability to detect very low concentrations, while the size of the particles may be a limiting factor. CPCs are usually characterized by their counting efficiency defined to be the ratio of the particle number concentration measured by a CPC and the concentra- tion of a reference instrument, assuming that the latter has 100 % counting efficiency over the particle size range of interest. Research groups have been working on improving the performance of commercially available mainly alcohol-based condensation particle counters, in particular their ability to measure particle number concentration below 3 nm in diameter. Mostly this has been done by varying parameters such as flows and saturator/condenser temperatures or by using different types of condensing liquids. The detection of very small particles (< 3 nm) is of crucial importance for several scientific projects (such as Kirkby et al. [69]) investigating mechanisms of

new particle formation, which are currently still poorly understood.

This article will provide insights into the performance of the N-WCPC and present a comparison to the well-established UCPC, and will illustrate the suitability of the N-WCPC to measure ambient airborne nanoparticles of various compositions.

6.2 Experimental Methods

6.2.1 Instrument Description

The N-WCPC is a laminar flow WCPC (Figure 6.1). This newly developed N-WCPC differs from the UWCPC 3786 in several major aspects. First, the geometry of the growth tube has been optimized to kinetically limit droplet growth resulting in uniform droplet size independent of the particle concentration. Second, a new wick design and active water removal system have been implemented providing a more stable water system. Further, changes were made to the optical design and to the electronic signal detection to allow for better signal-to-noise ratios and accurate measurements at high particle number concentrations without using photometric mode. A pulse height analyzer was implemented to monitor the state of the supersaturation. Additionally, a filtered recirculating sheath airflow (0.3 L/min) is provided to focus the aerosol (0.3 L/min) along the centerline. The inlet flow can be set to either 0.6 or 1.5 L/min. The temperature of the conditioner is 15 °C, while the growth tube temperature is set to 75 °C.

Due to the design improvements, the response time of the N-WCPC has been reduced by a factor of four to 250 ms corresponding to a rise time of 45 ms. The upper concentration limit was increased by a factor of four to 400,000 particles/cm^3. Details on the WCPC measurement principle have been presented elsewhere [49, 50] hence, they are not described here.

The UCPC was chosen for the comparison as it has the same nominal cut-off size of 2.5 nm defined for sucrose. The main difference between the N-WCPC and UCPC operation apart from the different working liquids is the temperature setting of the saturator and the condenser. Due to the properties of butanol liquid, the temperatures of the saturator and condenser in UCPC are reversed (39 °C and 10

°C, respectively). Details on the UCPC performance have been presented elsewhere [67, 124, 131].

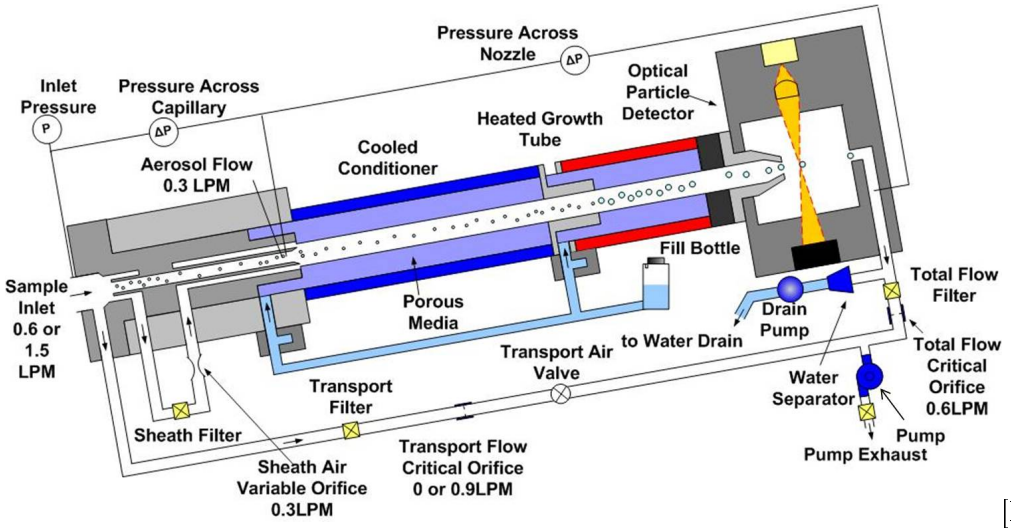

[H]

Figure 6.1: Schematic of the N-WCPC presenting flow structure. Individual parts such as cooled conditioner, (15 °C), heated growth tube (75 °C), and optical detector are indicated.

6.2.2 Aerosol Generation and Detection Set-up

The experimental schematic for characterization of the N-WCPC is presented in Figure 6.2. All measurements were performed at standard laboratory conditions and operating temperatures. To minimize diffusional losses, an inlet flow rate of 1.5 L/min was used for each particle counter and an aerosol electrometer (AE, TSI 3068B). Size distributions of test particles were determined by a scanning mobility particle sizer (SMPS, TSI 3936) consisting of an electrostatic classifier (EC, TSI 3080) with nano-differential mobility analyzer (nano-DMA, TSI 3085), and a UCPC as detector. The nano-DMA was operated at 10:1 sheath (20 L/min) to aerosol flow (2 L/min) ratio. Dilution air flow (2.5 L/min) and a mixing orifice (1.6 mm, used in TSI flow equalizers) followed by a flow splitter (TSI 3708) downstream of the nano-DMA provided uniformly mixed aerosol at a flow rate required by the counters and an AE (4.5 L/min in total). The flows were measured with mass flow meters (TSI 4140) and a Gilibrator bubble flow meter. The Aerosol Instrument Manager (AIM, TSI) software was used to record the data. Throughout the characterization, both

counters and the AE measured in parallel (Figure 6.2), with the exception during direct urban background aerosol and indoor air measurements where the AE was not implemented in the experimental setup. The diameter and the length of the conductive tubing between the flow splitter, AE, and counters were equal (11 cm) to assure identical losses. Nearly monodisperse positive singly charged particles with the diameter of interest were provided by manu- ally setting the voltage of the nano-DMA. Uniform mixing of the aerosol before detection and reproducible particle counting was confirmed through interchanging of the tubing connections on the flow splitter.

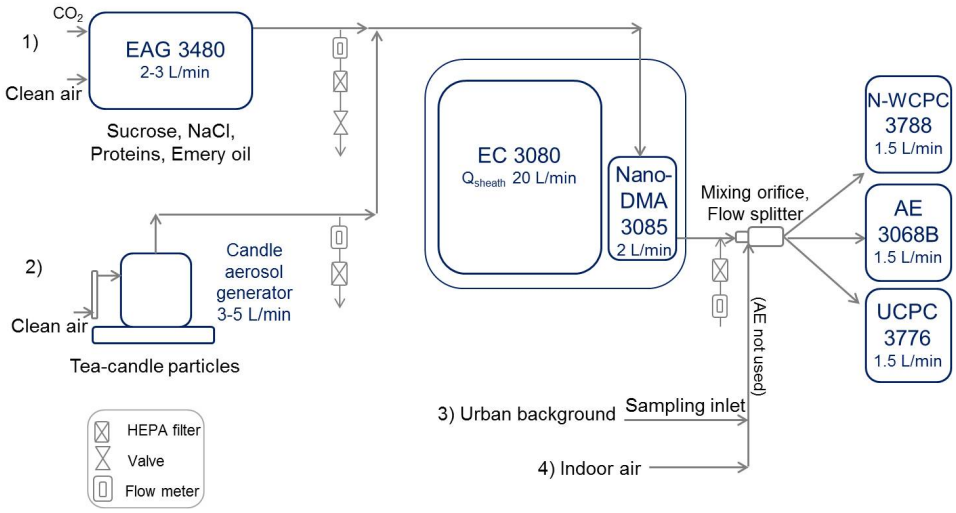

Figure 6.2: Schematic of the characterization setup with different used particle generation methods used, particle classification, and detection.

Samples

The urban background aerosol measurement was performed over a weekend (64 h, 27-30 January 2012) in a light industrial area near a bus depot and motorway in Aachen, Germany, using the setup described in Figure 6.2. The sampling site was about 50 m away from the road and about 200 m away from the freeway (A544). Both, N-WCPC and UCPC, measuring total number concentration, were sampling through a flow splitter and conductive tubing of the same length from a common sample inlet located outside the building and about 3 m above the ground level. Due to the low temperature (around -3 °C) and subsequent low relative humidity

of the sample, this case can be seen as a worst case scenario for the N-WCPC. Additionally, a comparison of indoor air particle number concentrations was made overnight (14 h) utilizing the same configuration.
Positively charged, nearly monodisperse particles of seven different materials in the size range between 2 and 53 nm were generated with the electrospray aerosol generator (EAG 3480, TSI; Figure 6.2) [86]: (1) sucrose, (2) sodium chloride (NaCl), (3) emery oil (EO), proteins: (4) ubiquitin, (5) albumin, (6) ferritin, and (7) candle aerosol.

Sucrose, NaCl, and protein solutions were prepared in a standard 20 mM ammonium acetate buffer solution with a conduc- tivity of 0.2 S/m (Chen et al. 1995). The concentrations used in the study ranged between 1 and 2000 ppm (parts per million) for NaCl and 1-1500 ppm for sucrose. Proteins obtained from Sigma Aldrich (St. Louis, MO, USA) included: (*a*) albumin from bovine serum (A7638); (*b*) ubiquitin from bovine erythrocytes (U6253); and (*c*) ferritin from equine spleen (F4503). Individual proteins were dissolved in buffer using an ultrasonic bath. Unlike for other particle material listed above, the diam- eters of proteins are independent of sample concentration, thus 10 μg/mL (10 ppm) concentrations were prepared and therefore highly monodisperse sizes between 3 and 13 nm were investigated.

Furthermore, EO (poly-alpha-olefin, PAO 4 cSt) providing synthetic lube oil spherical particles was generated between 6 and 53 nm by two EAGs of the same type. The additional EAG designated only for EO calibration and operating at higher than standard EAG backing pressure (1100 mbar) was used as a reproducibility check. Buffer and EO solutions were prepared according to calibration standard procedure described by the manufacturer (TSI Application note EM-004, TSI Inc., Shoreview, MN, USA) to obtain mode size diameters at 23 and 51 nm. These were investigated and used as stock solutions. Further dilutions provided samples with size distributions at lower particles sizes. On the contrary to proteins, dilutions of the stock solutions for EO, sucrose, and NaCl allow to shift the size distribution to lower particle sizes.

The tea-candle aerosol generator (Figure 6.2) was utilized to produce an aerosol to study the response of the N-WCPC to particles without precisely defined chemical composition. The candle was lit in advance to provide a steady burning phase (no smoldering) prior to sampling. It was placed on the bottom of the stainless

steel homemade candle aerosol generator (cylindrical chamber: 27 cm in height, 7 cm inner diameter, 12 cm outer diameter; Figure 6.2). Clean dry pressurized air (3-5 L/min) passing through the chamber provided a uniformly dispersed aerosol flow at the top outlet. Small windows located along the wall enabled confirmation that the candle was burning. The excess aerosol flow was removed through the valve downstream of the generator (high-efficiency particulate air (HEPA) filter used at lower flows).

6.2.3 Data Analysis

In the urban background and indoor air aerosol evaluations, data were averaged over 5 min periods at 1 s time resolution (300 data points). In the laboratory studies, the counting efficiencies (η) for the two CPCs were determined for each particle material using the ratio of the particle number concentration measured by CPC to the concentration determined by the AE. Each data point (=f(d_p, material)) was obtained by the average of at least three data sets of 2 min at 1 s time resolution. Experiments were repeated on different days to assure day-to-day reproducibility. The counting efficiency, η, ideally reaches unity for large diameters and drops down to zero for decreasing particle sizes due to losses within the instrument and decreasing nucleation (activation) probability. An empirical three-parameter function [156] was used to fit the counting efficiency data:

$$\eta = a - exp\left(\frac{D_1 - D_P}{D_2}\right) \tag{6.1}$$

This equation can be used to calculate the cut-off diameter D_{50} , where the counting efficiency eta reaches half of its maximum value. In xx Equation (1) the parameter a describes the maximum value reached by the counting efficiency, which usually should be close to 1. Parameters D_1 and D_2 are characteristic diameters for each curve and D_1 is close to D_{50}, D_2 is lower and may be considered as the diameter where the CPC does not count any particles [154].
Diffusional loss and multiple charge corrections were made with the AIM software based on the size distribution measurements using SMPS. Since the length of the tubing between the flow splitter and the three instruments was equal and the instruments ran at the same flow rate, no correction factor for particle losses has been applied.

The classified particle concentration recorded by AE was usually above 1000 particles/cm^3 with few exceptions recorded at 500 particles/cm^3. Additionally, the effect of concentration on the counting efficiency was studied, as well as the uniformity of the aerosol leaving the flow splitter. The presence of multiply charged particles was negligible due to the use of the EAG that does not produce large particles above 70 nm in the operation mode used for this study. For this reason, the correction for multiple charges was not applied to the classified particle diameters up to 53 nm. According to Wiedensohler [155], particles below 20 nm carry one elementary charge at most, while the contribution of doubly charged particles to diameters between 20 and 70 nm is still practically negligible.

6.3 Results and Discussion

6.3.1 Ambient Aerosol Measurement

To present the suitability of the N-WCPC to measure nanoparticles in ambient aerosols, the total number of concentrations measured by the N-WCPC was compared with an UCPC during 64 h of urban background aerosol sampling. The site is located close to a bus depot and light industrial area, thus the particles investigated originate and are influenced by combustion and urban emissions. Size distributions are typically dominated by particles below 150 nm in diameter, with a mode around 30 nm dependent on the actual traffic level [11]. The concentration linearity between the two CPCs during 64 h urban background measurement is shown in Figure 6.3. These data were averaged over 5 min periods and demonstrate the excellent agreement between both particle counters, irrespective of the working fluid they use. Since the mode diameter occurs at a large enough size, all the particles are counted with 100 % counting efficiency.

The relative response of the N-WCPC and UCPC particle number concentration to urban background aerosol represents the average of 0.98. On average, the UCPC measured slightly higher (< 2 %) number concentrations. However, this small difference (within the instrument uncertainties) is not sufficient to suggest that the water affinity of measured particles was slightly lower than for butanol. It could have simply resulted from instability of the CPC flow. Indoor aerosol composition results usually as a combination of indoor and outdoor activities, and may include

bio-aerosols (bacteria, viruses, and fungi) and particles resulting from gas to particle conversion, e.g., during com bustion. The physico-chemical parameters of indoor generated aerosols are not well characterized and are location dependent. To study the response to particles from an indoor environment, another direct comparison of both CPCs was performed using aerosol measured inside the laboratory (14 h). Size distribution and size-selected particles were not studied here. The agreement between both CPCs is very good ($y = 1.05x$; $r_2 = 0.999$ for 5 min averages). Particle sizes most probably were above the cut-off diameter allowing 100 % activation in both counters.

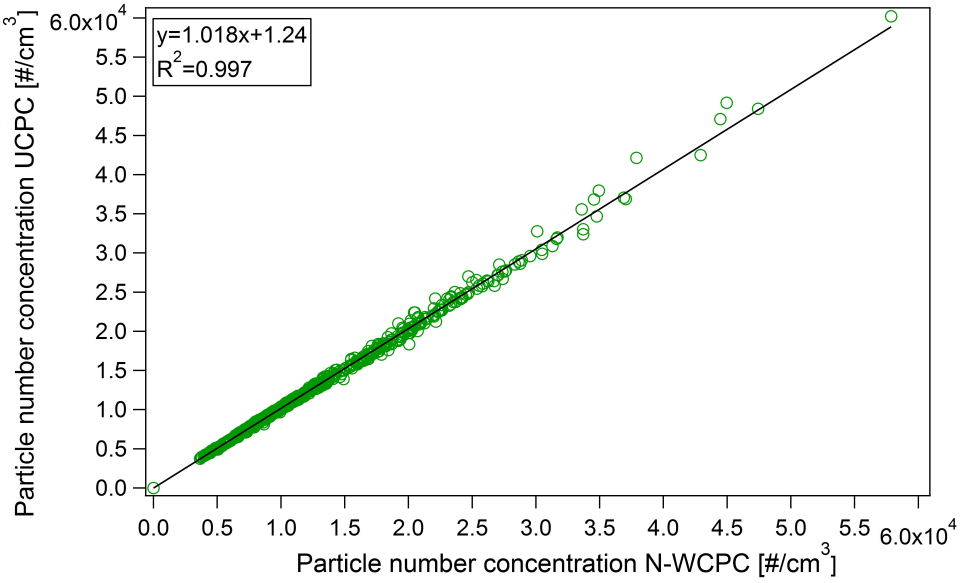

Figure 6.3: Direct comparison of the N-WCPC and UCPC number concentrations generated from sampling an urban background aerosol.

6.3.2 Counting Efficiency of N-WCPC and the Effect of the Particle Chemical Composition

Urban background and indoor air aerosol measurements have demonstrated that both CPCs can be used for measurements of outdoor airborne nanoparticles with various compositions. The performance of these instruments, although having the same cut-off size for positively charged sucrose particles, may be influenced not only by concentration but also by the chemical composition of the particles sampled

[78, 118]. Due to the different structure of water molecules being highly polar and butanol having polar and non- polar ends, some particles may have higher affinity for water than for butanol or vice versa.

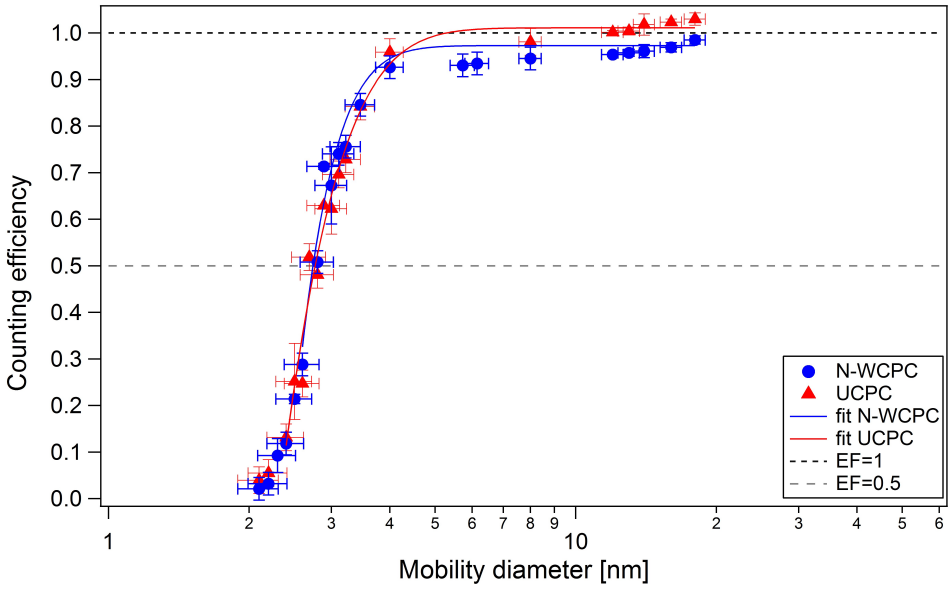

Figure 6.4: Cut-off diameters for the N-WCPC ($D_{50} = 2.7$ nm) and UCPC ($D_{50} = 2.8$ nm) for sucrose particles.

This dependence is demonstrated in the next section where the counting efficiencies for the N-WCPC, and UCPC for comparison, are studied using particles with various physico-chemical properties. The counting efficiency for the two CPCs for positively charged sucrose, NaCl, candle-generated aerosol, and EO is presented in Figures 6.4, 6.5, 6.6, 6.7, respectively. Solid lines correspond to fits according to Wiedensohler et al. [156], while dashed lines are presented to guide the eye. The horizontal error bars represent 1σ of the nano-DMA transfer function according to Stolzenburg [130].

The instrument flow stability has been considered to be included in the absolute error however is very small and accounts for only 0.04 %. The vertical bars result from the standard deviations of the mean counting efficiencies at a particular diameter. For the N-WCPC, the standard deviation of the counting efficiency was found to be between 5 % and 10 %. The width of the primary test particle size

distribution (geometric standard deviation) for sucrose was σ_g = 1.3-1.4; NaCl σ_g = 1.1-1.7; proteins: ferritin σ_g = 1.25; ubiquitin σ_g = 1.48; albumin σ_g = 1.56; EO σ_g = 1.4-1.7; and candle-generated particles σ_g = 1.4-1.67.

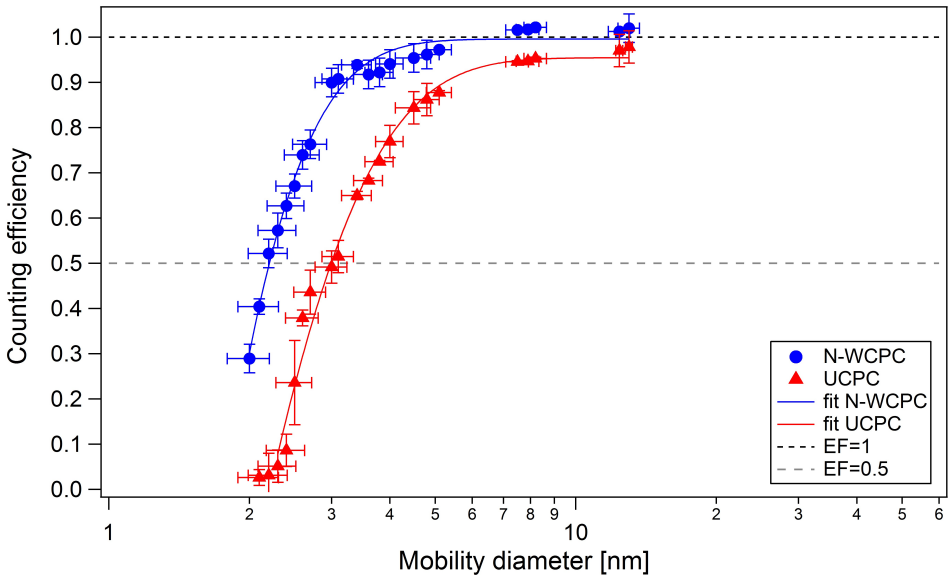

Figure 6.5: Counting efficiency data for the N-WCPC (D_{50} = 2.2 nm) and UCPC (D_{50} = 3 nm) for NaCl particles.

Sucrose and NaCl aerosol were chosen due to their solubility in water. The cut-off size for sucrose is similar for both counters (D_{50} = 2.7 nm for N-WCPC, and D_{50} = 2.8 nm for UCPC) and is approximately within the error bar when comparing with the specification given by the manufacturer (D_{50} = 2.5 nm; Figure 6.4). Furthermore, the counting efficiency curve for the N-WCPC appears to be slightly steeper than for the UCPC.

Measurements performed using NaCl particles show an enhanced activation in water (Figure 6.5). The resulting cut-off diameter (D_{50}= 2.2 nm) is even smaller than the one for sucrose. Although both sucrose and NaCl are hygroscopic, the sensitivity to detect and count NaCl is higher. This enhancement for more hygroscopic NaCl has been observed in previous studies [106]. The difference might be due to the properties of these two materials, with sucrose having a spherical structure and being composed of molecules, while NaCl is composed of ions and is cubic, and the

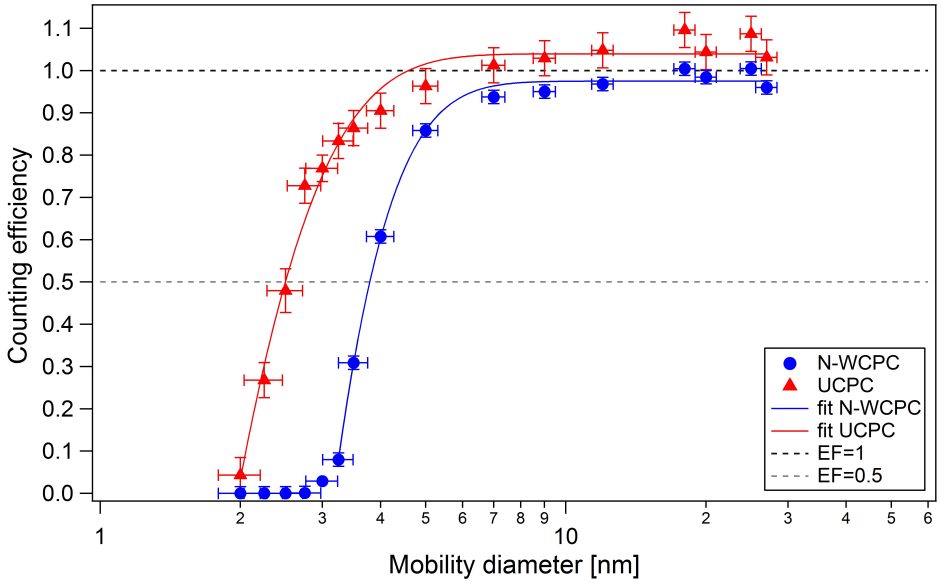

Figure 6.6: Counting efficiency data for the N-WCPC (D_{50} = 3.8 nm) and UCPC (D_{50} = 2.5 nm) for the candle-generated particles.

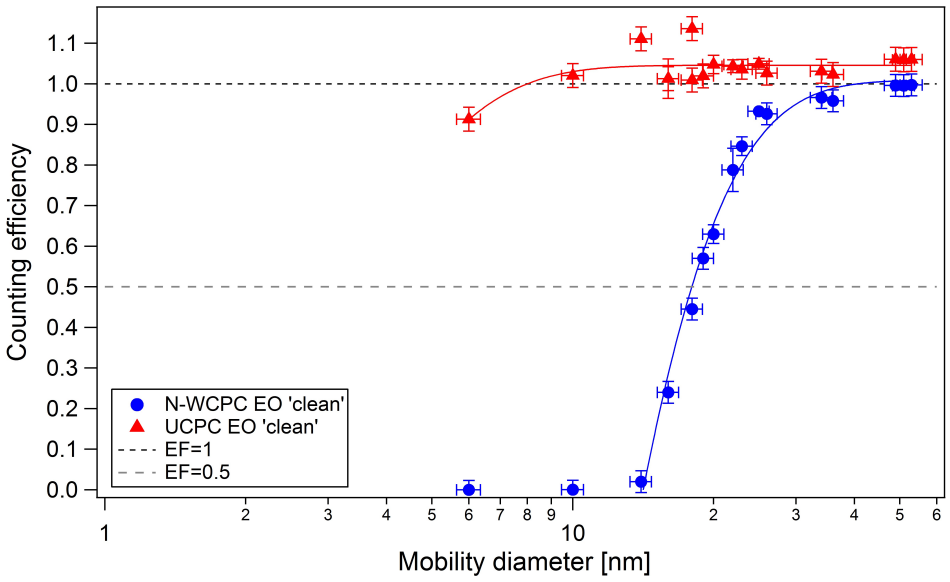

Figure 6.7: Counting efficiency data for the N-WCPC (D_{50} = 17.2 nm) and UCPC (D_{50} <3.4 nm) and clean emery oil. Reproducibility check was performed using two individual EAGs'.

affinity of water seems to be higher for NaCl (Figure 6.4, 6.5). According to Raoult's law, the reduction of equilibrium vapor pressure by the salt could be the reason for NaCl being activated at sizes below the nominal activation cut- off diameter [50]. The activation efficiency in WCPCs increases for hygroscopic particles [50], and the ability of particles to act as a condensation nuclei can be influenced by the chemical parameter such as wettability or solubility of the particle in the condensing liquid [78]. This material dependence can be observed for the UCPC counting less NaCl particles than the N-WCPC (Figure 6.5). The cut-off size for this particular material is 3 nm, slightly higher than for N-WCPC suggesting a higher particle affinity for water than for butanol. The cut-off size results for the UCPC using NaCl are in agreement with published results by Stolzenburg and McMurry [131].
The cut-off sizes (D_{50}) calculated from the fits 6.1 and the fitting parameters according to Wiedensohler [156] for the materials studied here are summarized in Table 6.1.

Table 6.1: Summary of all fit parameters a, D_1, D_2, and mean D_{50} (cut-off diameters for Equation 6.1 and the N-WCPC. Additionally D_{50} measured for the UCPC and literature references are presented

	Fit parameters N-WCP			N-WCPC	UCPC	Literature reference: D_{50}	
						UCPC[a]	UWCPC[a]
Substance	a	D_1 [nm]	D_2 [nm]	D_{50} [nm]	D_{50} [nm]	[nm]	[nm]
Sucrose	0.97	2.41	0.45	2.7	2.8	2.5[b]	2.4[c]; 2.5[d]
NaCl	1	1.78	0.61	2.2	3.0	4.1[e]	
Candle	0.98	3.15	0.86	3.8	2.5		
Emery oil	1.09	14.2	5.58	17.2	< 3.4		
Proteins	n.a.	n.a.	n.a.	≥ 3	≤ 3		
Silver	–	–	–	–	–	3.3[e]; 3.2[f]	4.4[4]; 4.5[g]; 3.9[f]

[a]At standard working temperatures.
[b]Specified by the manufacturer.
[c][86] and [d][33] used residue particles from ammonium acetate buffer and a custom UWCPC and UCPC 3025a, respectively, as a reference
[e][51]
[f][97]
[g][78]

Further tests for candle-generated aerosol (Figure 6.6) resulted in a slightly lower cut-off diameter for the UCPC (D_{50} = 2.5 nm) than for the N-WCPC (D_{50} = 3.79 nm) suggesting the presence of substances with a higher affinity for butanol than for water, e.g., organic compounds. The effect of affinity preference was observed by Petersen et al. [107] where the heterogeneous nucleation of water-propanol vapor

mixtures on nearly monodisperse NaCl particles (soluble in water, and practically insoluble in propanol) was investigated. The shape and steepness of the counting efficiency curves is similar for the results described so far (Figures 6.4, 6.5, 6.6, 6.7, 6.8).

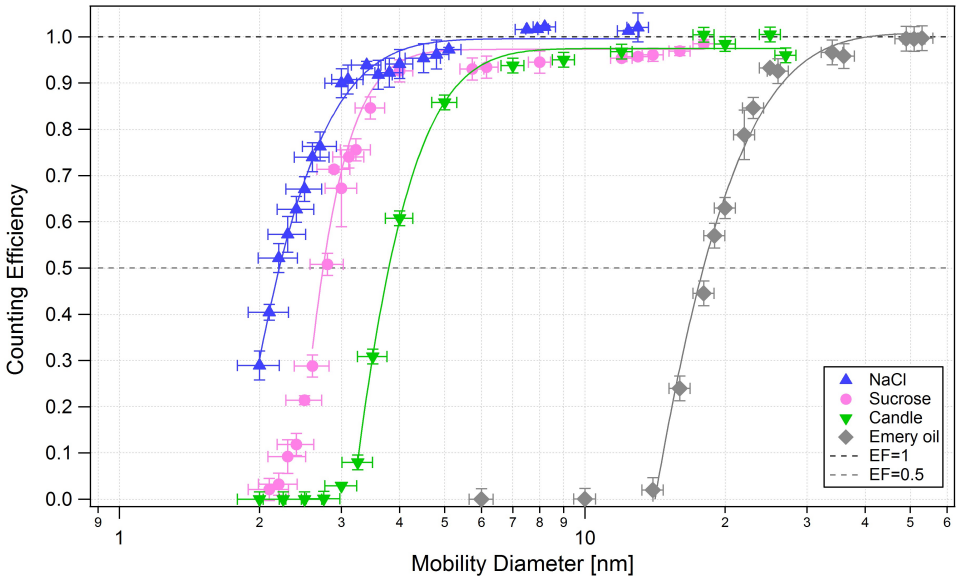

Figure 6.8: The detection efficiencies for particles with different chemical composition for the N-WCPC as compared with a reference AE. The triangular symbols represent NaCl, circles represent sucrose, rotated down triangles represent candle aerosol, and diamonds represent EO particles. The corresponding fit parameters and D_{50} are presented in Table 6.1. The dashed lines are presented to guide the eye.

The identification of the chemical composition of candle- generated particles is complex and has not been included in this study. According to the literature, tea candle consists of paraffin (mostly solid) made of heavy straight chain hydrocarbon from crude oil and may contain some additives, however, the composition of the particles generated is not precisely known. Zai et al. [167] described three candle burning modes that can be distinguished including steady, unsteady, and smoldering. In the first type, particles emitted are invisible and dominated by a high number in the ultrafine particle size range; unsteady burn produces black smoke and a bimodal size distribution (10-500 nm). In this study, particles of a steady burning candle were classified, and reproducible size distributions were measured, which ranged between 2 and 40 nm. In some studies, aldehyde beside other material

compounds and lead were detected in candle smoke [167]. To find out whether the test aerosol was composed of soot, we placed a tissue at the aerosol generator outlet (Figure 6.2) and left it there for 20 min. Since no visible deposit was observed, we assume the lack of soot in our test aerosol. Additional measurements would be advised to define the components of the candle-originated particles.

On the other hand, the composition of EO is known. EO is characterized by a low affinity for water (big contact angle). It is a nonsoluble, isoparaffinic polyalphaolefin composed of 1-decene (tetramer) mixed with 1-decene (trimer), and hydrogenated, consisting usually of 82-85 % $C_{30}H_{60}$ and 13-16 % $C_{40}H_{80}$ polyalphaolefins by volume [42]. For very pure EO particles, the cut-off size is measured at 17.2 nm for the N-WCPC, while for the UCPC it is expected to be below 3.4 nm (Figure 6.7). Even higher cut-off size for clean EO was found in other studies [85] where the D_{50} for the WCPC was above 60 nm. Moreover, the presence of contamination in the EO sample, e.g., sucrose will shift the cut- off diameter to smaller sizes as observed in Liu et al. [85], or as in the case of dioctyl sebacate (DOS) with added NaCl in Hering et al. [50]. This indicates that the presence of other materials in the sampled particles may increase the counting efficiency due to an enhanced wettability triggered by lowered vapor pressure due to dissolved solids. In addition, Rader et al. [115] observed the influence of evaporation on the particle diameter. For DOS, dioctyl phthalate, and oleic acid particles, the evaporation due to the residence (2 min) time may result in reduced particle diameters between the classification and the detection stage. In this study, this should not be the case due to the short residence time (from generation to classification stage) of well below 1 s. However, the potential evaporation in the saturator/condenser could lead to instability of those organic droplets resulting in a decreasing particle diameter and leading to more difficult activation of smaller particle sizes in the N-WCPC. The effects may be significant for smaller particle sizes Rader et al. [115] observed a sharp increase in the evaporation rate at smaller diameters, which is consistent with the exponential dependence on diameter of the Kelvin effect.

According to the EO specifications given by GMZ Inc. (West Chester, OH, USA [43]), the EO vapor pressure is 13.3 kPa (100 mm Hg) and the melting/freezing point between 22 °C and 26 °C. For this particular case, the material dependence is clearly visible, as the cut off size for hydrophobic EO particles measured at 17.2 nm decreases to D_{50}=2.2 nm for hygroscopic NaCl particles (Figure 6.5, 6.7, 6.8).

For hygroscopic particles (sucrose, NaCl), the counting of the N-WCPC is higher or similar as for the UCPC for small particle sizes, and opposite for hydrophobic materials (e.g. EO). In further measurements, we have electrosprayed three different proteins, ubiquitin, albumin, and ferritin, having a diameter of 3, 6.5 and 12 nm, respectively.
In general, proteins are nearly monodisperse, nonhygroscopic, and their affinity for water is low. Since each protein type is characterized by a different material, the counting efficiency curves are not drawn here. Efficiency calculations were done in the same way as for the other materials described previously and are presented in Figure 6.9. As expected due to protein's low water affinity, the butanol-based UCPC counted more particles than the N-WCPC. Unlike in other studies, the protein solutions were not filtered and purified in a centrifuge, however, the size distributions measured were similar to those measured by Adou and Johnston [1], e.g. for albumin.

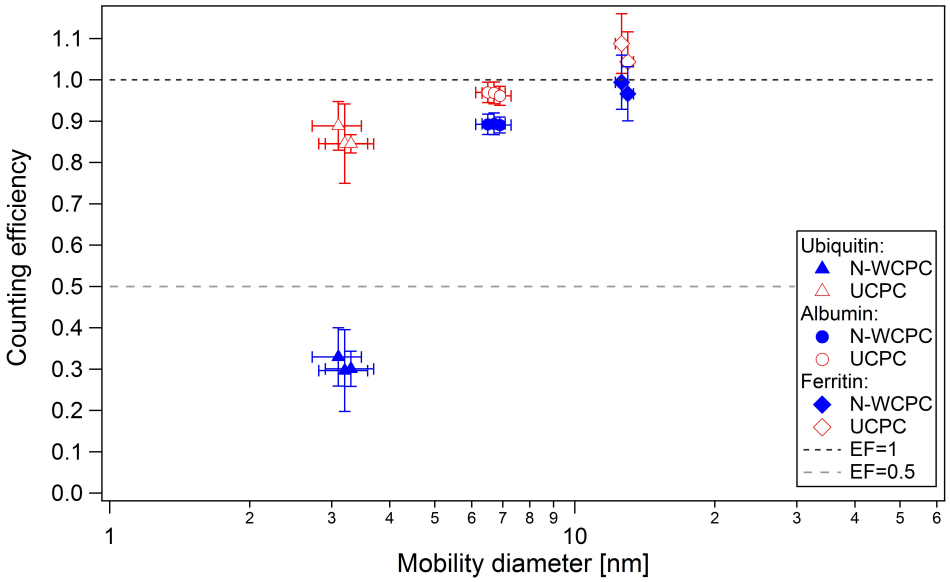

Figure 6.9: Counting efficiency data for the N-WCPC and UCPC for three different proteins (albumin, ubiquitin, and ferritin). Due to low water affinity for protein the performance of UCPC is better. The dashed lines are indicated to guide the eye. Due to the lack of data points and variety of aerosol, it is not possible to fit the detection efficiency curve.

Stolzenburg and McMurry [131] and Winkler et al. [162] observed that the polarity of the particles may influence the counting efficiency. The latter study has shown

that negatively charged particles requires a smaller supersaturation to be activated and grow to optically detectable sizes than positively charged particles, as is used in this study.
Although the N-WCPC shows higher sensitivity to the material used, it was negligible for ambient particles with the mode diameter above its cut-off size allowing for 100 % detection. For both hydrophilic NaCl and sucrose particles, the N-WCPC detects particles as small as 2.2 and 2.7 nm, respectively (Figure 6.8). For urban background and indoor aerosol, the agreement between these two instruments is very good. This clearly illustrates the possibility of the N-WCPC to serve as an alternative to the butanol-based UCPC.

6.3.3 The Effect of Particle Number Concentration on Counting Efficiency

Particle number concentration measured in single particle counting mode depends on the number of counts of high signal-to-noise particle events, flow rate, and time [50]. Increasing particle concentration may result in decreasing counting accuracy due to particle coincidence. This effect has been briefly studied here using nearly monodisperse sucrose particles. Figure 6.10 presents the linearity between particle number concentration measured by the N-WCPC and a reference instrument, the AE (TSI 3068B).

The concentration ranged between $1x10^3$ and $7.7x10^4$ particles/cm^3 for diameters between 8 and 18 nm. The agreement between these two instruments is very good indicating a negligible effect of the high particle concentration on the counting efficiency of the N-WCPC. The maximum studied concentration was found to be within 5 % of the reference AE value ($7.7x10^4$ particles/cm^3) at a particle diameter of 16 nm

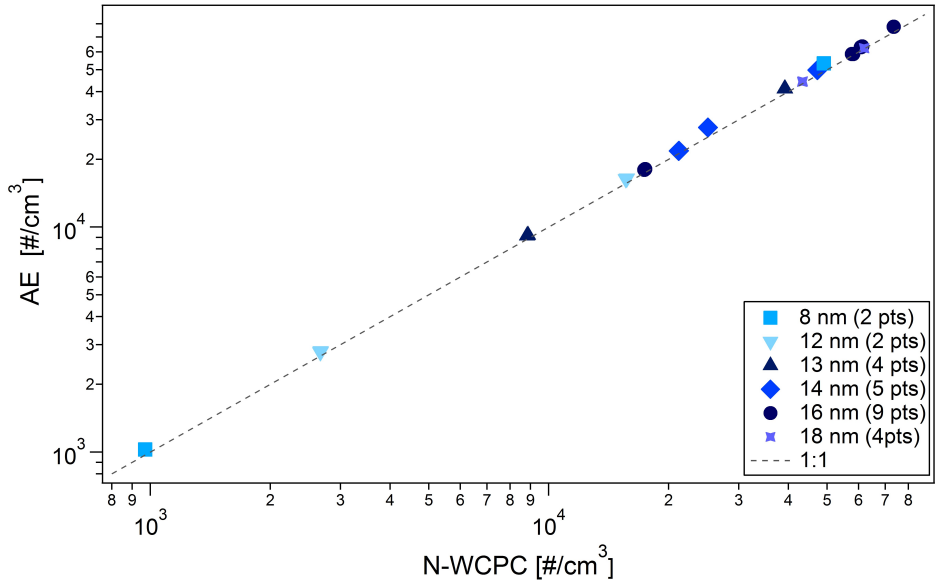

Figure 6.10: The particle number concentration linearity between the N-WCPC and an AE (TSI 3068B). Nearly monodisperse sucrose particles with diameters between 8 and 18 nm were studied. Numbers in the brackets indicate number of data points (pts) taken for certain particle diameter.

6.4 Conclusion

This study reports on the performance of the new N-WCPC (TSI 3788) according to a comparison with the well-established UCPC (TSI 3776) that was used as counting reference due to its identically specified lower cut size for positively charged sucrose particles. For ambient aerosol, measurements performed for an urban background aerosol and indoor air over a wide range of particle number concentrations between 2700 and 60,000 cm^{-3} and particle diameters allowing for 100 % counting showed the results of both CPCs to be within 2 %. Counting efficiencies measured for sucrose, NaCl, candle aerosol, EO, and proteins (albumin, ubiquitin, and ferritin) range for the N-WCPC between 2.2 and 17.2 nm. The smallest cut- off of 2.2 nm was found for NaCl using the N-WCPC. For sucrose particles, the cut-off was similar for both CPCs (2.7 for the N-WCPC vs. 2.8 nm for the UCPC) and within the experimental error as compared with the cut-off size specified by the manufacturer (TSI, 2.5 nm).

This study has shown how the complexity and variability of the particle composition may influence the counting efficiency of an instrument and impact its lowest cut-off size. Furthermore, for an unknown particle composition (e.g. candle aerosol), the difference in CPC responses may provide additional information on the properties of the particles measured (e.g. hygroscopicity) such as the affinity to one or the other liquid used. For specific nonpolar particle materials, the N-WCPC has shown some material dependency whereas it was negligible for the real life ambient indoor and outdoor aerosols tested in this study. Our findings are encouraging for further investigations on the effect of saturator/condenser temperatures on the detection efficiency. Based on the results of previous studies [73, 106], a higher temperature difference would surely result in lower cut-off sizes.

Acknowledgements

This research has received funding from the EC's Seventh Framework Programme under the grant agreement no. 215072 (Marie Curie Initial Training Network 'CLOUD-ITN'), and from the Austrian Science Fund (project no. P 19546, L593).

CHAPTER 7

CONCLUSIONS

The uncertainty in the net radiative forcing attributed mainly to aerosols is extremely difficult to quantify due to their variability [54]. The most radiatively relevant properties of aerosols are their composition and size distribution. Using those two parameters aerosol light scattering characteristics can be described. So far aerosol formation mechanisms, referred to as nucleation, have not yet been clarified and those are of crucial importance since they define specific aerosol properties. Whether aerosols form through homogeneous, heterogeneous or ion-induced nucleation in the atmosphere their formation mechanisms are not yet fully understood. The representation of physical mechanisms of aerosol formation in climate models is at the moment the main source of uncertainty in climate predictions [123].

In the framework of this PhD research fundamental understanding of nucleation mechanisms has been advanced helping to bridge the knowledge gap in the particle-aerosol-cloud-climate interactions. A significant progress on aerosol nucleation as described in this thesis has been achieved through:

(1) Providing a stable, desired and reproducible concentrations of sulfuric acid in the CLOUD chamber by means of an unique fibre-optic UV system **(Chapter III/ Paper I)**

(2) Studying homogeneous nucleation and particle growth at the CLOUD chamber and the effect of various vapors, ionizing radiation and temperature **(Chapter IV/ Paper II)**

(3) Studying heterogeneous nucleation of water vapor on neutral soluble and insoluble seed particles and the effect of temperature using SANC expansion chamber **(Chapter V/ Paper III)**

(4) Studying the effect of particle properties on the response of condensation particle counters utilizing different working liquids **(Chapter VI/ Paper IV)**

This was achieved using state-of-the-art aerosol- and gas-phase instruments at the CLOUD chamber for (1 and 2), and expansion type CPC (SANC) for (3), as well as commercially available laminar-flow water- and n-butanol-based particle counters in the laboratory for (4). The summary of the main scientific results achieved in this PhD work is provided in the following.

7.1 The effect of vapors, ions and temperature on atmospheric nucleation as performed at the CLOUD chamber (Paper I and II)

The recently developed CLOUD chamber at CERN has proved to be a state-of-the-art facility to investigate atmospheric nucleation and particle growth with a unique possibility to quantify the effect of ionizing radiation. CLOUD chamber provides a clean and thermally stable environment and allows for the simulation of different atmospheric conditions including temperature, relative humidity, trace gas (such as SO_2, O_3) concentration or solar radiation. The contents of the chamber were continuously monitored by state-of-the-art aerosol- and gas phase- instruments.

To investigate the effect of ionizing radiation and temperature on binary (H_2SO_4-H_2 O) and ternary (H_2SO_4-H_2O-NH_3) nucleation a stable concentration of sulfuric acid, one of the key components taking part in atmospheric nucleation, is required. Therefore an innovative fibre-optic UV system was installed at CLOUD chamber to trigger photochemical reactions by the same mechanisms as in the atmosphere. Concentrations of sulfuric acid produced in the CLOUD chamber through ozone photolysis and further OH reaction with SO_2 have proven to be stable and reproducible [80] **(Chapter III/ Paper I)**. The fibre-optic UV system described in this work has shown only negligible thermal effect, which is of crucial importance in nucleation studies. Nucleation is sensitively dependent on temperature and any

thermal changes can produce spurious formation of new particles. So far such high thermal stability has not been achieved in another comparable experimental set-up. This fibre-optic system is a powerful tool in nucleation studies as it a) is suitable to operate at any temperature between 183 and 300 K, b) provides reasonably uniform chamber illumination and c) in combination with other gases is capable to generate various photochemical reactions as in the atmosphere.

In-situ production of sulfuric acid at the CLOUD chamber allowed for the investigation of homogeneous binary and ternary nucleation and the effects of temperature and galactic cosmic rays (GCR, ionizing radiation) on these processes **(Chapter IV, Paper II)**. The nucleation rates J ($cm^{-3}s^{-1}$) were measured under neutral (J_n), galactic cosmic rays (J_{gcr}), and charged pion beam (J_{ch}) conditions [69].

Results have shown that both mechanisms cannot account for atmospheric boundary layer nucleation and that another component such as an organic compound is missing. The exact role of organics in nucleation processes remains unclear.
However, for the binary and ternary processes investigated here an ion enhancement has been observed for all considered temperatures (248, 278 and 292 K). Nucleation rates at CLOUD were measured as a function of H_2SO_4 concentration and temperature. For binary nucleation at low temperatures, a lower concentration of H_2SO_4 was found to be sufficient to maintain the same nucleation rates due to decrease in the H_2SO_4 saturation vapor pressure [69]. Results indicate that at natural conditions of the troposphere (cool temperature) and atmospheric sulfuric acid concentrations ion-induced binary nucleation proceeds at significant rates. This is the first global assessment of free tropospheric nucleation since previously reported studies were mainly based on the theoretical estimates and empirical assumptions.

Investigations of ternary nucleation involving ammonia resulted in increased nucleation rates and the presence of ions enhanced the formation of sulphuric acid clusters. However, at naturally occurring concentrations of H_2SO_4, nucleation rates were found to be significantly smaller than those measured in the atmosphere. This confirms the thesis already stipulated by other experiments that the presence of organics is required to explain nucleation processes in the atmosphere. These results contradict the assumption of climate modeling that only NH_3 is required to explain nucleation mechanisms. Thus, climate models should consider results reported here.

Findings reported in this study provide significant improvement in understanding aerosol formation and provide means for more adequate input parameters such as formation and growth rates used in climate models thus improving accuracy of predictions. Nucleation rates will remain highly uncertain unless chemical composition of the atmospheric system is understood. Such uncertainty for nucleation processes could highly influence cloud predictions through inadequate model assumptions of particle growth or concentration. Thus, further investigations are necessary. Since the mechanisms of nucleation are not precisely known the influence of GCR on aerosol and cloud formation cannot be quantified and is still poorly understood, however a potential link may exist. To quantify the effect of the latter further research needs to be carried out involving organics as recently investigated at CLOUD. Only then the effect of ions for atmospherically relevant conditions can be established.

7.2 The effect of particle size, composition and temperature on heterogeneous nucleation using SANC expansion chamber (Paper III)

Investigations of heterogeneous nucleation are crucial as aerosol particles in the atmosphere may also form on pre-existing seeds. Since the study of Wilson [158] on the influence of ions on water nucleation no other study than the one reported in Chapter V has been published on the heterogeneous nucleation of water vapour on particles < 4 nm and the effect of temperature.

As has been reported temperature is a critical factor in heterogeneous nucleation processes. Temperature dependence has recently gained attention especially as unusual temperature trends of heterogeneous nucleation were reported [121]. According to McGraw et al. [91] this unusual behavior may be related to strong seed surface effects. In the framework of this PhD the effect of particle properties (Ag and NaCl) and temperature (263-288 K) on heterogeneous nucleation of water vapour using expansion type CPC (SANC) was studied **(Chapter V/ Paper III)**.

The experimental set up included SANC expansion chamber, vapor and particle generation units. Vapor supersaturation achieved by adiabatic expansion trig-

gered formation and growth of liquid droplets, which were further optically detected by the Constant Angle Mie Scattering Method (CAMS). Heterogeneous nucleation probabilities as a function of vapor supersaturation, particle size, and nucleation temperatures were measured for neutral silver and sodium chloride particles with various diameters (3.4-7.8 nm).

Results described in this work have revealed an unexpected temperature trend for silver seeds where the onset saturation ratio exhibits a pronounced maximum at about 278 K [81]. The effect for sodium chloride particles however, was found to be in qualitative agreement with theory. Proposed temperature dependent contact angle and water density function have not been able to explain this behavior. Thus, this trend is not yet theoretically understood, however - as suggested by McGraw et al. [91] - could be related to the particle composition - in particular to strong surface effects. To rule out the possible experimental artifacts, a series of homogeneous nucleation experiments for water vapor at various temperatures were performed. These results were found to be in good agreement with previously published data and do not show any irregular temperature trend indicating the proper operation of the experimental system. Those findings are highly relevant for both fundamental and instruments aspects.

Further studies on the particle composition, temperature dependence using water and other various vapors is needed to better understand temperature effects. Also the effects of single and multiple charges would be of interest in this context.

7.3 The effect of seed particle composition on the response of condensation particle counters (Paper IV)

Since the nature of the particle may affect its activation and growth the effect of seed properties on the response of condensation particle counters was studied using water and n-butanol liquids. CPCs are the most common instruments used in nucleation studies and their performance may be critically influenced by specific properties of particles and working liquids.

The experimental set-up included nano-water based CPC (N-WCPC) and well-established butanol-based ultrafine CPC (UCPC) operating at their standard temperatures [82] **(Chapter VI/ Paper IV)**. An electrometer was used as a reference instrument. Particles with various physico-chemical properties generated by means of either electrospray or candle aerosol generators were further classified in a nano-DMA.
Cut-off sizes measured for sodium chloride, sucrose, candle aerosol, proteins and emery oil range between 2.2 and 17.2 nm for the N-WCPC. The smallest size of 2.2 nm was found for sodium chloride particles using water-based CPC. For sucrose particles, the cut-off size was similar for both CPCs and within the experimental error as compared with the indications of the manufacturer (2.5 nm).

Further, results of measurements performed with both particle counters for an urban background aerosol and indoor air in conditions allowing for 100 % counting, showed to be within 2 %. For specific nonpolar composition, the water based instrument has shown some material dependency that could considered to be negligible for real life ambient indoor and outdoor aerosols tested in this study.

The results provide an insight on how the variability and complexity of particles (such as composition, solubility, wettability, shape or size) may influence the activation and counting efficiency of a CPC-type instrument and impact its lowest cut-off size. Furthermore, when looking at particles with unknown composition (such as candle aerosol) the difference in counter responses could provide additional information on the particle properties such as whether it has higher affinity for water or n-butanol. Hence results described in this thesis may give justification for the choice of a certain instrument for the detection of specific particles.

7.4 Implications

Nucleation processes in the atmosphere are rather sporadic in time and space. In a polluted environment the available particle surface influences nucleation rates, while in non-polluted regions the nucleation rate is a function of the acid vapor formation rate. Precursor vapors taking part in nucleation are mainly produced in situ by photochemical processes such as sulfuric acid. Further the growth of particles may be influenced by the concentrations of available vapors (e.g. organics, ammonia, water) and temperature.

Investigations of nucleation mechanisms reported in this PhD thesis may lead to significant improvement of the basic understanding of nucleation processes as they take place in the atmosphere. Further, they will allow to more precisely incorporating particle formation in the climate models resulting in better predictions. In addition, findings described in this work may contribute to optimization of condensation particle counters and possible further development of these instruments.

7.5 Future work

After decades of basic aerosol research knowledge on nucleation processes is still a challenge. Nucleation, whether occurs on a particle emitted to the atmosphere or takes place in the atmosphere due chemical transformations [92], remains an open question. Despite the efforts in the aerosol research many aspects still need to be investigated to fully understand aerosol formation, aerosol-cloud interactions and further impact on climate. Various nucleation pathways in the atmosphere add to the complexity of this system.

Understanding these processes (physical and chemical) will require knowledge on the composition and concentration of their precursors (such as vapours, clusters). Identification of species responsible for nanoparticle formation and growth is needed to predict the impact on new particle formation on climate [126]. The number of molecules in critical cluster, the gaseous species involved in nucleation, their concentrations or the effect of ions on nucleation still remains unresolved.

Future research in condensation particle counter aspect should focus on multicomponent working fluids, further development of molecular based theoretical approaches to nucleation and further on the temperature dependence in both theory and experiment [91]. Molecular-scale interactions between seed particle surface and working fluid should be further tested using various vapours and nucleation seeds especially < 3 nm. Further, as unusual temperature trends have been observed pointing out for strong surface effects, one should further investigate those as well as the effect of the contact angle, wettability, solubility or charge effects (e.g. multiple charges) in water and in other vapors.
Moreover, theoretical developments and experimental studies at the microscopic levels are needed to resolve this multidimensional phenomenon. Further, development

of instrument detection thresholds is desired. Experimental measurements are not sufficient to progress on the mechanisms of particle formation in the atmosphere. Additional field, aircraft or satellite-based measurements greatly contribute to reduce the uncertainties in direct and indirect aerosol forcing. Further, an appropriate incorporation of particle formation and growth parameters in models should be pursued.

Bibliography

[1] Adou, K. and Johnston, M. (2009), Flow Interface for Charge-Reduced Electrospray of Nanoparticle Solutions. *Anal. Chem.*, 81: 10186-10192.

[2] Agarwal, J. K. et al. (1977), 'A Continuous Flow CNC Capable of Counting Single Particles', In Atmospheric Aerosols and Nuclei, Proceedings, 9th International Conference on Atmospheric Aerosols, Condensation and Ice Nuclei, Edited by: Roddy, A. F. and O'Connor, T. C. 118-122. Galway,Galway University Press.

[3] Aitken J. (1880), On Dusts, Fogs and Clouds, *Proc. Roy. Soc.*, 11:14,18

[4] Almeida et al., Manuscript in preparation

[5] Andreae, M.O. and Rosenfeld, D. (2008), Aerosol-cloud-precipitation interactions. Part 1. The nature and sources of cloud-active aerosols, *Earth-Science Reviews* 89, 13-41

[6] Arnold, F. (1980), Multi-ion complexes in the stratosphere-implications for trace gases and aerosol. *Nature* 284, 610-611.

[7] Ball, S.M. et al. (1999), Laboratory studies of particle nucleation: Initial results for H2SO4, H2O, and NH3 vapors. *Journal of Geophysical Research*, 104, 23709-23718, doi:10.1029/1999JD900411.

[8] Barnes, I. et al. (1994), An FTIR product study of the photooxidation of dimethyl disulfide. *Journal of Atmospheric Chemistry*, 18, 267 - 289, doi:10.1007/BF00696783.

[9] Becker, R. and Döring, W. (1935), Kinetische Behandlung der Keimbildung in übersättigten Dämpfen,*Ann. Phys. Leipzig*, 24, 719-752

[10] Berndt, T. et al. (2010). Laboratory study on new particle formation from the reaction OH + SO2: Influence of experimental conditions, H2O vapor, NH3 and the amine tert-butylamine on the overall process. *Atmospheric Chemistry and Physics,* 10, 7101-7116, doi:10.5194/acp-10-7101-2010.

[11] Bischof, O. F. and Zerrath, A. (2005). Measurements of Urban Aerosol in a Light Industrial Area-Physical Properties, Including Particle Size, Number and Diameter Concentrations. Poster presented at the 24th Annual AAAR Conference, Austin, TX (October)

[12] Boy, M. et al. (2005), Sulphuric acid closure and contribution to nucleation mode particle growth. *Atmos. Chem. Phys.* 5, 863-878.

[13] Brunelli, N. A. et al. (2009), Radial differential mobility analyzer for one nanometer particle classification. *Aerosol Sci. Technol.* 43, 53–59.

[14] Brus, D. et al. (2008), Homogeneous nucleation rate measurements in supersaturated water vapor, Journal of Chemical Physics, 131(7):074507, doi:10.1063/1.3211105

[15] Carter, W.P.L. et al. (1995a), Environmental chamber study of maximum incremental activities of volatile organic compounds. *Atmospheric Environment*, 29, 2499-2511.

[16] Carter, W.P.L. et al. (1995b), Environmental Chamber Studies of Atmospheric Reactivities of Volatile Organic Compounds. Effects of Varying Chamber and Light Source. Report to National Renewable Energy Laboratory, Contract XZ-2-12075, Coordinating Research Council, Inc., Project M-9, California Air Resources Board, Contract A032-0692, and the South Coast Air Quality Management District, Contract C91323 (Report available on Internet at /http://www.engr.ucr.edu/carter/pubs/explrept.pdf).

[17] Chen, C.C. and Tao, C.J (2000), Condensation of supersaturated water vapor on submicrometer particles of SiO2 and TiO2, J. Chem. Phys. 112, 9967; doi: 10.1063/1.481633

[18] Chen, C.C. et al. (2002), Condensation of Supersaturated Water Vapor on Charged/Neutral Nanoparticles of Glucose and Monosodium Glutamate, J*ournal of Colloid and Interface Science* 255, 158-170; doi:10.1006/jcis.2002.8486

[19] Chen, D.-R. et al. (1995), Electrospraying of Conducting Liquids for Monodisperse Aerosol Generation in the 4 nm to 1.8 μm Diameter Range. *J. Aerosol Sci.*, 26:963-977

[20] CLOUD Collaboration (2010), 2009 Progress Report on PS215/CLOUD. CERN-SPSC-2010-013, SPSC-SR-061, April 7, 2010 `/http://cdsweb.cern.ch/record/1257940/files/SPSC-SR-061.pdf.`

[21] Cocker, D. et al. (2001), State-of-the-art chamber facility for studying atmospheric aerosol chemistry. *Environmental Science and Technology*, 35, 2594 - 2601, doi:10.1021/es0019169.

[22] Coffman, D.J. and Hegg, D.A. (1995), A preliminary study of the effect of ammonia on particle nucleation in the marine boundary layer. *J. Geophys. Res.* 100(4), 7147-7160.

[23] Coulier P. J. (1975), Note sur une nouvelle propriete de l'air, *J. de Pharmacie et de Chimie, Paris*, 4(22), 165–173

[24] Curtius J. (2006), Nucleation of atmospheric aerosol particles, *Comptes Rendus Physique*, 7(9-10), 1027-1045, doi:10.1016/j.crhy.2006.10.018

[25] De la Mora, J. F. (2011), Heterogeneous Nucleation with Finite Activation Energy and Perfect Wetting: Capillary Theory Versus Experiments with Nanometer Particles, and Extrapolations on the Smallest Detectable Nucleus. *Aerosol Sci. Tech.*, 45(4): 543-554

[26] Dodge, M.C. (2000), Chemical oxidant mechanisms for air quality modeling: Critical review. *Atmospheric Environment*, 34, 2103-2130, doi:10.1016/ S1352-2310(99)00461-6.

[27] Duplissy, J. et al. (2010), Results from the CERN pilot CLOUD experiment. *Atmospheric Chemistry and Physics*, 10, 1635-1647, doi:10.5194/acp-10-1635-2010.

[28] Edney, E.O. et al. (2005), Formation of 2-methyl tetrols and 2-methylglyceric acid in secondary organic aerosol from laboratory irradiated isoprene/NOx/SO2/air mixtures and their detection in ambient PM2.5 samples collected in the eastern United States. *Atmospheric Environment,* 39, 5281 - 5289, doi:10.1016/j.atmosenv.2005.05.031.

[29] Eichkorn, S. et al. (2002), Cosmic ray-induced aerosol-formation: first observational evidence from aircraft-based ion mass spectrometer measurements in the upper troposphere. *Geophys. Res. Lett.* 29, 1698-1701.

[30] Eisele, F.L. and Tanner, D.J. (1993), Measurement of the gas phase concentration of H2SO4 and methane sulfonic acid and estimates of H2SO4 production and loss in the atmosphere. *Journal of Geophysical Research*, 98(D5), 9001-9010, doi:10.1029/93JD00031.

[31] Ermakov, V.I. et al. (1997), Ion balance equation in the atmosphere. *J. Geophys. Res.* 102, D19, 23,413-23,419.

[32] Feingold, G. and Siebert, H. (2009), in Clouds in the Perturbed Climate System (eds Heintzenberg, J. and Charlson, R.J.) 319-338 (MIT Press).

[33] Filimundi, E. et al. (2005), Measurement of Nucleation Mode Particles Using an Ultrafine Water-based Condensation Particle Counter. Abstracts of Le 21' me Congrs Francais sur les Aerosols (CFA) Paris, France.

[34] Fladerer, A. and Strey, R. (2003), Growth of homogeneously nucleated water droplets: a quantitative comparison of experiment and theory, Atmospheric Research 65 (2003) 161 - 187, doi: 10.1016/S0169-8095(02)00148-5

[35] Fletcher, N.H. (1958), Size effect in heterogeneous nucleation, *J.Chem. Phys.* 29(3), 572-576; doi: 10.1063/1.1744540

[36] Fletcher, N.H. (1962), The Physics of Rainclouds, Cambridge: Cambridge University Press

[37] Ford, I. (2004), Statistical mechanics of nucleation: a review, Proc. Instn Mech. Engrs.Part C: J. Mechanical Engineering Science, 218(1),883-899

[38] Ford, I.J. (1997), Nucleation theorems, the statistical mechanics of molecular clusters, and a revision of classical nucleation theory, *Phys. Rev. E* 56, 5615-5629, doi: 10.1103/PhysRevE.56.561

[39] Frenkel, J. (1946), Kinetic Theory of Liquids, Oxford Clarendon Press

[40] Froyd, K. D. and Lovejoy, E. R. (2003), Experimental thermodynamics of cluster ions composed of H2SO4 and H2O. 2. Measurements and ab initio structures of negative ions. *J. Phys. Chem. A* 107, 9812-9824.

[41] Gibbs J.W. (1906), Homogeneous nucleation rate measurements in supersaturated water vapor, Longmans Green London, *Scientific Papers*, 1

[42] Giechaskiel, B. et al. (2009). Calibration of Condensation Particle Counters for Legislated Vehicle Number Emission Measurements. *Aerosol Sci. Tech.*, 43(12):1164-1173.

[43] GMZ Inc. (2009), Material Safety Data Sheet. GMZ Inc., West Chester, OH, USA. Available at `http://www.gmzinc.com/uploads/docs/MSDS$_$Emery$_$622.pdf`

[44] Graus, M. et al. (2010), High resolution PTR-TOF: quantification and formula confirmation of VOC in real time. *J. Am. Soc. Mass Spectrom.* 21, 1037-1044.

[45] Hallquist, M. et al. (2009). The formation, properties and impact of secondary organic aerosol: Current and emerging issues. *Atmospheric Chemistry and Physics*, 9, 5155-5236, doi:10.5194/acp-9-5155-2009.

[46] Hegg, D.A. and Baker, M.B. (2000) Nucleation in the atmosphere, *Rep. Prog. Phys.* 72 056801 doi:10.1088/0034-4885/72/5/056801

[47] Hegg, D.A. and Baker, M.B. (2000) Nucleation in the atmosphere, Rep. Prog. Phys. 72 056801 doi:10.1088/0034-4885/72/5/056801

[48] Hering, S. V. and Stolzenburg, M. R. (2004), Continuous, Laminar Flow Water-based Particle Condensation Device and Method. US Patent 6,712,881, issued March 30, 2004.

[49] Hering, S. V. and Stolzenburg, M. R. (2005), A Method for Particle Size Amplification by Water Condensation in a Laminar, Thermally Diffusive Flow. *Aerosol Sci. Tech.*, 39(5): 428-436.

[50] Hering, S. V. et al. (2005), A Laminar-Flow, Water-Based Condensation Particle Counter (WCPC). *Aerosol Sci. Tech.*, 39:659-672.

[51] Hermann, M. et al. (2007), Particle Counting Efficiencies of New TSI Condensation Particle Counters. *J. Aerosol Sci.*, 38:674-682.

[52] Iida, K. et al. (2008), An Ultrafine, Water-Based Condensation Particle Counter and its Evaluation under Field Conditions. *Aerosol Sci. Tech.*, 42(10): 862-871.

[53] Iida K. et al.(2009), Effect of working fluid on sub–2 nm particle detection with a laminar flow ultrafine condensation particle counter, Aerosol Sci. Technol. 43, 81-96

[54] IPCC (2007), Climate Change 2007: the Physical Science Basis. Contribution of Working Group I to the Fourth Assessment Report of the Intergovernmental Panel on Climate Change, Cambridge Univ. Press

[55] Jiang J. H. et al. (2011), Influence of convection and aerosol pollution on ice cloud particle effective radius, *Atmospheric Chemistry and Physics*, 11(2), 457-463, doi:10.5194/acp-11-457-2011

[56] Jonsson, A. et al. (2008a), The effect of temperature and water on secondary organic aerosol formation from ozonolysis of limonene, D3-carene, and a-pinene. *Atmospheric Chemistry and Physics*, 8, 6541 - 6549, doi:10.5194/acp-8-6541-2008.

[57] Jonsson, A. et al. (2008b). Influence of OH scavenger on the water effect of secondary organic aerosol formation from ozonolysis of limonene, D3-carene, and a-pinene. *Environmental Science and Technology*, 42, 5938 - 5944, doi:10.1021/es702508y.

[58] Junninen, H. et al. (2010), A high-resolution mass spectrometer to measure atmospheric ion composition. *Atmos. Meas. Tech.* 3, 1039 - 1053.

[59] Kane, D. and El–Shall, M.S. (1996), Condensation of supersaturated vapors of hydrogen bonding molecules: Ethylene glycol, propylene glycol, trimethylene glycol, and glycerol,*J. Chem. Phys.* 105, 7617, doi:10.1063/1.4725484

[60] Kang, E. et al. (2007), Introducing the concept of Potential Aerosol Mass (PAM). A*tmospheric Chemistry and Physics*, 7, 5727-5744, doi:10.5194/acp-7-5727-2007.

[61] Kashchiev, D. (2000), Nucleation: Basic Theory with Applications, Butterworth-Heinemann, Oxford

[62] Kashchiev, D. (1982), On the relation between nucleation work, nucleus size and nucleation rate, J.Chem.Phys., 76, 5098-5102

[63] Kazil, J. and Lovejoy, E. R. (2007), A semi-analytical method for calculating rates of new sulfate aerosol formation from the gas phase, *Atmos. Chem. Phys.* 7, 3447-3459.

[64] Kerminen, V.-M. and Kulmala, M. (2002), Analytical formulae connecting the real and the apparent nucleation rate and the nuclei number concentration for atmospheric nucleation events.*J. Aerosol Sci.* 33, 609-622.

[65] Kerminen V.M. et al. (2005), Direct observational evidence linking atmospheric aerosol formation and cloud droplet activation, *Geophysical Research Letters,* 32,14

[66] Kerminen, V.M. et al. (2010), Atmospheric nucleation: highlights of the EUCAARI project and future directions. *Atmos. Chem. Phys.* 10, 10829-10848.

[67] Kesten, J. et al. (1991), Calibration of a TSI Model 3025 Ultrafine Condensation Particle Counter. *Aerosol Sci. Tech.*, 15:107-111.

[68] Kirkby, J. Cosmic rays and climate.*Surv. Geophys.* 28, 333-375 (2007).

[69] Kirkby J. et al. (2011), Role of Sulphuric Acid, Ammonia and Galactic Cosmic Rays in Atmospheric Aerosol Nucleation, *Nature*, 476, 429

[70] Köhler, H. (1936), The nucleus in and the growth of hygroscopic droplets, Trans. Faraday Soc. 32(2):1152-1161, doi: 10.1039/TF9363201152

[71] Krämer, L. et al. (2000), Microstructural rearrangement of sodium chloride condensation aerosol particles on interaction with water vapor, *J. Aerosol Sci.* 31, 6, pp. 673-685

[72] Kuang, C. et al. (2008), Dependence of nucleation rates on sulfuric acid vapor concentration in diverse atmospheric locations. *J. Geophys. Res.* 113, D10209, doi:0.1029/2007JD009253.

[73] Kuang, C. et al. (2011). Modification of Laminar Flow Ultrafine Condensation Particle Counters for the Enhanced Detection of 1 nm Condensation Nuclei. *Aerosol Sci. Tech.*, 46(3):309-315.

[74] Kulkarni, G. et al. (2011), Comparison of experimental and numerical studies of the performance characteristics of a pumped counterflow virtual impactor, *Aerosol Sci. Technol.*, 45(3), 382-392, doi:10.1080/02786826.2010.539291.

[75] Kulmala M. (2003), How particles nucleate and grow, *Science*, 302, 1000

[76] Kulmala M. et al. (2004), Formation and growth rates of ultrafine atmospheric particles: a review of observations, *Journal of Aerosol Science,* 35(2), 143-176, doi:10.1016/j.jaerosci.2003.10.003

[77] Kulmala, M. et al. (2006), Cluster activation theory as an explanation of the linear dependence between formation rate of 3nm particles and sulphuric acid concentration, *Atmos. Chem. Phys.,* 6, 787-793.

[78] Kulmala, M. et al. (2007), Towards direct measurement of atmospheric nucleation. *Science* 318, 89-92.

[79] Kulmala, M. and Kerminen, V.-M. (2008), On the formation and growth of atmospheric nanoparticles. *Atmos. Re*s. 90, 132-150.

[80] Kupc et al. (2011), A fibre-optic UV system for H2SO4 production in aerosol chambers causing minimal thermal effects, *J. of Aerosol Science*, 42(8) 532 - 543

[81] Kupc A. et al. (2013), Unusual Temperature Dependence of Heterogeneous Nucleation of Water Vapor on Ag Particles, Manuscript submitted to Aerosol Science and Technology on 20th February 2013

[82] Kupc A. et al. (2013), Laboratory Characterization of a New Nano-Water-Based CPC 3788 and Performance Comparison to an Ultrafine Butanol-Based CPC 3776, *Aerosol Science and Technology*, 47(2), 183-191, doi:10.1080/02786826.2012.738317

[83] Kurten T. et al. (2008), Amines are likely to enhance neutral and ion-induced sulfuric acid-water nucleation in the atmosphere more effectively than ammonia, *Atmos. Chem. Phys.* 8, 4095-4103.

[84] Lee, S. H. et al. (2003), Particle formation by ion nucleation in the upper troposphere and lower stratosphere. *Science* 301, 1886-1889.

[85] Liu, W. et al. (2005). Calibration of Condensation Particle Counters. SAE Technical Paper 2005-01-0189, SAE International

[86] Liu, W. et al. (2006). Water-Based Condensation Particle Counters for Environmental Monitoring of Ultrafine Particles. *J. Air Waste Manage. Assoc.*, 56:444-455.

[87] Lohmann U. (2012), Surface properties of water and Köhler curves, Presentation (16th October 2012), `www.iac.ethz.ch/edu/courses/master/modules/cloud_microphysics/handouts-2012/surface_koehler-corrected.pdf`

[88] Lovejoy, E. R. et al. (2004), Atmospheric ion-induced nucleation of sulfuric acid and water, *Journal of Geophysical Research: Atmospheres*, 109(D8), 2156-2202 doi:10.1029/2003JD004460

[89] Magnusson, L. E. et al. (2003). Correlations for Vapor Nucleating Critical Embryo Parameters. J. *Phys. Chem. Ref. Data*, 32(4): 1387-1410.

[90] McGraw, R. and Wu, D.T (2003), Kinetic extensions of the nucleation theorem, J. Chem. Phys., 118, 9337, doi:10.1063/1.1565098

[91] McGraw et al. (2012), Kinetics of Heterogeneous Nucleation in Supersaturated Vapor: Fundamental Limits to Neutral Particle Detection Revisited, *Aerosol Science and Technology*, 46(9), 1053-1064

[92] McMurry, P.H. (2000), A review of atmospheric aerosol measurements, *Atmospheric Environment*, 34(12-14), 1959 - 1999, doi:10.1016/S1352-2310(99)00455-0

[93] McMurry, P.H. et al. (2005). A criterion for new particle formation in the sulfur-rich Atlanta atmosphere. *Journal of Geophysical Research*, 110, D22S02, doi:10.1029/2005JD005901.

[94] Merikanto, J. et al. (2009) Impact of nucleation on global CCN. *Atmos. Chem. Phys.* 9, 8601-8616

[95] Metzger, A. et al. (2010). Evidence for the role of organics in aerosol particle formation under atmospheric conditions. *Proceeding of the National Academy of Science of the United States of America*, 107, 6646, doi:10.1073/pnas.0911330107.

[96] Mokross, B.J. (1997), Nucleation theory and small system thermodynamics, *Materials Physics and Mechanics*, 1(6),8

[97] Mordas, G. et al. (2008). On Operation of the Ultra-Fine Water-Based CPC TSI 3786 and Comparison with Other TSI Models (TSI 3776, TSI 3772, TSI 3025, TSI 3010, TSI 3007). *Aerosol Sci. Tech.*, 42(2): 152-158.

[98] Murphy, S.M. et al. (2007), Secondary aerosol formation from atmospheric reactions of aliphatic amines. *Atmos. Chem. Phys.* 7, 2313-2337.

[99] Nadykto A.B and Yu F. (2007), Strong hydrogen bonding between atmospheric nucleation precursors and common organics, *Chemical Physics Letters,* 435(1-3), 14 - 18

[100] Norman, M. et al. (2007), O21 as reagent ion in the PTR-MS instrument: detection of gas-phase ammonia. *Int. J. Mass Spectrom.* 265, 382-387.

[101] Oxtoby, D.W. and Kashchiev, D. (1994), A general relation between the nucleation work and the size of the nucleus in multicomponent nucleation, *J. Chem. Phys.* 100, 7665, doi:110.1063/1.466859

[102] Paasonen, P. et al. (2009), Connection between new particle formation and sulfuric acid at Hohenpeissenberg (Germany) including the influence of organic compounds. *Boreal Envir. Res.* 14, 616-629.

[103] Pathak, R.K. et al. (2007), Ozonolysis of a-pinene: Parametrization of secondary organic aerosol mass fraction. *Atmospheric Chemistry and Physics*, 7, 3811-3821, doi:10.5194/acp-7-3811-2007.

[104] Pathak, R.K. et al. (2008), Ozonolysis of b-pinene: Temperature dependence of secondary organic aerosol mass fraction. *Environmental Science and Technology*, 42, 5081-5086, doi:10.1021/es070721z.

[105] Paulsen, D. (2005), Secondary organic aerosol formation by irradiation of 1,3,5-trimetylbenzene-NOx-H2O in a new reaction chamber for atmospheric chemistry and physics. *Environmental Science and Technology,* 39, 2668-2678, doi:10.1021/es0489137.

[106] Petäjä, T.et al. (2006), Detection Efficiency of a Water-Based TSI Condensation Particle Counter 3785. *Aerosol Sci. Tech.*, 40(12): 1090-1097.

[107] Petersen D. (2001), Experimental Investigation on Condensation of Supersaturated Vapors on Nanoparticles Applying a Newly Developed Laser Light Scattering System, Ph.D. thesis, Faculty of Natural Sciences and Mathematics, University of Vienna

[108] Petersen, D. et al. (2001), Soluble-Insoluble Transition in Binary Heterogeneous Nucleation, *Phys. Rev. Lett.*, 87, 22, 2257031-4, doi: 10.1103/PhysRevLett.87.225703

[109] Pichelstorfer. L. (2010) Temperature dependence of heterogeneous nucleation, Master Thesis, University of Vienna

[110] Pierce, J. R. and Adams, P. J. (2009), Can cosmic rays affect cloud condensation nuclei by altering new particle formation rates? *Geophys. Res. Lett.* 36, L09820, doi:10.1029/2009GL037946

[111] Pierce J. (2011), Atmospheric chemistry: Particulars of particle formation, *Nature Geoscience*, 4,665-666, doi:10.1038/ngeo1267

[112] Pörstendoerfer, J. et al. (1985), Heterogeneous nucleation of water vapor on monodisperse Ag and NaCl particles with diameters between 6 and 18 nm, *Aerosol Sci. Technol.* 4, 65

[113] Presto, A.A. et al. (2005), Secondary organic aerosol production from terpene ozonolysis. 1. Effect of UV radiation. *Environmental Science and Technology*, 39, 7036-7045, doi:10.1021/es050174m.

[114] Pruppacher H. R. and Klett J. D (1998), Microphysics of Clouds and Precipitation, Second Revised and Enlarged Edition with an Introduction to Cloud Chemistry and Cloud Electricity, *Climatic Change,* 38(4), 497-499, doi:10.1023/A:1005304329379

[115] Rader, D. J. et al. (1987), Evaporation Rates of Monodisperse Organic Aerosols in the 0.02 to 0.2- μ m-Diameter Range. *Aerosol Sci. Tech.*, 6(3): 247–260.

[116] Raes F. and Janssens A. (1985), Ion-induced aerosol formation in a H2O-H2SO4 system–I. Extension of the classical theory and search for experimental evidence, *Journal of Aerosol Science* 16(3), 217-227, doi:10.1016/0021-8502(85)90028-X

[117] Raes, F. et al. (1986) The role of ion-induced aerosol formation in the lower atmosphere. *J. Aerosol Sci.* 17, 466-470.

[118] Riipinen, I. et al. (2009), Applying the Condensation Particle Counter Battery (CPCB) to Study the Water-Affinity of Freshly-Formed 2-9 nm Particles in Boreal Forest. *Atmos. Chem. Phys.*, 9:3317-3330.

[119] Rosenfeld, D. et al. (2008), Flood or drought: how do aerosols affect precipitation? *Science* 321, 1309-1313.

[120] Saathoff, H. et al. (2009), Temperature dependende of yields of secondary organic aerosols from the ozonolysis of a-pinene and limonene. *Atmospheric Chemistry and Physics*, 9, 1551-1557, doi:10.1016/S0021-8502(03)00363-X.

[121] Schobesberger et al. (2010), Experiments on the temperature dependence of heterogeneous nucleation on nanometer-sized NaCl and Ag particles, *Chem. Phys. Chem.*, 11(18), 3874-3882

[122] Seinfeld J.H. (2011), Insights on global warming, *AIChE Journal*, 57(12), 1547

[123] Seinfeld, J.H. and Pandis, S.N. (1998), Atmospheric Chemistry and Physics. Wiley: Hoboken, New York.

[124] Sem, G. J. (2002). Design and Performance Characteristics of Three Continuous-Flow Condensation Particle Counters: A Summary. *Atmos. Res.*, 62:267-294.

[125] Sipila M. et al. (2010), The role of sulfuric acid in atmospheric nucleation, *Science* 327, 1243-1246.

[126] Smith J. et al. (2008), Chemical composition of atmospheric nanoparticles formed from nucleation in Tecamac, Mexico: Evidence for an important role for organic species in nanoparticle growth,*Geophysical Research Letters,* 35(4),1944

[127] Smith, J. N. et al. (2010), Observations of aminium salts in atmospheric nanoparticles and possible climatic implications. *Proc. Natl Acad. Sci.* USA 107, 6634-6639.

[128] Sorokin, A. and Arnold, F. (2007), Laboratory study of cluster ions formation in H2SO4-H2O system: implications for threshold concentration of gaseous H2SO4 and ion-induced nucleation kinetics. *Atmos. Environ.* 41, 3740-3747.

[129] Spracklen, D. V. et al. Contribution of particle formation to global cloud condensation nuclei concentrations. *Geophys. Res. Lett.* 35, L06808, doi:10.1029/ 2007GL033038 (2008).

[130] Stolzenburg, M. R. (1988), An Ultrafine Aerosol Size Distribution Measuring System. Ph.D. thesis, Mechanical Engineering Department, University of Minnesota, MN.

[131] Stolzenburg, M. R. and McMurry, P. H. (1991), An Ultrafine Aerosol Condensation Nucleus Counter. *Aerosol Sci. Tech.*, 14(1): 48-65.

[132] Strey, R. et al. (1986), Homogeneous Nucleation Rates for n-Alcohol Vapors Measured in a 2-Piston Expansion Chamber, *J. Chem. Phys.* 84(4), 2325

[133] Svensmark, H. and Friis-Christensen, E. (1997), Variation of cosmic ray flux and global cloud coverage-a missing link in solar-climate relationships. *J. Atmos. Sol. Terr. Phys.* 59, 1225-1232.

[134] Szymanski, W. and Wagner, P. (1990), Absolute aerosol number concentration measurement by simultaneous observation of extinction and scattered light. *J. Aerosol Sci.*, 21:441-451

[135] Thomson, W.T. (1870), On the equilibrium of vapour at a curved surface of a liquid, *Proc. Roy. Soc. Edinb.*, 7, 63

[136] TSI Inc. (2006), Generating Emery Oil Aerosol for Calibration. TSI Application note EM-004. TSI Inc., Shoreview, MN, USA. Available at http://www.tsi.com/uploadedFiles/ Site Root/Products/Literature/ApplicationNotes/EM-004-Generating Emery Oil Aerosol-5001326A.pdf

[137] Turco, R. P. et al. (1998), A new source of tropospheric aerosols: Ion–ion recombination. *Geophys. Res. Lett.* 25, 635-638.

[138] Usoskin, I.G. et al. (2004), Cosmic ray induced ionization in the atmosphere: spatial and temporal changes. *J. Atmos. Sol. Terr. Phys.* 66, 1791-1796.

[139] Vanhanen, J. et al. (2011), Particle size magnifier for nano-CN detection. *Aerosol Sci. Technol.* 45, 533-542.

[140] Vehkamäki, H. et al. (2007), Heterogeneous Multicomponent Nucleation Theorems for the Analysis of Nanoclusters, *J. Chem. Phys.* 126, 174707, doi:10.1063/1.1565098

[141] Vehkamäki, H. (2010), Classical Nucleation Theory in Multicomponent Systems, Springer

[142] Vehkamäki, H.and Riipinen, I. (2012), Thermodynamics and kinetics of atmospheric aerosol particle formation and growth,*Chem. Soc. Rev.*, 41(15) 5160-5173, doi: 10.1039/C2CS00002D

[143] Vesala et al. (1997), Models for condensational growth and evaporation of binary aerosol particles. *J. Aerosol Sci.* 28, 565-598.

[144] Vissanen, Y. et al. (2000), Erratum: Homogeneous nucleation rates for water, J. Chem. Phys. 99, 4680, *J. Chem. Phys.* 112, 18, 8205

[145] Vissanen, Y.et al. (1993), Homogeneous nucleation rates for water, *J. Chem. Phys.* 99, 4680

[146] Volmer M. and Weber A. (1926), Keimbildung in übersättigten Gebilden (Nucleation of supersaturated structures), *Phys. Chem.*, 119, 277

[147] Wagner, P. et al. (2003) Nucleation probability in binary heterogeneous nucleation of water-n-propanol vapor mixtures on insoluble and soluble nanoparticles, *Phys. Rev. E,* 67, 021605

[148] Wagner, P.E. and Strey, R. (1981), Homogeneous Nucleation Rates of Water-Vapor Measured in a 2-Piston Expansion Chamber, J. Phys. Chem., 85 (18), 2694

[149] Wagner, P.E. (1985), A constant-angle Mie scattering method (CAMS) for investigation of particle formation processes, *Journal of Colloid and Interface Science,* 105, 456-467; doi: 10.1016/0021-9797(85)90319-4

[150] Wang, L. et al. (2010), Atmospheric nanoparticles formed from heterogeneous reactions of organics. *Nature Geosci.* 3, 238-242.

[151] Wang, J. et al. (2012), Flux induced growth of atmospheric nanoparticles by organic vapors. *Atmos. Chem. Phys. Discuss.*, 12, 22813-22833, doi:10.5194/acpd-12-22813-2012

[152] Weber R.J. (1996), Measured atmospheric new particle formation rates: Implications for nucleation mechanisms, *Chem. Eng. Comm.* 151,53-62

[153] Wedekind et al. (2004) Nucleation and Atmospheric Aerosols 2004: 16th International Conference N2 - 4, 49, Kyoto University Press, Kyoto

[154] Wehner, B. et al. (2011). Characterization of a New Fast CPC and its Application for Atmospheric Particle Measurements. *Atmos. Meas. Tech.*, 4:823-833.

[155] Wiedensohler, A. (1988). An Approximation of the Bipolar Charge Distribution for Particles in the Submicron Size Range. *J. Aerosol Sci.*, 19:387-389.

[156] Wiedensohler, A. et al. (1997). Intercomparison Study of the Size-Dependent Counting Efficiency of 26 Condensation Particle Counters. *Aerosol Sci. Tech.*, 27(2):224-242.

[157] Wilson C. T. R. (1911), On a method of making visible the paths of ionising particles, *Proc. R. Soc. London, Ser. A*, 88,285 - 288

[158] Wilson C. T. R. (1899), On the comparative efficiency as condensation nuclei of positively and negatively charged ions, *Philos. Trans. R. Soc. London, Ser. A,* 193,289-308

[159] Winkler, P.M. et al. (2006), Condensation of water vapor: Experimental determination of mass and thermal accommodation coefficients, *Journal of Geophysical Research* 111, D19202

[160] Winkler, P. M. et al. (2008), Condensation Particle Counting Below 2 nm Seed Particle Diameter and the Transition from Heterogeneous to Homogeneous Nucleation. *Atmos. Res.* 90:125–131; doi: 10.1016/j.atmosres.2008.01.001

[161] Winkler, P. M. et al. (2008a), Condensation Particle Counting Below 2 nm Seed Particle Diameter and the Transition from Heterogeneous to Homogeneous Nucleation. Atmos. Res. 90:125–131, doi: 10.1016/j.atmosres.2008.01.001

[162] Winkler P. M. et al (2008b), Heterogeneous Nucleation Experiments Bridging the Scale from Molecular Ion Clusters to Nanoparticles, *Science*, 319, 1374

[163] Winkler, P.M. et al. (2012), Quantitative Characterization of Critical Nanoclusters Nucleated on Large Single Molecules, Phys, Rev. Lett. 108, 085701; doi:10.1103/PhysRevLett.108.085701

[164] Wölk, J. and Strey, R. (2001), Homogeneous nucleation of H2O and D2O in comparison: The isotope effect, *J. Phys. Chem. B* 105, 11683; doi: 10.1021/jp0115805

[165] Wölk, R. et al., (2002) Empirical function for homogeneous water nucleation rates; Journal of Chemical Physics, 117, 10, p. 4954-4960; doi: 10.1063/1.1498465

[166] Yu, F.R. and Turco, P. (2000) Ultrafine aerosol formation via ion-mediated nucleation, *Geophys. Res. Lett.* 27,883-886

[167] Zai, S., Zhen, H., and Jia-song, W. (2006). Studies on the Size Distribution, Number and Mass Emission Factors of Candle Particles Characterized by Modes of Burning. *Aerosol Sci.*, 37:1484-1496.

[168] Zeldovich J. (1942), Theory of the formation of a new phase. cavitation, *Zh. Eksp Theor Fiz*, 12,525-538

[169] Zeldovich J. (1943), On the theory of the formation of a new phase, cavitation, *Acta Physicochimica USS*, USS XVIII:1/22/01

[170] Zhang, R. et al. (2004), Atmospheric new particle formation enhanced by organic acids. *Science* 304, 1487-1490.

[171] Zhang, R. et al. (2009), Formation of nanoparticles of blue haze enhanced by anthropogenic pollution. *Proc. Natl Acad. Sci.* USA 106, 17650-17654.

[172] Zhang, R. (2010). Getting to the critical nucleus of aerosol formation. *Science*, 328, 1366-1367, doi:10.1126/science.1189732

[173] Zhang, K. et al. (2011), Radon activity in the lower troposphere and its impact on ionization rate: a global estimate using different radon emissions. *Atmos. Chem. Phys. Discuss. 11,* 3251-3300.

[174] Zhao J. et al. (2009), Hydrogen-Bonding Interaction in Molecular Complexes and Clusters of Aerosol Nucleation Precursors, *J. Phys. Chem. A*, 113, 680–689

[175] Ziereis, H. and Arnold, F. (1986), Gaseous ammonia and ammonium ions in the free troposphere. *Nature* 321, 503-505.

List of Figures

List of Tables

CURRICULUM VITAE

Agnieszka Kupc

Email: agnieszka.kupc@univie.ac.at

EDUCATION

May – August 2012	**Fellow within Graduate Visitor Program, ASP at NCAR,** Atmospheric Chemistry Division, research Ultrafine Aerosols Research Group, Boulder, CO
February 2009 – present	**PhD position at University of Vienna, Vienna, AUSTRIA** Aerosol- and Environmental Physics Group, focus on aerosol nucleation processes (CLOUD-ITN Project). PhD research was partly done at CERN, Switzerland. **PhD Thesis:** *Experimental study of nucleation in different vapors and its temperature dependence and the effect of particle properties on the response of condensation particles counters*
January 2008	**Master of Science in Natural Resources Management and Ecological Engineering (DI), University of Natural Resources and Applied Life Sciences (BOKU), Vienna, AUSTRIA** (Jointly taught and awarded with Lincoln University in New Zealand)
February 2006 – May 2007	**Lincoln University, Canterbury, NEW ZEALAND**
February 2005 – January 2006	**University of Natural Resources and Applied Life Sciences (BOKU), Vienna, AUSTRIA**, Master Course in Natural Resources Management and Ecological Engineering, Spec. Ecological Engineering
June 2004	**Bachelor of Science in Environmental Protection and Management,**
June – September 2003	**Instituto Superior Tecnico (IST), Lisbon, PORTUGAL** Research work within ERASMUS Student Exchange Program, Faculty of Chemistry
October 2000 – June 2004	**Gdansk University of Technology, Gdansk, POLAND** Environmental Protection and Management Course Faculty of Chemistry
June 2000	Graduated from Secondary School of General Education, Rumia, POLAND, Faculty: Mathematics and Physics

ADDITIONAL TRAINING

January 2012	**Secondment** at TSI Aachen, Germany: Characterization of the new ultrafine N-WCPC and comparison to UCPC
December 2010	**Secondment** at the Institute for Atmospheric and Environmental Sciences, Goethe University Frankfurt am Main, Germany
August 2010	**Workshop** on *Atmospheric Nucleation*, Hyytiälä, Finland
August 2010	**Summer school:** *Formation and Growth of Atmospheric Aerosols*, Hyytiälä, Finland
August 2009	**Summer School**: *Atmospheric Aerosols and Clouds*, Rabenberg, Germany
July 2009	**Summer School:** *Basic Aerosol Science*, University of Vienna, Austria
March 2009	**Winter School**: *Physics and Chemistry of air pollution and their effects*, Hyytiälä, Finland
November 2008	**Joint Research Centre, Ispra, Italy** Workshop on Air Quality Assessment Strategies: Addressing the new Air Quality Directive and CAFE Thematic Strategy
October 2008	**Joint Research Centre, Geel, Belgium** Training Course on Use of Reference Materials and the Estimation of Measurement Uncertainty
June 2008	**Joint Research Centre, Ispra, Italy** Life Cycle Assessment Training Course

WORK EXPERIENCE

May- August 2012	**Fellow within Graduate Visitor Program, ASP at NCAR,** Atmospheric Chemistry Division, research within Ultrafine Aerosols Research Group, Boulder, CO
February 2009 – October 2012	**Project Assistant at University of Vienna, Vienna, Austria** Aerosol- and Environmental Physics group, PhD position in the field of aerosol nucleation processes within CLOUD-ITN Project/ ~3 months each year at CLOUD Experiment (5 campaigns) at **CERN, Switzerland**
January 2008 – January 2009	**Trainee at the European Commission, Joint Research Centre (JRC)**, Ispra, Italy, Institute for Environment and Sustainability, Transport and Air Quality Unit, Action Air Pollution and Effects – Project: Characterization of Atmospheric Aerosol
October – December 2004	**Trainee at the Institute of Meteorology and Water Management (IMGW)**, Gdynia, Poland

CONFERENCES

2012 European Aerosol Conference (EAC) Granada, Spain,
2011 European Aerosol Conference (EAC) Manchester, UK
2010 International Aerosol Conference (IAC) Hesinki, Finland (BEST POSTER AWARD)
2010 Marie Curie Satellite Event (ESOF 2010 Euroscience Open Forum), Turin, Italy
2009 European Aerosol Conference (EAC) Karlsruhe, Germany
2009 International Conference on Nucleation and Atmospheric Aerosols (ICNAA) Prague

Abstracts submitted for:
2013 ICNAA, Fort Collins, USA (June)
2013 EAC, Prague (September)

PUBLICATIONS

2013 **Kupc** *et al.,* Unusual temperature dependence of heterogeneous nucleation of water vapor on Ag particles *(Manuscript in the form of an Aerosol Research Letter submitted to Aerosol Science and Technology: 20th February 2013)*

2013 **Kupc** *et al.,* Laboratory Characterization of a New Nano Water-Based CPC 3788 and Performance Comparison to an Ultrafine Butanol-Based CPC 3776, Aerosol Science and Technology, 47, 2, 183-191

2011 Kirkby et al., Role of sulphuric acid, ammonia and galactic cosmic rays in atmospheric aerosol nucleation, *Nature*, 476, 429-U77

2011 **Kupc** et al., A fibre-optic UV system for H_2SO_4 production in aerosol chambers causing minimal thermal effects, *Journal of Aerosol Science*, 42, 8, 532-543

2013 Almeida et al., Molecular understanding of amine-sulphuric acid particle nucleation in the atmosphere *(Manuscript in preparation)*

2013 Wimmer D. et al. Performance of Diethylene Glycol based particle counters in the sub 3 nm size range *(Manuscript submitted to Atmos. Meas. Tech. Discuss.)*

POSTERS

2012 Wimmer, D., Kreissl F., Kürten, A., J. Curtius, J., Riccobono, F., **Kupc, A**., Lehtipalo, K. and the CLOUD collaboration. *Calibration of CPCs at low temperatures using the CLOUD chamber,* EAC Granada

2011 **Kupc A**., Vrtala, A., Winkler P.M., and Wagner P.E., *Heterogeneous nucleation of water vapor on nanoparticles and its temperature dependence*, EAC Manchester

2011 Wimmer D., Kreissl F., Metzger A., Kürten K., Curtius J., **Kupc A**., Lehtipalo K., Riccobono F. and CLOUD Collaboration, *Performance of an ultrafine Diethylene Glycol (DEG) based Condensation Particle Counter,* EAC Manchester

2010 **Kupc A.**, Vrtala A., Winkler P.M., Wagner P.E., and CLOUD Collaboration, *A unique UV fibre optic system for H2SO4 production inside the CLOUD chamber*, IAC Helsinki **(BEST POSTER AWARD)**

2010 S. Ehrhart, **A. Kupc**, L. Rondo, A. Kurten, J. Curtius and the CLOUD collaboration, *Modelling of CLOUD chamber chemistry*, IAC Helsinki

PRESENTATIONS

2012 *Comprehensive Laboratory Characterization of a New Nano Water-based CPC and Performance Comparison to an Ultrafine CPC*, EAC Granada

2012 *A new N-WCPC and its suitability for nanoparticle measurements in ambient aerosols and at the CLOUD experiment*, TSI Webinar within Global Aerosol Education (invited online talk), 12th July

2010 *A unique UV fibre optic system for H_2SO_4 production inside the CLOUD chamber* IAC Helsinki, Finland (back-up talk)